

DISSERTATION

NEAR-RESONANT AND RESONANT LIGHT IN ULTRACOLD GASES

Submitted by
Jonathan Gilbert
Department of Physics

In partial fulfillment of the requirements
For the Degree of Doctor of Philosophy
Colorado State University
Fort Collins, Colorado
Spring 2020

Doctoral Committee:

Advisor: Jacob Roberts

Dylan Yost
Mark Bradley
Mario Marconi

Copyright by Jonathan Gilbert 2020

All Rights Reserved

ABSTRACT

NEAR-RESONANT AND RESONANT LIGHT IN ULTRACOLD GASES

This dissertation describes experiments and calculations involving light manipulation of atoms and light propagation in ultracold gases. There are three major sections to this dissertation. Each section presents a research topic connected to the main subject of near-resonant and resonant light in ultracold gases. First, this dissertation details the theoretical description and experimental implementation of a novel cooling technique for ultracold atoms trapped in a confining potential. Manipulating the internal states of atoms by applying near-resonant laser pulses at specified times leads to high energy atoms being preferentially selected and then slowed to achieve cooling. We call the technique "spatially truncated optical pumping (STOP) cooling." Advantages of the technique include its straightforward adaptability into experiments already using a magneto-optical trap; its applicability to any species that can be laser cooled and trapped in a confining potential; it does not depend on highly specific transitions for cooling; it does not depend on number loss for cooling. We present experimental results from applying the technique to an ultracold gas of ^{87}Rb . We also present theoretical predictions of expected cooling rates, along with possible improvements to our apparatus that could lead to further cooling.

Next, this dissertation details numerical calculations of near-resonant light propagation through a highly absorptive elongated ultracold gas. The confined gas modeled by these calculations are representative of gases commonly found in ultracold atom experiments. The spatial density distribution and spatial extent of these gases leads to a substantial gradient in the index of refraction. In addition, these gases can have a smaller spatial extent than that of the cross section of a laser beam that illuminates them. We present calculations that show the index variation in these systems can lead to frequency-dependent focusing or defocusing of incident near-resonant light. In some cases, focusing results in light intensities inside of the gas that are over an order of magnitude higher

than the incident value. Additionally, we show that refraction and diffraction of the light results in non-intuitive patterns forming in the directions perpendicular to the light propagation.

Lastly, this dissertation details the theoretical treatment and experimental measurements of the time-dependent absorption and phase response of an ultracold gas that is suddenly illuminated by near-resonant light. These studies focus on dynamics occurring over timescales on the order of an atomic excited state lifetime. Because the atoms cannot respond instantaneously to the applied light, both the absorption response and phase response require time to develop, with the phase response being slower than the absorption response. Related polarization effects such as Faraday rotation are due to phase shifts imparted by the gas, and therefore these effects also require time to develop. We detail our experimental measurements of the time-dependent development of Faraday rotation in an ultracold gas of ^{85}Rb and compare the results to predictions using a theoretical approach based on solving optical Bloch equations. We identify how parameters such as the applied magnetic field strength and optical thickness of the gas influence the response timescales of the gas.

ACKNOWLEDGEMENTS

I would like to express my deep appreciation to my advisor, Prof. Jacob Roberts. I am fortunate to have conducted research under his guidance, and I will be forever grateful for having the opportunity to work in his lab. His knowledge and insights provided invaluable contributions and direction to my studies. His patience and encouragement allowed me to explore and grow as a scientist. And his passion for physics and excitement for new discoveries were, and will remain, truly inspirational.

I would like to thank Prof. Siu Au Lee for her support and words of advice throughout my time in the graduate program. I would like to thank Wei-Ting Chen for helping me get acquainted with the lab and for his friendship during our time in the research group. I also thank Rebekah Ferrier Wilson, Renae Wall, Colin Roberts, and Mark Watkins for their contributions to the research presented in this dissertation. I thank Chris Chambers, Adam Craycraft, and Puchang Jiang for their friendship, encouragement, and the wide-range of discussions we had. Finally, I owe countless thanks to my family. They stood by my side through thick and thin and inspired me to never give up.

DEDICATION

This dissertation is dedicated to my parents, Mary and Larry, and my sisters, Audrey and Amber, in recognition of their unconditional love, never-ending support, and immeasurable patience.

TABLE OF CONTENTS

ABSTRACT	ii
ACKNOWLEDGEMENTS	iv
DEDICATION	v
LIST OF FIGURES	ix
Chapter 1 Introduction	1
1.1 Background	2
1.2 Overview	3
1.2.1 Laser Cooling and Trapping Atoms (Chapter 2)	3
1.2.2 General Experimental Apparatus (Chapter 3)	4
1.2.3 Spatially Truncated Optical Pumping Cooling (Chapter 4)	5
1.2.4 Intensity Pattern Formation in a Trapped Gas (Chapter 5)	6
1.2.5 Faraday Rotation at Atomic Lifetime Timescale (Chapter 6)	6
1.2.6 Radiation Transport Through an Ultracold Gas (Chapter 7)	7
Chapter 2 Laser Cooling and Trapping Atoms	9
2.1 Doppler Cooling Atoms	9
2.2 Sub-Doppler Cooling Atoms	13
2.2.1 Lin-Perp-Lin Cooling	13
2.2.2 Motion-Induced Orientation Cooling	17
2.3 Magneto-Optical Trap	20
2.4 Optical Dipole Trap	22
Chapter 3 General Experimental Apparatus	26
3.1 Neutral Atoms for Laser Cooling	26
3.1.1 The D2 Line of ⁸⁵ Rb and ⁸⁷ Rb	27
3.2 Ultra-High Vacuum Chamber	29
3.2.1 Bake-Out Procedure	30
3.3 External-Cavity Diode Lasers	31
3.3.1 Laser Beam Manipulation Tools	34
3.4 Experiment Magneto-Optical Trap	37
3.4.1 Loading Atoms into the MOT	38
3.5 Experiment Optical Dipole Trap	39
3.5.1 Aligning and Loading the FORT	40
3.6 Imaging Ultracold Gases	43
3.6.1 Basic Atomic Gas Characteristics	44
3.6.2 Probe Beam and Optical Depth	45
3.6.3 Data from CCD Camera	47
3.7 Measuring Transmission Signals	49
3.7.1 Laser Beam with Rapid Turn-on	50
3.7.2 Electronics and Detectors	50

Chapter 4	Spatially Truncated Optical Pumping Cooling	52
4.1	A Novel Nonevaporative Technique	54
4.1.1	Overview of a STOP Cooling Cycle	55
4.2	STOP Cooling Theory	56
4.2.1	Simple Harmonic Oscillator Model	56
4.2.2	Impact of Elastic Collisions	60
4.2.3	Comparison to Evaporation	64
4.3	Extension to Molecules	65
4.4	Experimental Implementation	67
4.4.1	STOP Cooling Beams	68
4.4.2	Single Cycle to Multiple Cycles	69
4.5	STOP Cooling Data	70
4.6	STOP Cooling Results	71
4.7	Comparing Measurements to Predictions	73
4.7.1	Possible Heating from Optical Pumping	73
4.7.2	Realistic Optical Trap Shape	74
4.7.3	Apparatus Improvements	75
4.7.4	Ways to Mitigate Limitations	76
4.8	STOP Cooling Conclusions	77
Chapter 5	Intensity Pattern Formation in a Trapped Gas	79
5.1	A Detour from STOP Cooling	79
5.2	Near-Resonant Light in Optically Thick Gases	81
5.3	Envelope Wave Equation	85
5.3.1	Integration Method	86
5.3.2	Calculation Parameters	88
5.4	Calculation Results	89
5.4.1	Elongated-Axis Intensity Profiles	90
5.4.2	Pattern Formation in Radial Directions	90
5.4.3	Total Scattered Power	94
5.5	Intensity Pattern Formation Conclusions	95
5.5.1	Difficulties with Comparing to Data	96
Chapter 6	Faraday Rotation at Atomic Lifetime Timescale	98
6.1	Near-Resonant Light and Atoms	99
6.1.1	Implementation Overview	100
6.2	Treatment of Dipole Response	101
6.2.1	The Polarization Components	101
6.2.2	Atomic Dipole Response	104
6.2.3	Dividing the Gas into Increments	107
6.2.4	Constraining Calculation Parameters	110
6.3	Experimental Methods	111
6.3.1	Near-Resonance Beam	112
6.4	Experimental Data and Predictions	113
6.5	Time-Dependent Response	115

6.5.1	Influences on Response Times	118
6.6	Time-Dependent Faraday Rotation Conclusions	119
Chapter 7	Radiation Transport Through an Ultracold Gas	122
Bibliography	126

LIST OF FIGURES

2.1	The average force on an atom irradiated by a red-detuned one-dimensional optical molasses, where $I/I_{sat} = .01$. The solid curve corresponds to $\delta = -2\gamma$ and the dashed curve corresponds to $\delta = -\gamma/2$. Note that the units allow the force and velocity to be represented in quantities independent of parameters specific to an atomic species. . . .	12
2.2	Spatially dependent light shifts for the ground state magnetic sublevels, $m_J = \pm 1/2$. At positions where the light is linearly polarized (lin), the sublevel energies are equal, and at positions where the light is circularly polarized (σ^+ , σ^-), the difference between the sublevel energies is maximal. An atom in motion through the polarization gradient is represented by the black solid lines with arrows on the oscillating light shift energy curves. The upward black solid arrow corresponds to an atom absorbing a photon near the top of a potential hill, and the downward blue dashed arrow corresponds to the spontaneous emission of a blue-shifted photon as the atom transitions to the lower energy ground state magnetic sublevel.	15
2.3	The average force on an atom irradiated by a red-detuned one-dimensional optical molasses in the lin \perp lin configuration, where $I/I_{sat} = .01$ and $\delta = -\gamma$. The solid curve corresponds to the average force from lin-perp-lin cooling and the dashed curve corresponds to the average force from pure Doppler cooling.	17
2.4	The average force on an atom irradiated by a red-detuned one-dimensional optical molasses in the σ^+ - σ^- configuration, where $I/I_{sat} = .01$ and $\delta = -\gamma$. The solid curve corresponds to the average force from motion-induced orientation cooling and the dashed curve corresponds to the average force from pure Doppler cooling.	19
2.5	Energy levels for a $J = 0$ to $J = 1$ transition in the presence of a weak inhomogenous linear magnetic field, $\vec{B}(z) = bz\hat{z}$. The energy levels are Zeeman shifted by an amount, $\Delta E \propto m_J z$, where the atomic resonance frequency is ω_0 and the laser frequency is ω . An atom located at $z < 0$ ($z > 0$) will scatter more σ^+ (σ^-) light on average. The position dependence of the magnetic sublevel energy shifts combined with properly polarized light leads to the radiation pressure force driving the atom toward $z = 0$	21
2.6	Three-dimensional confining potential produced by an optical dipole trap with beam parameters, $w_0 = 100 \mu\text{m}$ and $\Lambda = 10 \mu\text{m}$. A low velocity atom near the origin is trapped in an approximate three-dimensional simple harmonic oscillator potential. Note the axial and radial axes have the same units but span different ranges.	24
3.1	The D2 line for ^{85}Rb and ^{87}Rb . The resonant wavelength corresponding to the optical frequency splitting [1,2] between the $5S_{1/2}$ and $5P_{3/2}$ is 780 nm. Hyperfine structure (ground state [1] and excited state [3] splittings in ^{85}Rb , and ground state [4] and excited state [3] splittings in ^{87}Rb) within each hyperfine manifold are shown to scale (but not with respect to other manifolds or the difference between the $5S_{1/2}$ and $5P_{3/2}$ energy levels). Note the hyperfine splitting in the ground state is orders of magnitude larger than the excited state shifts.	28

3.2	Top-down view of the main elements housed inside the enclosure of a homebuilt ECDL. The labeled parts are as follows: a) an aluminum mounting plate, b) a thermistor mounted to the top of an aluminum diode laser collimation tube housing, c) a diode laser collimation tube, including diode laser and collimation optic, d) a thermoelectric device mounted beneath the aluminum mounting plate, e) the beam path of the diode laser output (rightward arrow) and the first diffraction order coupled back into the diode laser (leftward arrow), f) the zeroth diffraction order (experiment laser beam), g) a diffraction grating, h) a piezoelectric actuator mounted between a surface and adjustment screw head, i) a mechanical mirror mount with vertical and horizontal adjustment screws, j) aluminum enclosure, and k) experiment laser beam output window (wedge). The electrical connections associated with the diode laser, thermistor, thermoelectric device, and piezoelectric actuator are left out for clarity.	32
3.3	Schematic of laser beam and vapor cell arrangements used for creating signals to calibrate and lock the diode laser frequency. Part a) shows the dichroic-atomic-vapor laser lock set-up, and part b) shows the Doppler-free saturated absorption spectroscopy set-up. Part c) is adapted with permission from [5] © The Optical Society and shows the resulting signal shape produced by each type of set-up when the laser frequency is scanned over the $^{87}\text{Rb } F = 2 \rightarrow F' = 1, 2, 3$ and $^{85}\text{Rb } F = 3 \rightarrow F' = 2, 3, 4$ transitions. The labels indicate photodiodes (PD), a waveplate (WP), a polarizing beam splitter (PBS) cube, and mirrors (M). In both set-ups, the PD signals are combined such that one PD is forward-biased and the other is reverse-biased to form a difference signal.	35
3.4	Schematic of the three-dimensional MOT configuration implemented experimentally. The light-red arrows correspond to red-detuned laser beams for laser cooling, where the circular polarization of each beam is labeled. The counter-propagating laser beam pairs are mutually orthogonal and intersect at the center of the vacuum chamber. The dark-red arrows correspond to the repump laser. The black circles represent opposing magnetic coils mounted external to the vacuum (see main text), and the light-blue circle in the center represents a laser cooled and spatially confined gas of atoms. . . .	38
3.5	Radial oscillation frequency data collected via parametric heating (see main text) over a range of power modulation frequencies. The radial spatial extent is plotted and is related to the temperature of the gas. The largest spatial extent corresponds to the highest temperature gas. The blue diamonds and green circles are data collected on consecutive days. The peak position in this data indicates a radial oscillation frequency of 550 Hz.	41
3.6	Schematic of the FORT beam path through the vacuum chamber. The lens (L) before the chamber creates a beam focus external to the vacuum port. The next lens (internally mounted in the chamber) images the beam focus to the center of the vacuum, where atoms become spatially confined in the optical dipole trap. The third lens in the beam path focuses the beam to a location outside of the chamber so a mirror (M) can direct it into a beam dump. The inset shows an elongated gas of trapped ultracold atoms (light-blue) at the focus of the laser beam (outlined by dark-red curved lines). Distances are not drawn to scale.	42

3.7	Schematic showing the probe beam path through the chamber and overlapped onto the CCD camera. Before entering the chamber, the beam passes through a linear polarizer (Pol.) then a quarter waveplate to create circularly polarized light. A magnification lens (L) on the output side of the vacuum chamber images the light onto a CCD camera. The beam path is directed using a gold-plated mirror (M).	46
3.8	Pixel calibration data collected over a range of free fall times. The center-of-mass location of the ultracold gas is determined through absorption imaging performed at specified times after releasing the atoms from the trap. The x' and y' center-of-mass (c.o.m.) positions are plotted separately for clarity. The blue diamonds correspond to data and the red curves correspond to best-fit functions. In both cases, the fit function is a quadratic free fall equation with three fit parameters.	49
4.1	Depiction of a STOP cooling cycle. The light-blue oval represents confined ultracold atoms in a dark state, where the horizontal direction is the z -axis. The red represents atoms in a bright state. (a) Step 1 is the application of the laser beam (red arrow) that optically pumps atoms into a bright state. The dotted line, z_c , represents the edge of the laser overlap region where optical pumping is spatially truncated, leaving the remainder of the atoms in a dark state. (b) Step 2 is giving the bright state atoms' center-of-mass time to move to the center of the confining potential. (c) Step 3 is the application of the scattering beam (dark-blue arrow) that slows the bright state atoms' center-of-mass once it reaches the center of the confining potential. Step 4 is the application of the laser beam (light-blue arrow) that optically pumps atoms back into a dark state. The curves shown in each subfigure correspond to the bright state atoms' z -coordinate position and velocity distributions at the end of the corresponding step(s). The vertical axis for each curve is the number density of bright state atoms. Figure reproduced from [6].	57
4.2	Energy reduction per atom in the gas from a single STOP cooling cycle for a selected fraction of bright state atoms. T_i denotes the initial temperature of the gas. The blue curve corresponds to a 10% selected fraction, the green curve corresponds to a 15% selected fraction, the red curve corresponds to a 25% selected fraction, and the teal curve corresponds to a 35% selected fraction. While the calculation is performed in a one-dimensional model, the energy reduction fraction is calculated using a denominator appropriate to the total energy of a gas confined via a simple harmonic oscillator potential in three dimensions for easier comparison to experiments. Figure reproduced from [6].	61
4.3	Impact of elastic collisions on total and radial energy reduction rates (in temperature units, i.e. average energy divided by k_B) in STOP cooling. The purple circles correspond to total energy reduction rates from STOP cooling using a 10% selected fraction. The teal squares correspond to total energy reduction rates from STOP cooling using a 25% selected fraction. The blue downward triangles correspond to radial energy reduction rates from STOP cooling using a 10% selected fraction. The red upward triangles correspond to radial energy reduction rates from STOP cooling using a 25% selected fraction. Note that the horizontal and vertical axes have logarithmic scales. Figure reproduced from [6].	62

4.4	Ratio of STOP cooling total average energy reduction rate to simple evaporative cooling average energy reduction rate. The gray circles correspond to the ratio of energy reduction rates from STOP cooling using a 10% selected fraction to evaporative cooling. The blue squares correspond to the ratio of energy reduction rates from STOP cooling using a 25% selected fraction to evaporative cooling. Each ratio is determined using an equivalent time for STOP cooling and evaporation at a particular collision rate (see main text for definition of timescale used). Note that the horizontal and vertical axes have logarithmic scales.	65
4.5	Relevant energy levels for STOP cooling CaF molecules. The red solid arrow (628.5 nm) corresponds to the beam used to optically pump molecules into a bright state. The orange solid arrow (606 nm) corresponds to the scattering beam used to slow the bright state molecules' center-of-mass. The yellow solid arrow (585 nm) corresponds to the beam used to optically pump atoms into the dark state. The dotted lines correspond to spontaneous emission (606 nm). Figure reproduced from [6].	66
4.6	Schematic of the experimental set-up used to perform STOP cooling. The confining potential, up-pump beam, stop beam, and down-pump beam are pictured. The portion of the down-pump beam depicted as a dotted line is overlapped with the stop beam. The beams used to form the initial MOT and the probe beam used for absorption imaging are left out for clarity. Note that all three beams used for STOP cooling are derived from existing MOT lasers. Figure reproduced from [6].	68
4.7	One-dimensional spatial density profiles of confined atoms. O.D. is the optical depth. The blue curve is a measurement taken after STOP cooling cycles have been applied to the gas. The green curve is a measurement of atoms that have been held for an equivalent amount of time required to complete the STOP cooling cycles but without applying any cooling cycles. The red curve is a measurement taken at the beginning of a STOP cooling experiment before any cycles have been applied to the gas. Figure reproduced from [6].	71
4.8	Fractional temperature reduction resulting from the application of successive STOP cooling cycles. T_0 is the temperature of the gas when no STOP cooling cycles have been applied. T_0 is measured at an equivalent amount of time required to complete the corresponding number of STOP cooling cycles and rethermalization for a given data point (blue diamonds). ΔT is the difference between T_0 and the temperature of the gas after STOP cooling cycles have been applied. The green curve is a second-order polynomial fit to the data. Figure reproduced from [6].	72
5.1	One-dimensional spatial density profiles of bright state atoms (top) and the corresponding fraction of bright state atoms along the axial direction of the confining potential (bottom). The yellow spatial density profiles are when the entire confined gas is optically pumped into the bright state. The other curves are when only the edge of the confined ultracold gas is optically pumped into the bright state. The length of time the up-pump beam is applied is shown in the inset legend. The frequency of the up-pump beam is below resonance (red-detuned) on the left and increases to above resonance (blue-detuned) on the right.	80

5.2	Normalized Gaussian spatial density distribution along the (a) axial direction and (b) radial directions. The horizontal axis for the axial distribution extends from $z = -5\sigma_z$ to $z = 5\sigma_z$. The horizontal axis for the radial distribution extends from $r = 0$ to $r = 5\sigma_r$. These plots were included to allow for ease of comparison between the density of atoms at a given position with the amount of light intensity predicted (shown in later figures) to be at that same position. Figure reproduced from [7].	83
5.3	Beer-Lambert-law-based calculations of the optical depth (O.D.) along the long central axis of an elongated trapped ultracold gas. The variation in calculated O.D. with detuning is shown. The O.D. is determined by integrating along the axial length of the gas as described in the main text. The resonant wavelength is 780 nm. The green curve corresponds to a peak spatial density of 10^{11} cm^{-3} and the blue curve corresponds to a peak spatial density of 10^{12} cm^{-3} . Note that the vertical axis has a logarithmic scale. Figure reproduced from [7].	84
5.4	Beer-Lambert law predictions for the intensity of light propagating through the model system with a peak spatial density of (a) 10^{11} cm^{-3} and (b) 10^{12} cm^{-3} . The initial position is $z = -3.5 \text{ mm}$ (well outside of the volume with significant gas density). The blue curve is 0Γ detuning, green is $\pm 3\Gamma$, red is $\pm 6\Gamma$, and teal is $\pm 9\Gamma$, where Γ is the natural linewidth of the resonance transition. Figure reproduced from [7].	84
5.5	Schematic of a plane wave (red) encountering an ultracold gas (blue) of two-level atoms. The axial positions $z_0, z_1, z_2, z_3,$ and z_4 identify the locations of evenly spaced planes perpendicular to the light propagation direction in the spatial density distribution (see main text). Figure reproduced from [7].	86
5.6	Wave propagation model predictions for the intensity along the elongated axis of the spatial density distribution. The plots (a) and (b) both have a peak spatial density of 10^{11} cm^{-3} . The plots (c) and (d) both have a peak spatial density of 10^{12} cm^{-3} . The blue curve for all four plots is 0Γ detuning. For (a) and (c) the green curve is $+3\Gamma$, red is $+6\Gamma$, and teal is $+9\Gamma$. For (b) and (d) the green curve is -3Γ , red is -6Γ , and teal is -9Γ . Note that the vertical axis scale for (a)-(c) is different than the vertical axis scale for (d). Figure reproduced from [7].	91
5.7	Intensity patterns located at evenly-spaced planes perpendicular to the axis of propagation for a peak spatial density of 10^{12} cm^{-3} . (a)-(d) correspond to a frequency detuning of $+6\Gamma$ and (e)-(h) correspond to a frequency detuning of -6Γ . The planes are located at $z_1 = -1.75 \text{ mm}$, $z_2 = 0$, $z_3 = 1.75 \text{ mm}$, and $z_4 = 3.5 \text{ mm}$. The horizontal and vertical widths are equal to $16\sigma_r$ for all of the subfigures. Figure reproduced from [7].	92
5.8	Intensity patterns formed in a plane that intersects the central elongated axis of the spatial density distribution for a peak spatial density of 10^{12} cm^{-3} . (a) corresponds to a frequency detuning of $+6\Gamma$ and (b) corresponds to a frequency detuning of -6Γ . The horizontal axes are parallel to the axis of propagation and the tick marks are located at $z_1 = -1.75 \text{ mm}$, $z_2 = 0$, $z_3 = 1.75 \text{ mm}$, and $z_4 = 3.5 \text{ mm}$. The vertical width is equal to $16\sigma_r$ (aspect ratio not to scale) and the center of the vertical axis is $r = 0$ for both subfigures. Figure reproduced from [7].	92

5.9	Radial plot of intensity patterns formed during propagation through the model system with a peak spatial density of 10^{12} cm^{-3} . The horizontal axis extends out to $5\sigma_r$, where $r = 0$ lies on the elongated central axis of the gas. The peak spatial density is 10^{12} cm^{-3} and the frequency detuning is -6Γ . The blue curve corresponds to the radial intensity at $z = 0$, the green curve corresponds to $z = 1.498 \text{ mm}$, and the red curve corresponds to $z = 3.5 \text{ mm}$. Figure reproduced from [7].	93
5.10	Normalized scattered power as a plane wave propagates through the model system with a peak spatial density of 10^{12} cm^{-3} . The blue curve is $+6\Gamma$ and red is -6Γ . The green curve is the prediction from the Beer-Lambert law for $\pm 6\Gamma$. Figure reproduced from [7].	95
6.1	Relevant energy levels for our theoretical calculations and experimental measurements of the time-dependent Faraday rotation of light in an ultracold gas. The incident light is composed of equal parts σ^+ and σ^- circular polarization and is represented by the red arrow(s). Part (a) shows the hyperfine structure in the D2 (780 nm) line in ^{85}Rb (the ground state [1] and excited state [3] splittings are not to scale). Polarized light is driving the $5S_{1/2} F = 3$ to $5P_{3/2} F = 4$ cycling transition. Part (b) depicts the magnetic sublevels in the $5S_{1/2} F = 3$ ground state and $5P_{3/2} F = 4$ excited state. The gray lines represent the degenerate (no magnetic field) magnetic sublevels and the black lines represent the Zeeman-shifted sublevels. Two examples of the σ^+ and σ^- polarization components are shown with different amounts of detuning resulting from the energy shifts. Figure reproduced from [8].	102
6.2	Time-dependent optical depth (blue solid curve) and time-dependent phase (black dashed curve) of the transmitted σ^+ polarization component through an optically thin gas of atoms driven on a simple $F = 0$ to $F = 1$ transition, where $A'_+ = .01\gamma$ and $\eta = 1$. The magnitude of the induced detuning in the calculations is $ \delta = 1.0\gamma$. The blue (black) dotted vertical line indicates the time when the optical depth (phase response) reaches its maximum. Subfigure (a) shows the curves plotted on the same horizontal axis, with a clear separation between the times corresponding to the maximum of each curve. Subfigure (b) shows that when the phase response is plotted with respect to the bottom horizontal axis and the optical depth is plotted with respect to a separate horizontal axis scaled by a factor of 2 (shown on top of the subfigure), the dotted vertical lines exactly overlap. Note that the vertical axis is a normalized scale. Figure reproduced from [8].	106
6.3	Phase response for an optically thin gas of atoms driven on a simple $F = 0$ to $F = 1$ transition with a large detuning, $ \delta = 20\gamma$. Figure reproduced from [8].	106

6.4	Time-dependent optical depth (blue solid curve) and time-dependent phase (black dashed curve) of the transmitted σ^+ light through an optically thin gas of multi-level atoms driven on an $F = 3$ to $F = 4$ transition in the presence of increasing applied magnetic field strengths. The ground state magnetic sublevels have initial populations that are evenly distributed. The optical depth is plotted with respect to the top horizontal axis and the phase response is plotted with respect to the bottom horizontal axis. The subfigures (a)-(c) are the results when the magnitude of the magnetic field induced detuning for the outermost allowed transition between ground and excited state magnetic sublevels is (a) $ \delta = 0.5\gamma$, (b) $ \delta = 1.0\gamma$, and (c) $ \delta = 1.5\gamma$. The blue (black) dotted vertical line indicates the time when the optical depth (phase response) reaches its maximum. Figure reproduced from [8].	108
6.5	Schematic depicting the experimental set-up used to measure the time-dependent Faraday rotation in an ultracold gas. The beams used to form the initial MOT are left out for clarity. Note that the near-resonance beam has a turn-on time that is faster than the excited state lifetime of the atoms. Figure reproduced from [8].	112
6.6	Experimental data and theoretical calculations in the presence of a $B = 1.3$ Gauss magnetic field along the axis of light propagation. Subfigure (a) is data and predictions when the quarter waveplate's fast axis is positioned at 0° , and subfigure (b) is data and predictions when the quarter waveplate's fast axis is positioned at 45° . The yellow and blue data are measurements collected on detector 1 and 2, respectively. The black and red curves are the predicted transmission corresponding to the light on detector 1 and 2, respectively. Figure reproduced from [8].	114
6.7	The same type of data as shown in figure 6.6, except $B = 4.4$ Gauss. Figure reproduced from [8].	115
6.8	The same type of data as shown in figure 6.6, except $B = 6.2$ Gauss. Figure reproduced from [8].	116
6.9	Time-dependent optical depth (blue solid curve) and time-dependent phase difference (black dashed curve) calculated from the theory curves of figures 6.6-6.8. The optical depth is plotted with respect to the top horizontal axis and the phase response is plotted with respect to the bottom horizontal axis. The subfigures (a)-(c) are the results when the magnitude of the magnetic field quantization axis is (a) $B = 1.3$ Gauss, (b) $B = 4.4$ Gauss, and (c) $B = 6.2$ Gauss. The blue (black) dotted vertical line corresponds to the time when the optical depth (phase response) reaches its maximum. Figure reproduced from [8].	117
6.10	Time-dependent magnitude of the σ^+ polarization component dipole amplitude in the first (green dashed curve) and last (red solid curve) increment of a calculation using 20 increments in the z -direction. The last increment corresponds to the side of the gas opposite to the incident light. The calculation is performed in the low-intensity ($I \ll I_{sat}$) limit with zero detuning and no magnetic field. The ground state magnetic sublevels have initial populations that are evenly distributed. The subfigures (a)-(c) are the results when the optical depth is (a) O.D. = 0.06, (b) O.D. = 1.2, and (c) O.D. = 2.4. The curves in each subfigure are normalized to the maximum dipole amplitude value in the first increment for easier comparison between subfigures.	120

7.1	Relevant energy levels for the resonant photon excitations and ionization pulse used in the radiation transport measurement technique.	123
7.2	Schematic of the resonant laser beams and ionization laser pulse used in the radiation transport measurement technique. Part a) shows the application of the 780 nm laser beam (light red) used to excite atoms (light blue circle) from the $5S_{1/2}$ ground state to the $5P_{3/2}$ excited state. Part b) shows the application of the 776 nm laser beam (dark blue) used to excite atoms from the $5P_{3/2}$ excited state to the $5D_{5/2}$ excited state. Also shown is the 1064 nm ionization pulse (bronze) propagating along a direction that passes through the center of the gas. Part c) shows the resulting ions being accelerated toward the micro-channel plate (MCP) detector. The dotted vertical lines correspond to voltage grids and the voltages will be approximately $V_1 = +10$ V, $V_2 = -10$ V, and $V_3 = -200$ V.	124

Chapter 1

Introduction

Atoms have physical properties that can be manipulated by the application of a drive frequency in the form of coherent electromagnetic radiation. For particular drive frequencies, there is a peaked response corresponding to an atomic resonance. Phenomena associated with near-resonant and resonant atom-light interactions are most easily studied when atoms are moving slowly. As such, ultracold gases provide a near-ideal test bed to investigate fundamental physics, where the effects of atom-light interactions lead to pronounced observable responses. The experimental and theoretical work presented in this dissertation is a compilation of three research projects that are connected by the main subject of near-resonant and resonant light in ultracold gases. First, we performed an experimental implementation and theoretical evaluation of a completely new laser cooling technique for atoms or molecules confined in a trapping potential [6]. These experiments resulted in a nearly 30% temperature reduction of a confined ultracold gas of ^{87}Rb atoms. Next, we developed a numerical model to predict the behavior of near-resonant light in an elongated ultracold gas [7]. These calculations produced the surprising result that under particular conditions, over an order of magnitude increase in intensity can arise inside of the gas. Such an increase is astonishing when the optical thickness (characterized by the absorption of light) of the gas is considered. Lastly, our numerical work on intensity variations in ultracold gases stimulated a new research direction for our group that included experimental and theoretical studies of the time-dependence of the opacity and indices of refraction of an ultracold gas of ^{85}Rb atoms at times shorter than the D2 line atomic excited state lifetime [8]. We found that the peak response times associated with opacity and polarization rotation depend strongly on physical parameters in the system. An accurate description of the time-dependent response of the gas does not generally match simple expectations, and requires careful modeling of the system.

1.1 Background

The focus of my first project (chapter 4) was the continued development of a novel laser cooling technique originally proposed by my advisor and one of his previous graduate students. Upon joining the research group, my first task was to get the experimental apparatus back in working order so we could continue to study the new cooling technique. This included diagnosing and fixing experimental hardware (e.g. lasers, circuits, electrical connections) and adding more control electronics (e.g. digital switches, amplifiers, function generators). In addition, the number of diode lasers used for the experiment was reduced from five to two, which required all new beam paths and characterization of those beams. For the most part, this went smoothly. However, during the alignment of a particular laser beam needed for one of the steps in the cooling scheme, we encountered unexpected signals in a subset of the collected data. The anomalous signals ultimately prompted us to take a slight detour away from our laser cooling studies.

The temporary deviation in our research path led to my second project (chapter 5), which focused on developing a model to numerically calculate the intensity variations of near-resonant light propagated through a trapped gas representative of those used in our laser cooling scheme. While the gradient in the spatial number density of atoms in those systems was expected to have an effect, we were surprised to find realistic conditions produced large increases in light intensity inside of an optically thick (model) system. The predicted spatial light intensity patterns that formed in the gas motivated us to consider how we could study radiation transport physics associated with a source of resonant light originating inside of an optically thick gas. In particular, how that light would propagate outward through the gas during timescales less-than and on the order of an atomic excited state lifetime. Before heading in a new research direction, we returned to our novel laser cooling technique and completed measurements that definitively demonstrated the cooling technique does indeed work. We also performed additional calculations to understand possible sources of cooling efficiency loss in our experiments.

After wrapping up our work on the cooling technique, we directed our research focus on studying radiation transport physics in optically thick gases at timescales on the order of an atomic

excited state lifetime. In the simplest of terms, we wanted to place a source of resonant light at the center of an ultracold gas and observe how that energy propagated through the system until finally escaping. The proposed detection scheme (chapter 7) was going to require significant changes to our existing apparatus. We took a pause to consider what measurements were possible with our existing apparatus that would better our understanding of what to expect in the proposed experiments. This led to my third and final project (chapter 6). The main thrust of the last project was to measure the transmitted intensity and polarization of a near-resonant laser beam over timescales on the order of an atomic excited state lifetime after the beam had propagated through an optically thick ultracold gas. The measured signals were compared to theoretical predictions and good agreement was obtained. Addressing and overcoming the challenges that came up during the experimental implementation and theoretical calculations explored numerous physics and technical considerations necessary for future research to be performed by our group.

1.2 Overview

The following sections provide short summaries of the content presented in each chapter of this dissertation. First is a chapter intended as an introduction to laser cooling and trapping concepts that are relevant to the techniques we use to produce and confine ultracold gases in our experiments. The next chapter is a description of the general experimental apparatus hardware and methods that are commonly used throughout our experiments. After discussing the apparatus, the following three chapters consist of detailed descriptions of the three projects that constitute the bulk of research conducted for this dissertation. Lastly, there is a brief chapter describing a proposed measurement technique for radiation transport experiments that will be performed by our research group in the near future.

1.2.1 Laser Cooling and Trapping Atoms (Chapter 2)

Chapter 2 discusses atom-light interactions relevant to the laser cooling and trapping schemes used in our experiments. The chapter begins with a description of Doppler cooling [9], which has

a lowest achievable temperature known as the Doppler cooling limit [10–13]. Once a gas has been cooled to temperatures near the Doppler cooling limit, other mechanisms that are able to cool the gas to even lower temperatures [14–16] become necessary for further cooling. These are aptly referred to as sub-Doppler cooling mechanisms. Specifically, lin-perp-lin cooling and motion-induced orientation cooling are described [17–20]. After introducing the concepts behind laser cooling atoms to ultracold temperatures, a description of how these atoms are spatially confined is presented. The two spatially confining traps discussed will be a magneto-optical trap [21–24] and an optical dipole trap [25–27]. The former combines laser cooling with a magnetic field so that atoms experience a viscous velocity damping force and a spatial restoring force in a small region of space. The latter operates in the absence of any laser cooling mechanisms such that the atoms are spatially confined by an approximately conservative force.

1.2.2 General Experimental Apparatus (Chapter 3)

Chapter 3 provides a description of the hardware and techniques used to produce and characterize ultracold gases in our experiments. All of our experiments are performed using either ^{85}Rb or ^{87}Rb , so the relevant energy levels [1–4] for those species are presented. This is followed by a description of the type of vacuum chamber we use, along with how the necessary vacuum pressures are reached. The arrangement and operation of our "homebuilt" lasers is then presented, which when used with the vacuum chamber and magnetic coils, provide the main apparatus components needed to produce ultracold gases for our experiments. In addition to the lasers used for manipulating the atoms with near-resonance light, we often use a high-powered CW laser to spatially confine atoms using far-off resonance light. This optical dipole trap is discussed, and then the imaging technique used to characterize our ultracold gases is described. Lastly, some of our experiments measure light intensity transmitted through an ultracold gas as a function of time. Data collection for those experiments require a different detection scheme than the absorption imaging set-up, so details of the necessary additional detectors and electronics are presented. Much of the

apparatus hardware is descendent from past experiments performed by previous members of our research group, and is well-documented in those student dissertations [28–30].

1.2.3 Spatially Truncated Optical Pumping Cooling (Chapter 4)

Chapter 4 presents our theoretical and experimental work in developing a novel laser cooling technique for ultracold atoms trapped in a confining potential. We call the technique "spatially truncated optical pumping (STOP) cooling" [6]. STOP cooling uses the fact that the internal states of atoms can be manipulated by laser light such that high energy atoms can be preferentially selected and then slowed to achieve cooling. The research presented in this chapter builds on the groundwork laid by a previous graduate student whose efforts provided the first indications of STOP cooling's viability [30]. For those experiments, the temperature reduction from applying STOP cooling to a gas of trapped atoms was inferred through indirect calculations rather than being explicitly measured. This was due to constraints imposed by unfavorable vacuum conditions. The implementation of the cooling technique presented in this dissertation resulted in a direct measurement of temperature reduction, including the temperature reduction from applying STOP cooling multiple times to a confined ultracold gas. Each application of STOP cooling involves four steps that are collectively referred to as a "cycle." Our experiments resulted in a $0.0091(5)$ fractional single-cycle temperature reduction and a $0.282(4)$ fractional temperature reduction from 60 cycles. In addition to conducting new experiments under improved vacuum conditions, we performed additional calculations, too. These included the impact of collisions, a comparison to a collision-based cooling mechanism, and the effect of using a realistic three-dimensional confining potential. By numerically modeling imperfections in the experimental system, we were able to identify where improvements could be made to realize further temperature reduction. A description of the calculations, experiments, and results are presented, along with several proposed improvements to the apparatus that are expected to further increase the technique's cooling efficiency.

1.2.4 Intensity Pattern Formation in a Trapped Gas (Chapter 5)

Chapter 5 describes unanticipated signals seen during our STOP cooling experiments, and the ensuing numerical calculations used to predict intensity pattern formations resulting from a near-resonant plane wave propagating through an elongated model gas of two-level atoms. These Maxwell's equations-based calculations show that the wave nature of light coupled with the dimensions and spatial density distribution of confined ultracold atoms can lead to large intensity variations inside of an elongated gas [7]. We perform the calculations using parameters representative of physical quantities (e.g. density, spatial dimensions) similar to those found in our experimentally confined ultracold gases. The main features of the predicted intensity variations depend on whether the near-resonant light is above (+) or below (−) the resonance frequency of the atoms. For example, light with a frequency below resonance will undergo a focusing effect that can lead to over an order of magnitude larger light intensity inside of the gas as compared to the incident intensity. The resulting increase in light intensity along the elongated axis is surprising given the expected absorptive nature of the gas. Conversely, light with a frequency above resonance experiences a defocusing effect that can lead to a dramatic decrease in light intensity along the elongated axis of the gas. The results of these frequency-dependent calculations are in disagreement with predictions of near-resonant light intensity as a function of elongated axis position that result from a standard treatment using the Beer-Lambert law. In addition, significant radially-varying intensity patterns can form in planes perpendicular to the direction of light propagation for both signs of light frequency. These on and off-axis intensity variations would need to be carefully considered in actual experiments that require accurate descriptions of light intensity in comparable systems. A description of the numerical model is presented, along with results from calculations using parameters similar to the elongated gases found in our STOP cooling experiments.

1.2.5 Faraday Rotation at Atomic Lifetime Timescale (Chapter 6)

Chapter 6 details theoretical predictions and experimental measurements of the time-dependent development of opacity and Faraday rotation in an ultracold gas over timescales on the order of an

atomic excited state lifetime [8]. When a gas of atoms is suddenly illuminated with near-resonant light, the atoms cannot respond instantaneously. This results in an initial period of transparency while the light absorption takes time to develop over a timescale set by the atomic excited state lifetime. The atoms' non-instantaneous response means the index of refraction also takes time to develop, and the associated phase response is expected to develop slower than absorption effects. When the gas has differing indices of refraction for orthogonal circular light polarization components, a polarization rotation of the light can occur. Faraday rotation is one manifestation of this. We have performed experimental measurements and theoretically described the time-dependent development of polarization rotation in an ultracold gas subjected to an applied magnetic field (i.e. Faraday rotation), and good agreement between experimental results and theoretical predictions was obtained. The resulting timescale associated with the phase response is indeed slower than that of absorption. However, the actual situation is more complicated than a simple factor of 2 estimate between the absorption and phase response timescales and involves multiple factors that affect the timescales in ways that make general characterizations difficult. These factors include the incident light intensity, the incident light frequency detuning, and the magnitude of the applied magnetic field. In addition, we identify an optical thickness effect that also influences the response timescale. In an optically thick gas, atoms on the opposite side of the gas from the incident light are driven toward their steady-state response faster than they would be in an optically thinner gas. This physics is relevant for applications or experiments that use rapidly applied near-resonant light pulses in similar systems, especially those in which timings and phase shifts are important.

1.2.6 Radiation Transport Through an Ultracold Gas (Chapter 7)

Chapter 7 discusses the main details of a new detection scheme for radiation transport experiments planned for future work in our research group. The proposed detection scheme combines laser manipulation of the internal states of atoms with a device designed to detect charged particles. By allowing the light associated with the radiation transport physics we are interested in studying to excite atoms in an ultracold gas, the location of those atoms can be detected. This will be done

by ionizing the excited atoms, and the resulting ions will be accelerated to the detector. The spatial information coupled with different timings between laser pulses will provide a measurement technique capable of "looking inside" of an ultracold gas as resonant light propagates outward. The focus of this chapter will be to provide a sense of the general set-up, including the atomic energy levels and excitation wavelengths involved.

Chapter 2

Laser Cooling and Trapping Atoms

The purpose of this chapter is to introduce concepts necessary for understanding the laser cooling and trapping techniques used for the experimental work presented in this dissertation. There are a large number of different laser cooling schemes, and extensive work has been performed by the laser cooling community in describing the common ones presented in this chapter. Therefore, the following sections are intended to provide just an overview of the most basic physics of cooling techniques used in our research. Our experiments generally involve gases of atoms with temperatures on the order of 10 - 100 μK . These ultracold temperatures are achieved by using atom-light interactions to reduce the average energy of atoms in a gas. The primary cooling mechanisms relevant for producing the ultracold gases used for our experiments are categorized as Doppler cooling and sub-Doppler cooling, both of which will be described in this chapter. In addition to cooling the atoms, our experiments require spatial confinement of the gas, either during preparation stages, or for the entire duration of an experiment. The first type of confining trap that will be described uses a combination of lasers and an applied magnetic field and is known as a magneto-optical trap. The second type of confining trap that will be presented is purely light based and is known as an optical dipole trap.

2.1 Doppler Cooling Atoms

An effective and straightforward technique for laser cooling atoms is the method of Doppler cooling [9]. Given a gas of atoms whose thermal motion is described by a velocity distribution (e.g. Maxwell-Boltzmann velocity distribution), Doppler cooling works by slowing a subset of those atoms that are moving within a particular velocity range. The basic idea is to take advantage of the Doppler frequency shift of near-resonant light as measured from a moving atom's reference frame. This is routinely implemented in multiple dimensions but is most easily described in a one-dimensional configuration.

Consider a two-level atom in motion along the \hat{z} -direction and illuminated with low-intensity counter-propagating laser beams of the same frequency, ω , in the lab frame. In the atom's reference frame, the laser beam that the atom is moving toward will have a frequency that appears higher (blue-shifted) than ω , and the laser beam that the atom is moving away from will have a frequency that appears lower (red-shifted) than ω . An appropriate choice of laser frequency (red-detuning) in the lab frame leads to more photons being scattered (i.e. photon absorption and spontaneous emission) on average from the laser beam that the atom is traveling toward than the laser beam that the atom is traveling away from. This can be understood by examining the total scattering rate of light for an atom in motion with velocity, \vec{v} , and illuminated by a plane wave with frequency, ω . The frequency and velocity dependent total scattering rate can be expressed as [31]

$$R = \frac{\gamma}{2} \left(\frac{I/I_{sat}}{1 + I/I_{sat} + 4 \left(\frac{\delta - \vec{k} \cdot \vec{v}}{\gamma} \right)^2} \right), \quad (2.1)$$

where $\gamma = \tau^{-1}$ and τ is the excited state lifetime of the atomic transition, δ is the frequency detuning ($\delta = \omega - \omega_0$, where ω_0 is the atomic resonance), \vec{k} is the wavevector ($\|\vec{k}\| = k = 2\pi/\lambda$, where λ is the wavelength), I is the intensity of the light, and I_{sat} is the saturation intensity ($I_{sat} \equiv 2\pi^2\hbar c/(3\lambda^3\tau)$, where \hbar is the reduced Planck constant, and c is the vacuum speed of light). The functional form of (2.1) is a Lorentzian centered at $\delta - \vec{k} \cdot \vec{v} = 0$. Choosing the frequency of light to be red-detuned ($\delta < 0$) with respect to ω_0 leads to the atom scattering more photons on average from a beam it is moving toward ($\vec{k} \cdot \vec{v} = -\|\vec{k}\|\|\vec{v}\|$) as compared to a beam it is moving away from ($\vec{k} \cdot \vec{v} = \|\vec{k}\|\|\vec{v}\|$) for suitably low velocities.

Each photon carries $\hbar\vec{k}$ of momentum, so the process of photon absorption by an atom results in a momentum transfer to the atom. This is followed by the atom spontaneously emitting a photon in a random direction and undergoing a momentum recoil opposite to that random direction. When this photon scattering process occurs many times, the net momentum change from spontaneous emission events averages to zero. The remaining average momentum change from the absorption

events is in the direction of \vec{k} which results in an average radiation pressure force on the atom that can be expressed as [17]

$$\vec{F}_{sp} = \hbar\vec{k}R = \frac{\hbar\vec{k}\gamma}{2} \left(\frac{I/I_{sat}}{1 + I/I_{sat} + 4 \left(\frac{\delta - \vec{k} \cdot \vec{v}}{\gamma} \right)^2} \right). \quad (2.2)$$

It is worth noting that (2.2) cannot be made arbitrarily large by increasing the intensity without bound. This is a consequence of the I/I_{sat} term in the denominator and corresponds to the excited state population of the two-level transition saturating such that half of the atoms in a gas are in the excited state. For an atom illuminated by low-intensity (i.e. $I/I_{sat} \ll 1$) counter-propagating laser beams such that stimulated emission events can be neglected, the average force on the atom can be expressed as

$$\vec{F} = \frac{\hbar k\gamma}{2} \left(\frac{I/I_{sat}}{1 + I/I_{sat} + 4 \left(\frac{\delta - \vec{k} \cdot \vec{v}}{\gamma} \right)^2} - \frac{I/I_{sat}}{1 + I/I_{sat} + 4 \left(\frac{\delta + \vec{k} \cdot \vec{v}}{\gamma} \right)^2} \right) \hat{z}. \quad (2.3)$$

where $\vec{k} = k\hat{z}$ in (2.3). When the laser frequency is red-detuned from the atomic resonance, the counter-propagating beams provide a velocity-dependent viscous force opposite to the atom motion. This configuration creates what is known as a one-dimensional optical molasses [17–20]. The optical molasses can be implemented in three dimensions by arranging orthogonally intersecting pairs of counter-propagating laser beams [32, 33]. The average force as a function of atom velocity for a low-intensity one-dimensional optical molasses is shown in figure 2.1.

Figure 2.1 indicates that the one-dimensional force an atom experiences is linearly dependent on the atom velocity between $\pm\|\vec{v}\| \simeq \gamma/k$, known as the (approximate) velocity capture range for Doppler cooling [17, 18]. This definition of the capture range is in line with early work in the field.

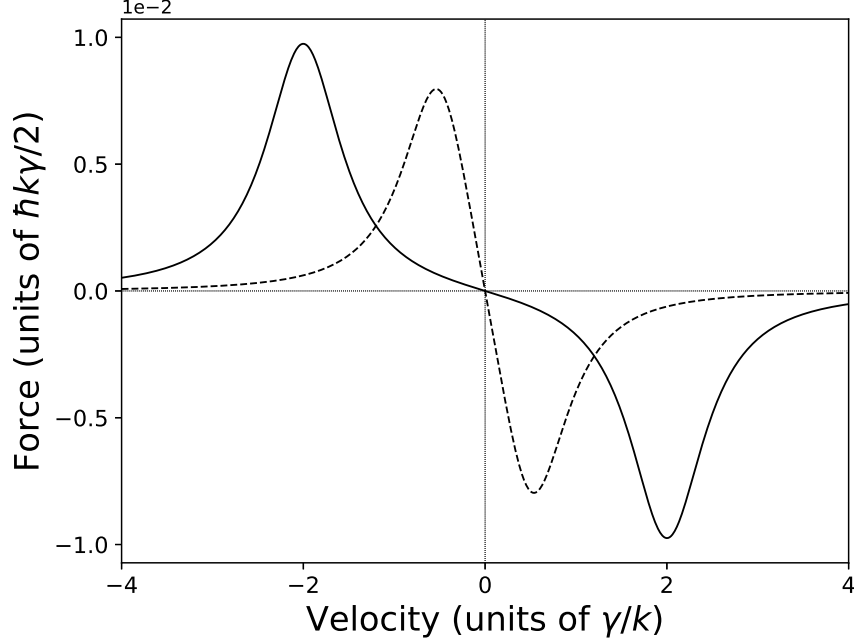


Figure 2.1: The average force on an atom irradiated by a red-detuned one-dimensional optical molasses, where $I/I_{sat} = .01$. The solid curve corresponds to $\delta = -2\gamma$ and the dashed curve corresponds to $\delta = -\gamma/2$. Note that the units allow the force and velocity to be represented in quantities independent of parameters specific to an atomic species.

The basic physics presented in the remainder of this chapter will identify other capture ranges as first described in early literature as well. In general for many typical configurations, that will be approximately equal to the linear region of the cooling force [34]. More recently, the capture range tends to be defined in the context of a stopping length. This is because the capture range is really a function of the distance over which an atom could be brought to rest.

The validity of treating the velocity in (2.3) as a quasi-continuous variable depends on the amount of momentum change imparted to an atom during an absorption or spontaneous emission event. The magnitude of the recoil velocity, $\|\vec{v}_R\| = v_R = \hbar k/M$, must be such that $kv_R \ll \gamma$ [17]. Rubidium is an example of an atomic species for which this recoil velocity Doppler shift condition is valid. For a Rb atom illuminated by 780 nm wavelength light (D2 line), the Doppler shift imparted by a photon absorption or spontaneous emission event is $kv_R/(2\pi) \approx 8$ kHz, which is a negligible fraction of the natural linewidth (i.e. $\Gamma \equiv (2\pi\tau)^{-1} = 6$ MHz). The recoil momentum is also important when predicting the lowest achievable temperature from Doppler cooling.

Scattering many photons in an optical molasses introduces statistical heating (i.e. random thermal motion) acquired from the random direction of spontaneous emission events. The Doppler cooling limit [10–13] in equilibrium is expressed as $k_{\text{B}}T_{\text{D}} = \hbar\gamma/2$, where k_{B} is Boltzmann’s constant and T_{D} represents the minimum Doppler temperature. For a sense of scale, the Doppler cooling limit for Rb being cooled on the D2 line is $\approx 140 \mu\text{K}$, corresponding to a root-mean-square (RMS) speed of $v_{\text{rms}} \sim 10 \text{ cm s}^{-1}$.

2.2 Sub-Doppler Cooling Atoms

Laser cooling below the Doppler cooling limit is possible through additional mechanisms referred to as polarization gradient cooling [17–20], among other possibilities [35–38]. The theoretical description of polarization gradient cooling relies on a multilevel atom traveling through a spatially varying polarization landscape produced by counter-propagating laser beams with different polarizations. The interaction of the light with the internal structure (i.e. hyperfine and magnetic sublevels) of an atom can result in temperatures that are less than the Doppler cooling limit [14–16]. The two types of polarization gradient cooling described in this section were originally named ellipticity-gradient cooling and polarization-rotation cooling [17], but are now more commonly referred to as lin-perp-lin cooling and motion-induced orientation cooling, respectively. For simplicity, the descriptions will be for a low-intensity one-dimensional optical molasses, with the emphasis being on the ability to reach sub-Doppler temperatures.

2.2.1 Lin-Perp-Lin Cooling

Lin-perp-lin cooling depends on overlapping counter-propagating laser beams of the same frequency, ω , such that one beam is linearly polarized in an \hat{e}_1 direction and the other beam is linearly polarized in an \hat{e}_2 direction, where $\hat{e}_1 \cdot \hat{e}_2 = 0$. This is known as the lin-perp-lin (or $\text{lin} \perp \text{lin}$) configuration [18]. Assuming plane wave solutions of equal amplitude counter-propagating along the \hat{z} -direction and letting $\hat{e}_1, \hat{e}_2 \rightarrow \hat{x}, \hat{y}$, the superposition of the electric fields can be expressed as

$$\vec{E} = E_0[(\hat{x} + \hat{y}) \cos \omega t \cos kz + (\hat{x} - \hat{y}) \sin \omega t \sin kz], \quad (2.4)$$

where E_0 is a real amplitude, t is time, and $k = 2\pi/\lambda$ is the wavenumber. Beginning at $z = 0$, positions spaced by quarter-wavelength increments (i.e. $z = 0, \lambda/4, \lambda/2, \dots$) have a total field that is linearly polarized at a different angle ($\pi/2$ change every quarter wavelength) with respect to the \hat{x} -direction. Half-way between those quarter-wavelength increments (i.e. $z = \lambda/8, 3\lambda/8, \dots$), the total field is circularly polarized (σ^+, σ^-) with alternating handedness depending on position. Along the axis of propagation, the polarization changes from linear to σ^- circular to linear to σ^+ circular in less than half a wavelength.

A description of how this gradient of ellipticity leads to sub-Doppler cooling requires including the internal structure of a multilevel atom. A simple transition that can be used to describe sub-Doppler cooling in the lin \perp lin configuration is a $J = 1/2$ to $J = 3/2$ transition ($J = L + S$ is the total angular momentum, where L is the orbital angular momentum, and S is the spin angular momentum) [18]. The $J = 1/2$ ground state has magnetic sublevels, $m_J = \pm 1/2$, and the $J = 3/2$ excited state has magnetic sublevels, $m_J = \pm 1/2, \pm 3/2$ (where the sublevels are denoted by their quantum numbers; see figure 2.2). Dipole allowed transitions between the ground state sublevels and excited state sublevels are those that result in $\Delta m = 0, \pm 1$, where $\Delta m = 0$ corresponds to transitions from linearly polarized light, $\Delta m = +1$ corresponds to transitions from σ^+ light, and $\Delta m = -1$ corresponds to transitions from σ^- light. In addition to the sublevel transitions that occur from the atom-light interaction, there are energy shifts (i.e. AC Stark shifts [39], otherwise known as light shifts) of the magnetic sublevels due to the presence of the driving field. The light shifts of the ground state magnetic sublevels due to counter-propagating laser beams of equal low-intensity can be expressed as [31]

$$\Delta E_g = \frac{\hbar \delta (I/I_{sat}) C_{ge}^2}{1 + 4 \left(\frac{\delta}{\gamma} \right)^2}, \quad (2.5)$$

where C_{ge} is the Clebsch-Gordan (CG) coupling coefficient between the atom and light for a particular transition between a ground state sublevel, g , and excited state sublevel, e . The CG coefficient

depends on the polarization of the local driving field and the quantum numbers of the magnetic sublevels involved in the transition. This means an atom in a ground state magnetic sublevel moving through the $\text{lin} \perp \text{lin}$ polarization landscape will undergo light shifts that have an oscillatory spatial dependence, as shown in figure 2.2.

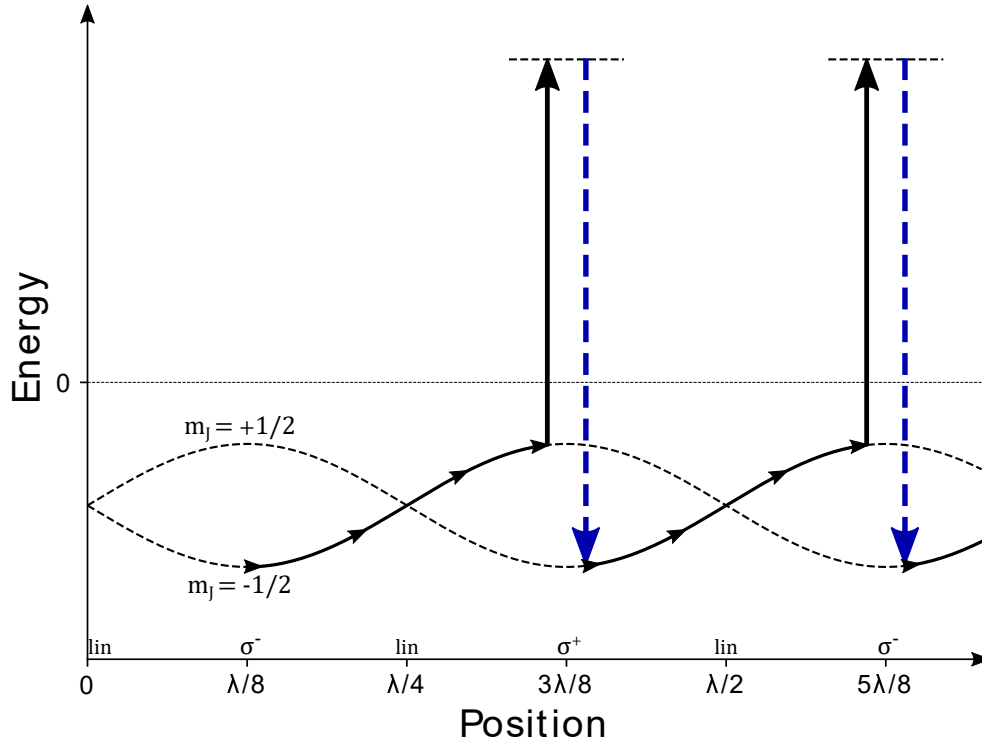


Figure 2.2: Spatially dependent light shifts for the ground state magnetic sublevels, $m_J = \pm 1/2$. At positions where the light is linearly polarized (lin), the sublevel energies are equal, and at positions where the light is circularly polarized (σ^+ , σ^-), the difference between the sublevel energies is maximal. An atom in motion through the polarization gradient is represented by the black solid lines with arrows on the oscillating light shift energy curves. The upward black solid arrow corresponds to an atom absorbing a photon near the top of a potential hill, and the downward blue dashed arrow corresponds to the spontaneous emission of a blue-shifted photon as the atom transitions to the lower energy ground state magnetic sublevel.

When the atom moves from a position where the light shift is the largest to a position where the light shift is the smallest (in absolute value), the internal energy of the atom increases through a reduction of its kinetic energy (for $\delta < 0$). The atom will absorb more photons on average at positions where it is moving the slowest, and the CG coefficients are such that spontaneous emission into the lower energy ground state magnetic sublevel is most probable. This results in a

spontaneous anti-Stokes Raman photon [18, 19], where the additional energy of the emitted photon corresponds to the difference between the AC Stark shifts of the ground state magnetic sublevels. As the atom continues to move through the polarization gradient, it will again convert kinetic energy to potential energy, then dissipate some or all of that internal energy difference through absorption and spontaneous emission. The continual climbing of potential hills at the expense of kinetic energy is the reason this cooling mechanism is also known as Sisyphus laser cooling [40], in reference to Greek mythology.

For the $J = 1/2$ to $J = 3/2$ transition, an analytical result can be derived for the average force on an atom traveling through low-intensity light in the lin \perp lin configuration. It is valid when $\|\vec{v}\| \ll \gamma/k$ and is expressed as [18]

$$\vec{f} = \frac{-\alpha\vec{v}}{1 + \left(\frac{\vec{v}}{\vec{v}_c}\right)^2}, \quad (2.6)$$

where $\alpha = -3\hbar k^2 \delta / \gamma$ for $\delta < 0$ and $\|\vec{v}_c\| = 1/(2k\tau_p)$ is the critical speed, where τ_p is the average time required for an atom to be transferred from one ground state magnetic sublevel to the other ground state magnetic sublevel via photon absorption and emission (a process known as optical pumping [18]; $1/\tau_p = (I/I_{sat})(\gamma^3/(4\delta^2))$ [17]). The velocity domain over which (2.6) is linear corresponds to the velocity capture range for lin-perp-lin cooling. Sufficiently slow moving atoms that are within the velocity capture range experience an additional damping force that is much more effective than Doppler cooling, as shown in figure 2.3.

In the range where the force is linear, the minimum (lowest achievable) equilibrium temperature when $|\delta| \gg \gamma$ is expressed as $T \simeq \hbar\gamma^2(I/I_{sat})/(16k_B|\delta|)$. The temperature expression suggests that an unphysical limit approaching zero temperature is possible. A more meaningful lower temperature limit from this cooling mechanism requires that the RMS speed be much smaller than $\|\vec{v}_c\|$, leading to a condition for the minimum laser intensity necessary for the temperature derivation validity [18]. The condition can be expressed as $I/I_{sat} \gg 2\hbar k^2 |\delta|^3 / (M\gamma^4)$, where M is the atomic mass of the particular species being laser cooled. A subsequent condition is then placed

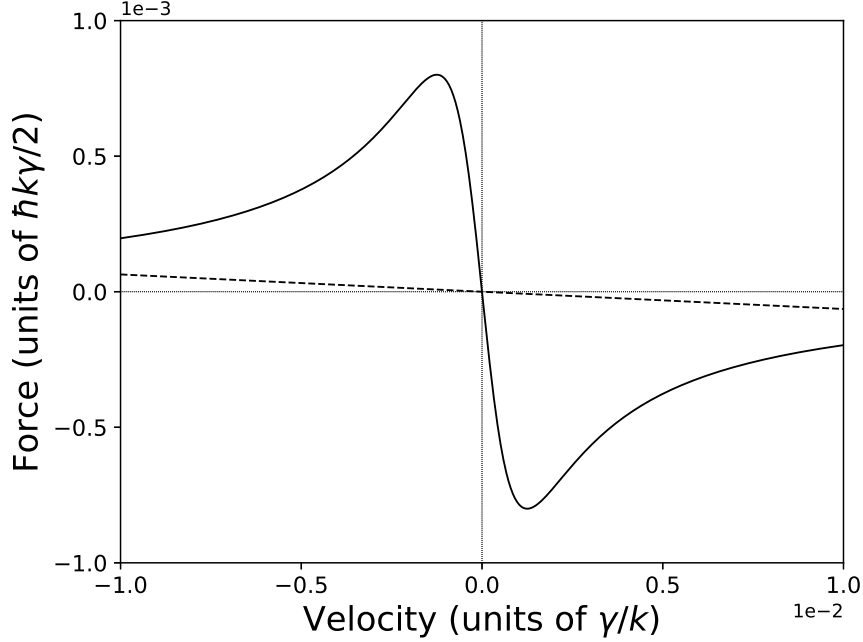


Figure 2.3: The average force on an atom irradiated by a red-detuned one-dimensional optical molasses in the lin \perp lin configuration, where $I/I_{sat} = .01$ and $\delta = -\gamma$. The solid curve corresponds to the average force from lin-perp-lin cooling and the dashed curve corresponds to the average force from pure Doppler cooling.

on the minimum equilibrium temperature and is expressed as $T \gg \hbar^2 k^2 |\delta|^2 / (k_B M \gamma^2)$. Achieving the lowest predicted temperatures requires an atom gas with very low optical density such that multiple photon scattering events do not contribute substantial heating [41–43].

2.2.2 Motion-Induced Orientation Cooling

Motion-induced orientation cooling is created by overlapping counter-propagating laser beams of the same frequency, ω , such that one beam is σ^+ circularly polarized ($\hat{\epsilon}_1 = -(\hat{x} + i\hat{y})/\sqrt{2}$) and the other beam is σ^- circularly polarized ($\hat{\epsilon}_2 = (\hat{x} - i\hat{y})/\sqrt{2}$) with regard to the atom's absorption frame. This is known as the σ^+ - σ^- configuration [18]. Assuming plane wave solutions of equal amplitude counter-propagating along the \hat{z} -direction leads to a total electric field expressed as

$$\vec{E} = -\sqrt{2}E_0 \sin \omega t [\hat{x} \sin kz + \hat{y} \cos kz], \quad (2.7)$$

which is an electric field that is linearly polarized with a polarization vector that rotates around the axis of propagation (in the lab frame) with a periodicity determined by the wavelength of the laser beams. An atom moving through this polarization landscape encounters light of constant intensity and linear polarization everywhere. The light shifts no longer vary spatially, but instead are constant along the direction of motion for a particular magnetic sublevel.

A $J = 1$ to $J = 2$ transition can be used to explain how the σ^+ - σ^- configuration can result in sub-Doppler temperatures [18]. In this case, the $J = 1$ ground state has magnetic sublevels, $m_J = 0, \pm 1$. Transforming to a moving frame (rest frame of the atom) that rotates with the direction of the linear polarization leads to nonadiabatic (vanish when the atom is at rest) couplings proportional to $\vec{k} \cdot \vec{v}$ between the ground state eigenstates. This leads to a population difference that causes the atom to experience unbalanced radiation pressure forces from the counter-propagating beams. Due to the structure of the CG coefficients, the atom scatters more photons from the beam it is moving toward as compared to the beam it is moving away from with a velocity dependence that becomes effective at speeds where Doppler shifts are small. Velocity reduction still occurs through differential absorption from counter-propagating laser beams, but rather than reliance on the Doppler shift, motion-induced orientation cooling depends on non-adiabatic following of the atom orientation as it moves through the polarization landscape (here orientation refers to the anisotropy in the populations of the ground state magnetic sublevels). This non-adiabatic following of the atom orientation is what leads to this cooling mechanism being referred to as motion-induced orientation cooling.

In a low-intensity ($\tau \ll \tau_p$) and low velocity ($\|\vec{v}\| \ll 1/(k\tau_p)$) regime, the velocity dependent force for a $J = 1$ to $J = 2$ transition in the σ^+ - σ^- laser configuration can be expressed as [18]

$$\vec{f} = - \left(\frac{120}{17} \frac{-\delta\gamma}{5\gamma^2 + 4\delta^2} \hbar k^2 \right) \vec{v}, \quad (\delta < 0). \quad (2.8)$$

The velocity capture range for motion-induced orientation cooling corresponds to the velocity domain where (2.8) is valid. Low-intensity is an initial assumption for the expression's derivation, so the velocity capture range is necessarily small. Even so, for slow atoms within the capture

range, the resulting damping force provides a much more effective cooling mechanism than the force exerted by Doppler cooling. A comparison of the two forces in the linear regime is shown in figure 2.4.

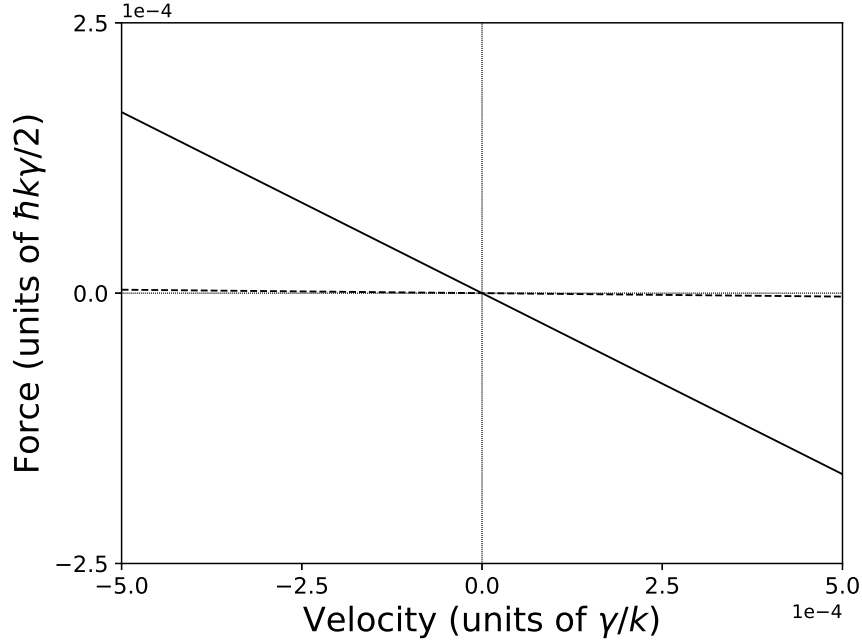


Figure 2.4: The average force on an atom irradiated by a red-detuned one-dimensional optical molasses in the $\sigma^+ - \sigma^-$ configuration, where $I/I_{sat} = .01$ and $\delta = -\gamma$. The solid curve corresponds to the average force from motion-induced orientation cooling and the dashed curve corresponds to the average force from pure Doppler cooling.

For the motion-induced orientation cooling mechanism, the minimum equilibrium temperature when $|\delta| \gg \gamma$ is given by, $T \simeq 29\hbar\gamma^2(I/I_{sat})/(600k_B|\delta|)$. As was the case in lin-perp-lin cooling, the lowest achievable temperature from motion-induced orientation cooling must also be carefully considered. A condition for the minimum laser intensity can be expressed as $I/I_{sat} \gg 2\hbar k^2|\delta|/(M\gamma^2)$, and the resulting condition for the minimum temperature is then expressed as, $T \gg \hbar^2 k^2/(k_B M)$. This indicates that temperatures larger than the recoil temperature (corresponding to the recoil velocity), but less than the Doppler cooling limit, are achievable in a low-intensity $\sigma^+ - \sigma^-$ laser configuration. In addition, for substantial detunings, motion-induced orientation cooling results in lower temperatures than lin-perp-lin cooling.

2.3 Magneto-Optical Trap

The laser cooling mechanisms described in section 2.1 and 2.2 provide viscous forces that can be used to slow atoms, but they do not provide a restoring force necessary for confining atoms within a region of space. An atom in motion that leaves the volume of overlap formed by the counter-propagating laser beams is essentially lost, since it is no longer acted on by the slowing forces present in the optical molasses. However, a spatially dependent force that acts to "localize" the atom can be introduced through a weak inhomogeneous magnetic field along the direction of light propagation [21–23]. Such a magnetic field combined with the σ^+ - σ^- laser configuration is known as a magneto-optical trap (MOT) [24]. For simplicity, the MOT will be described in a one-dimensional case.

The MOT scheme can be applied using any J_g to $J_e = J_g + 1$ transition, so a $J = 0$ to $J = 1$ transition is adequate for understanding the effect of adding a weak magnetic field, $\vec{B}(z) = bz\hat{z}$, where b is the field gradient. The excited state magnetic sublevels, $m_J = 0, \pm 1$, are Zeeman shifted by an amount, $\Delta E = g_J m_J \mu_B bz$, where E represents energy, g_J is the Landé g -factor, and μ_B is the Bohr magneton. For an atom located at a position, $z < 0$, the $m_J = +1$ sublevel is shifted lower in energy. Conversely, if the atom is located at a position, $z > 0$, then the $m_J = -1$ sublevel is shifted lower in energy. Arranging the counter-propagating lasers to be red-detuned and aligned such that the σ^+ beam propagates in the $+\hat{z}$ -direction results in an atom located at $z < 0$ scattering more σ^+ light than σ^- light on average. This is due to the frequency difference associated with the $\Delta m_J = +1$ transition being closest to the laser frequency. The situation is the opposite for an atom located at $z > 0$, where it will scatter more σ^- light than σ^+ light due to the $\Delta m_J = -1$ transition being closest to the laser frequency. The effect of this spatially dependent differential scattering from the laser beams is to drive the atom toward the magnetic field zero ($z = 0$). A depiction of the energy levels and counter-propagating beams are shown in figure 2.5.

For a sufficiently slow moving atom ($\|\vec{v}\| \leq \gamma/k$) near $z = 0$, the viscous force from the radiation and the restoring force from the magnetic field gradient leads to damped harmonic motion [24], and the atom becomes spatially confined. As the Doppler cooling limit is reached, sub-

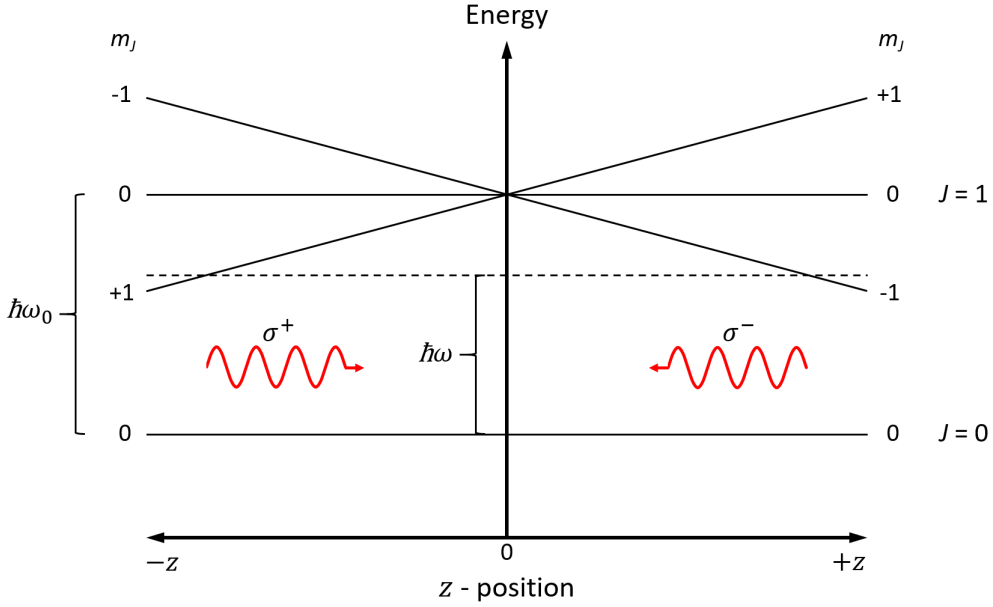


Figure 2.5: Energy levels for a $J = 0$ to $J = 1$ transition in the presence of a weak inhomogeneous linear magnetic field, $\vec{B}(z) = bz\hat{z}$. The energy levels are Zeeman shifted by an amount, $\Delta E \propto m_J z$, where the atomic resonance frequency is ω_0 and the laser frequency is ω . An atom located at $z < 0$ ($z > 0$) will scatter more σ^+ (σ^-) light on average. The position dependence of the magnetic sublevel energy shifts combined with properly polarized light leads to the radiation pressure force driving the atom toward $z = 0$.

Doppler cooling begins to dominate [44–46] and the atom is cooled highly effectively since it is trapped in the region of laser overlap where the magnetic field is low. From the one-dimensional description, it would appear that motion-induced orientation cooling is the relevant sub-Doppler cooling mechanism in a MOT. However, the polarization gradient formed in the volume of a multi-dimensional MOT is a complicated superposition of fields that leads to both σ^+ - σ^- and $\text{lin} \perp \text{lin}$ polarization landscapes. An atom in motion along a trajectory that does not coincide with a laser beam propagation axis will likely encounter both types of polarization gradients.

One way to straightforwardly implement a MOT in three-dimensions is to combine the three-dimensional red-detuned optical molasses described in section 2.1 with a pair of equal radius magnetic coils. The coils are positioned coaxially with opposite current directions to produce a spherical quadrupole magnetic field [22, 47, 48]. The magnetic field is zero at the position half way between the coils (along the axis of symmetry) and increases linearly in all directions outward from that position. The counter-propagating laser beam pairs for the optical molasses are arranged in

the σ^+ - σ^- configuration and are made to intersect at the magnetic field zero. Assuming properly polarized beams with respect to the field directions along the orthogonal axes, the damping forces from the optical molasses and the spatial restoring force from the magnetic field are present in all three dimensions. The temperature of atoms in a low density MOT, where atom-atom interactions such as multiple photon scattering and collisions can be neglected, is identical to the temperature of an optical molasses [41,49]. However, the typical parameters (i.e. laser intensity, frequency detuning, atomic species, spatial number density) used in a standard Rb MOT implementation yield gas temperatures on the order of $100 \mu\text{K}$ with a root-mean-square spatial extent $\sim 1 \text{ mm}$ in one dimension.

2.4 Optical Dipole Trap

Magneto-optical traps are a powerful tool for producing low temperature trapped gases, but often times it is preferential to have confined ultracold atoms without extraneous fields (i.e. magnetic fields) present. There are also substantial limitations to the lowest temperatures that can be achieved in a MOT for reasonable density gases [41–43]. In addition, it may be desirable to have higher spatial number densities than what can be achieved in a standard MOT. One option is to use an optical dipole trap produced by a single focused laser beam that is red-detuned far from the atomic resonance of the species being trapped [25,26]. This type of optical dipole trap is known as a far-off resonance trap (FORT) [27]. A FORT does not provide any dissipative forces that can cool atoms, but it does provide a three-dimensional confining potential that leads to an approximately conservative restoring force on the atoms.

A specific type of FORT is created when the trapping laser frequency is less than half of the resonance frequency of the lowest electric dipole transition of the species being trapped. In this case, the optical dipole trap is sometimes referred to as a quasi-electrostatic trap (QUEST) [50,51]. Advantages of using such a trap include a very low photon-scattering rate ($> 10^{-3} \text{ s}^{-1}$ [26]) and small photon recoil energy. From an atom's perspective, the applied laser field, \vec{E} , is well-

approximated as a static electric field. This field induces an atomic dipole moment, $\vec{p} = \alpha_s \vec{E}$, and the resulting dipole interaction potential can be expressed as [26]

$$U_{dip} = -\frac{\alpha_s}{2\epsilon_0 c} I(\vec{r}), \quad (2.9)$$

where α_s is the static polarizability and $I(\vec{r})$ is the spatially dependent intensity of the field. For a Gaussian laser beam, the intensity can be expressed as [52]

$$I(\vec{r}) = I_0 \frac{1}{1 + (z/z_R)^2} \exp\left(-\frac{2r^2}{w_0^2(1 + (z/z_R)^2)}\right), \quad (2.10)$$

where z and r are the axial and radial position coordinates, respectively, I_0 is the peak intensity ($I_0 = 2P_0/(\pi w_0^2)$, where P_0 is the total laser power), $z_R = \pi w_0^2/\Lambda$ is the Rayleigh length, w_0 is the spot size of a Gaussian laser beam, and Λ is the optical trap wavelength. This spatial intensity profile means the interaction potential has a non-vanishing second derivative in all spatial dimensions and so may be approximated as a three-dimensional simple harmonic oscillator potential near the $z = r = 0$ origin. The specific radial to axial aspect ratio of the trap depends on the physical parameters of the Gaussian beam, where aspect ratios of 1:10 - 1:100 are common in experiments. Therefore, a focused Gaussian beam can produce a tightly confining elongated trap, as shown in figure 2.6. The frequency and intensity profile of a red-detuned FORT lead to a conservative force on an atom that is attractive toward the position of highest intensity (i.e. the focus, w_0 , of the laser beam located at the origin), and is expressed as

$$\vec{F}_{dip} = -\nabla U_{dip} = \frac{\alpha_s}{2\epsilon_0 c} \nabla I(\vec{r}). \quad (2.11)$$

For typical laser parameters (spot size on the order 10 - 100 μm and power on the order of 10 - 100 W), the FORT has a trap depth $\sim 100 \mu\text{K}$ (in temperature units, i.e. energy divided by k_B). The depth of the confining potential establishes how much energy an atom can if it is to become trapped. As mentioned above, the optical dipole trap does not provide any dissipative forces, and so the relatively shallow trap depth means laser cooling techniques must be implemented in

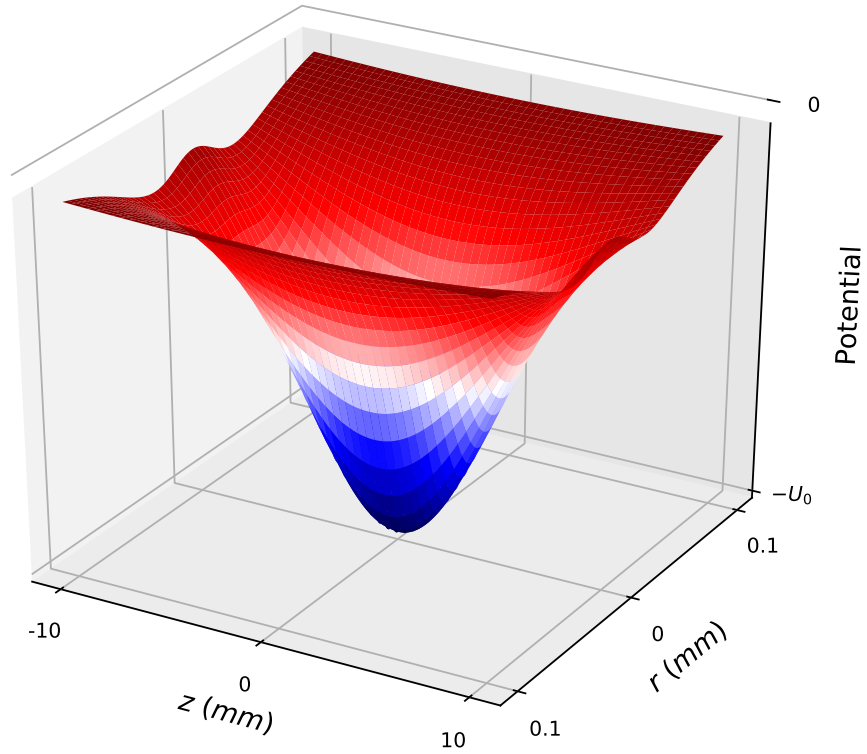


Figure 2.6: Three-dimensional confining potential produced by an optical dipole trap with beam parameters, $w_0 = 100 \mu\text{m}$ and $\Lambda = 10 \mu\text{m}$. A low velocity atom near the origin is trapped in an approximate three-dimensional simple harmonic oscillator potential. Note the axial and radial axes have the same units but span different ranges.

conjunction with the FORT for atoms to be confined. This is usually accomplished by overlapping the FORT with a MOT [27] for a period of time, after which the magnetic coils are turned off, and an optical molasses stage further cools the atoms in the confining potential.

Chapter 3

General Experimental Apparatus

This chapter is intended to provide a synopsis of the main apparatus components used throughout the course of this dissertation work. The apparatus components that are used in a majority of the experiments are a source of neutral atoms, a vacuum chamber, lasers, magnetic field coils, a TTL-based timing control system, and a charge-coupled device (CCD) camera for imaging. These components are combined to create gases of ultracold atoms and characterize those gases by means of absorption imaging. In addition to using a CCD camera for data collection, we also introduced a pair of solid-state photoreceivers as the primary measurement devices for a subset of our later experiments. The main apparatus components will be described to an extent that provides a sufficient context for how the work was performed as described in following chapters. A more detailed description of the first-generation apparatus and characterization techniques, along with electronics circuit diagrams and discussion of the computer control using LabView, can be found in the dissertation of a previous graduate student [28].

3.1 Neutral Atoms for Laser Cooling

Alkali atoms are well suited for laser cooling and trapping experiments as they have single valence electrons with closed optical transitions [26]. The resonance frequencies necessary to excite those transitions generally lie in a spectral range that is conveniently accessible with existing laser technology. Furthermore, alkali atoms have nonzero nuclear spin which leads to hyperfine structure in the ground state and excited states. Finally, these atoms' vapor pressure means that they are easily introduced at the right density into vacuum systems without as much effort as other types of atoms. All of the experiments presented in this dissertation are performed using rubidium atoms, namely ^{85}Rb and ^{87}Rb , and so the following is intended to provide a description of the relevant energy levels used for manipulating those atomic species. The symbol notation for the energy levels will be of the form nL_J , where n is the principal quantum number, L is the total

orbital angular momentum quantum number in spectroscopic notation, and J is the total angular momentum quantum number.

3.1.1 The D2 Line of ^{85}Rb and ^{87}Rb

The ^{85}Rb and ^{87}Rb isotopes (atomic number 37) each have a single valence electron in the $5S_{1/2}$ ground state energy level and the lowest energy excited state is the $5P_J$ energy level, where spin-orbit coupling splits the excited state into $5P_{1/2}$ and $5P_{3/2}$ fine structure energy levels. Our experiments are performed by exciting the valence electron on the $5S_{1/2}$ to $5P_{3/2}$ transition, commonly known as the D2 line, with 780 nm wavelength light. The total angular momentum of the nucleus and electrons is, $F = I + J$, where the nuclear spin (represented as I in this section) for ^{85}Rb is $I = 5/2$ and the nuclear spin for ^{87}Rb is $I = 3/2$. The nucleus and electron interaction results in hyperfine structure in the ground state and excited state energy levels for the two isotopes. The energy difference in frequency units between the fine structure and hyperfine structure energy levels are shown in figure 3.1.

According to quantum number selection rules [53], electric dipole allowed transitions between hyperfine ground state and hyperfine excited state energy levels are those that result in $\Delta F = 0, \pm 1$. The size of the hyperfine splittings with respect to the 6 MHz natural linewidth ($\Gamma = (2\pi\tau)^{-1}$, where $\tau = 26.25$ ns [54]) of the D2 transition allows for manipulating Rb atoms via excitations between various pairs of individual hyperfine energy levels. Of particular importance to laser cooling is the cycling transition used to scatter photons from the laser cooling beams. For ^{85}Rb , the D2 line cycling transition is the $5S_{1/2} F = 3$ to $5P_{3/2} F = 4$ transition, and for ^{87}Rb , the D2 line cycling transition is the $5S_{1/2} F = 2$ to $5P_{3/2} F = 3$ transition. An atom with thermal motion that is illuminated by light that is slightly red-detuned from a cycling transition will repeatedly scatter photons on that transition and experience a velocity reduction for the proper arrangement of laser cooling beams.

During the cycling transition scattering process, the presence of lower energy hyperfine excited states means the atom has a nonzero probability of undergoing a $\Delta F = 0$ or $\Delta F = -1$ ground

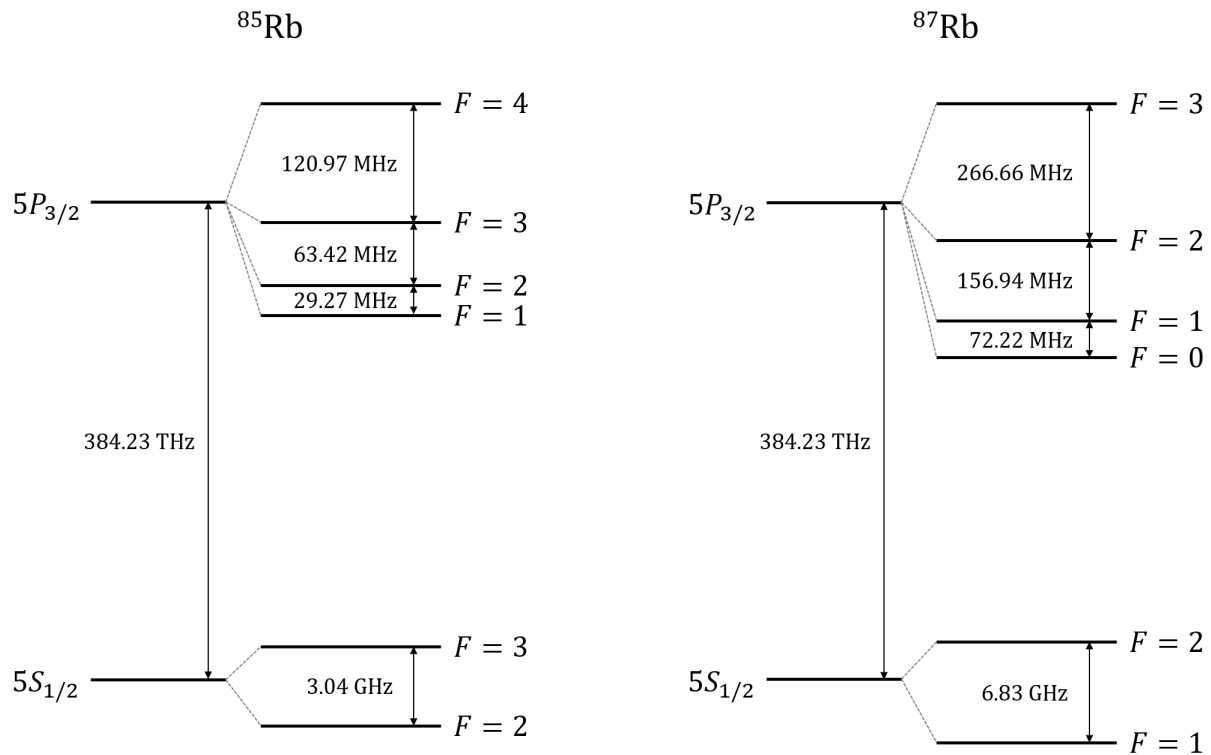


Figure 3.1: The D2 line for ^{85}Rb and ^{87}Rb . The resonant wavelength corresponding to the optical frequency splitting [1, 2] between the $5S_{1/2}$ and $5P_{3/2}$ is 780 nm. Hyperfine structure (ground state [1] and excited state [3] splittings in ^{85}Rb , and ground state [4] and excited state [3] splittings in ^{87}Rb) within each hyperfine manifold are shown to scale (but not with respect to other manifolds or the difference between the $5S_{1/2}$ and $5P_{3/2}$ energy levels). Note the hyperfine splitting in the ground state is orders of magnitude larger than the excited state shifts.

state to excited state transition, followed by a decay into the lower hyperfine ground state. Such an event puts the atom into a "dark state", meaning that atom can no longer be driven by the frequency of the laser cooling light that is nearly resonant with the cycling transition. The inability of the cooling laser frequency to excite atoms in the dark state is a consequence of the relatively large hyperfine splitting between the hyperfine ground states. This problem is remedied by optically pumping atoms from the lower hyperfine ground state back into the upper hyperfine ground state using an additional laser, commonly referred to as a hyperfine repump laser. For our experiments involving ^{85}Rb , the hyperfine repump laser frequency is set to the $5S_{1/2} F = 2$ to $5P_{3/2} F = 3$ transition, and for our experiments involving ^{87}Rb , the hyperfine repump laser frequency is set to the $5S_{1/2} F = 1$ to $5P_{3/2} F = 2$ transition.

3.2 Ultra-High Vacuum Chamber

Performing experiments with ultracold trapped gases of atoms requires operating the experiments in an ultra-high vacuum (UHV) environment. This is due to the trapped atoms being confined in relatively shallow trap depths (~ 1 K for the MOT and ~ 100 μK for the FORT). In the event that a room temperature background molecule or atom collides with a trapped atom, the confined atom will likely be ejected from the trap. To mitigate those losses from background-gas collisions and maximize the characteristic trap lifetimes (i.e. the time required for the number of atoms in a trap to decrease to e^{-1} the initial trapped number), it is important to maintain a high quality vacuum with a pressure $\sim 10^{-9}$ - 10^{-10} Torr.

The ultracold atom experiments presented in this dissertation are all conducted inside of a stainless steel vacuum chamber (Kurt J. Lesker custom chamber) with optical access provided by a subset of the vacuum ports capped with optically transparent windows set in stainless-steel conflat (CF) flanges. The vacuum arm-length (i.e. the extent a port protrudes from the main vacuum chamber body) and port diameter varies depending on the particular arm. All of the vacuum connections are formed by sandwiching a copper gasket between two CF surfaces. The knife-edge on the CF flanges deforms the copper gasket and produces a high-quality seal. This metal-to-metal

connection has the benefit of being able to withstand the high temperatures necessary for "baking-out" the vacuum. A bake-out is required anytime the vacuum chamber has been brought up to atmosphere and exposed to the external environment. At minimum, contaminants from the air, such as water molecules, become attached to the inner walls of the vacuum chamber. In addition, when adding or removing items from the open vacuum chamber (e.g. optics, electrical connections), there is an increased risk of vacuum surface contamination through accidental contact. This can severely inhibit the lowest attainable vacuum pressures since impurities in the vacuum system will outgas over time (creating a persistent background pressure). The bake-out process accelerates this outgassing by raising the temperature of the entire sealed vacuum system to 150 °C - 300 °C, where the maximum temperature is limited by whichever component in the system has the lowest bake-out temperature rating.

3.2.1 Bake-Out Procedure

The procedure for taking the closed vacuum chamber from atmosphere to UHV pressures can be summarized by the following steps. First, the vacuum chamber is slightly elevated from the main optical table to eliminate direct surface contact during the bake-out. Next, a dedicated vacuum chamber port with a bakeable all-metal isolation valve (Nor-Cal Products Model AMV-150-CF) is attached to a bootstrapping pump (comprised of a turbo vacuum pump (Pfeiffer Vacuum Model TMU 261 P) and diaphragm vacuum pump (Pfeiffer Vacuum Model MVP-035-2) in series). The chamber is wrapped with independent lengths of heater tape connected to variac power supplies, and thermistors are strategically placed to monitor the local temperature at different positions. The entire vacuum chamber is then wrapped with aluminum foil to create an enclosed oven, and the heater tape is used to slowly raise the temperature of the system. During this time, it is important to ensure large temperature gradients do not develop, since these can lead to differential thermal expansion at flange connections that could result in vacuum leaks. While the temperature is being increased, the diaphragm vacuum pump is used to compensate for the outgassing and ultimately bring the vacuum pressure down to levels where the turbo vacuum pump can operate effectively

($\sim 10^{-3}$ Torr). The system is given time to bake until the pressure reduction approximately levels off ($\sim 10^{-8}$ Torr), at which point the applied heat is slowly reduced to zero and the tin foil is removed. The chamber is carefully lowered to its original height and an ion vacuum pump (Gamma Vacuum Model 45S-CV-2V-SC-N-N) that is attached to another dedicated vacuum port is turned on. Finally, the bakeable valve is closed and the bootstrapping pump is turned off and detached from the vacuum chamber. The UHV operates indefinitely with the ion vacuum pump maintaining the vacuum pressure.

3.3 External-Cavity Diode Lasers

The coherent light required for creating ultracold gases of atoms in our experiments is produced by tunable external-cavity diode lasers (ECDLs), otherwise known as grating-stabilized diode lasers, that are aligned and controlled to emit 780 nm wavelength light. These are home-built systems that use the rear facet of a commercial diode laser (Roithner Lasertechnik Model ADL78901TX) and a diffraction grating in the Littrow configuration to form a resonant cavity [55, 56]. The cavity is placed in an enclosure to isolate it from environmental changes (e.g. turbulent air, temperature gradients), and temperature-control of the enclosed cavity is achieved by contact with a thermoelectric device mounted to a heat sink to the outside environment. A general schematic of the design of a homebuilt laser is shown in figure 3.2.

The wavelength of the laser emission is determined by the cavity mode that experiences the most gain [52]. As shown in figure 3.2, the diffraction grating is mounted such that the first diffraction order couples directly back into the diode laser, and the zeroth order reflects out of the cavity and enclosure. The first diffraction order provides feedback into the lasing medium and increases the gain associated with a particular cavity mode, causing the emission to be predominantly in that single mode [52]. By altering the angle between the incident light and the grating surface normal, the wavelength associated with the mode with maximum gain can be selected [56] (over a finite range determined by the diode laser and cavity characteristics). The diffraction grating is physically mounted (glued) to a mirror mount, which provides coarse adjustment capability to the angle

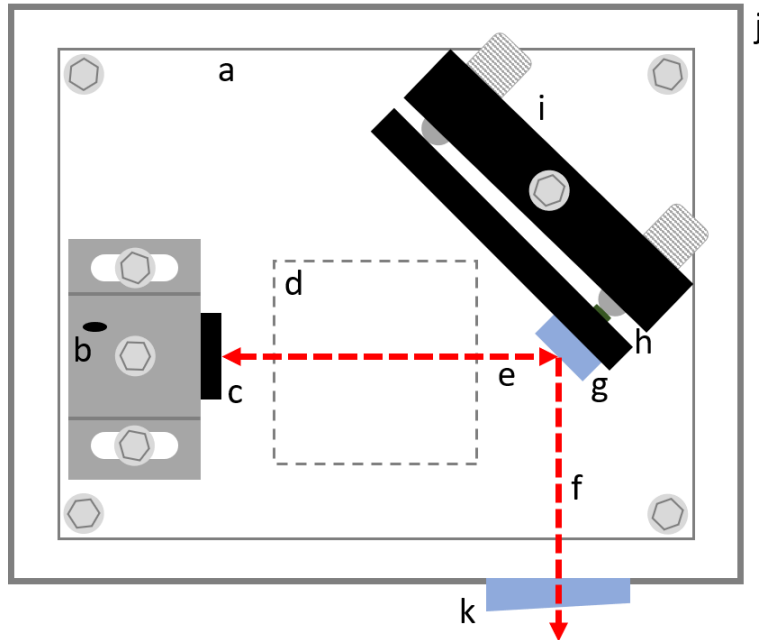


Figure 3.2: Top-down view of the main elements housed inside the enclosure of a homebuilt ECDL. The labeled parts are as follows: a) an aluminum mounting plate, b) a thermistor mounted to the top of an aluminum diode laser collimation tube housing, c) a diode laser collimation tube, including diode laser and collimation optic, d) a thermoelectric device mounted beneath the aluminum mounting plate, e) the beam path of the diode laser output (rightward arrow) and the first diffraction order coupled back into the diode laser (leftward arrow), f) the zeroth diffraction order (experiment laser beam), g) a diffraction grating, h) a piezoelectric actuator mounted between a surface and adjustment screw head, i) a mechanical mirror mount with vertical and horizontal adjustment screws, j) aluminum enclosure, and k) experiment laser beam output window (wedge). The electrical connections associated with the diode laser, thermistor, thermoelectric device, and piezoelectric actuator are left out for clarity.

of the grating. Fine-scale angle changes are accomplished by applying a bias voltage (Thorlabs Model MDT694A) to a piezoelectric actuator (made from lead zirconate titanate and referred to as PZT (Thorlabs Model AE0203D04F)) mounted between the mirror mount surface and horizontal adjustment screw (see figure 3.2).

Thermal expansion or contraction of the cavity directly affects the wavelength of the dominant lasing mode, so an additional source of wavelength control comes from altering the temperature of the cavity. Additionally, the center of the gain curve of the diode laser itself is temperature-dependent. The easiest way to alter the temperature is by changing the current supplied to the thermoelectric device, or to alter the injection current supplied to the diode laser. The temperature sensitivity of the laser wavelength does, however, mean temperature control of the cavity is critical when performing experiments. Including a thermistor in the homebuilt enclosure provides a voltage signal that is used for an electronic servo-loop [28] that controls the current supplied to the thermoelectric cooler. A low-noise current supply (ILX Lightwave Model LDX-3525) is used to power the diode laser. Long-timescale temperature changes are readily managed by the feedback loop, but rapid temperature variations can be severely problematic. Rapid temperature changes can be compensated for using an additional feedback servo-loop that alters the injection current, but this was not necessary in our experiments, and so was not implemented.

In addition to the electronic servo-loop that controls the temperature of the cavity, there is a servo-loop [28] that controls the bias voltage applied to the PZT. When a constant voltage is applied to the PZT, the resulting cavity length produces a specific output frequency of the laser. Changing the PZT voltage then allows for the laser frequency to be altered in a controllable way. For this to be useful during our experiments, it is necessary to provide a precise frequency reference that can be used to calibrate the applied voltages such that the laser operates at the desired frequency. The voltage signal for the servo-loop is provided by a dichroic-atomic-vapor laser lock (DAVLL) [5] signal. The frequency reference used to calibrate the DAVLL signal is provided by a Doppler-free saturated absorption (SA) spectroscopy set-up [55]. The light used to create the DAVLL signal and SA signal is derived from the ECDL. Figure 3.3 shows a DAVLL set-up and SA set-up, along

with the resulting signals. Calibrating the DAVLL signal based on the hyperfine splitting in Rb allows us to apply a specific voltage to the PZT so that the output laser frequency corresponds to a well-known frequency that drives a transition in Rb atoms.

As shown in figure 3.3, a DAVLL set-up works by sending linearly polarized light through a room temperature Rb vapor cell. The linearly polarized light can be considered as being composed of equal parts σ^+ and σ^- circular polarization components. A uniform magnetic field, \vec{B} , is provided by permanent magnet rings attached concentrically around the vapor cell. The effect of the magnetic field (~ 100 Gauss) is to Zeeman shift the central frequencies of the Doppler broadened absorption features associated with the σ^+ and σ^- circular polarization components. The central frequencies are shifted by equal and opposite amounts away from the unshifted resonance frequency. After the vapor cell, the light passes through a quarter waveplate and polarizing beam splitter (PBS) cube. The fast axis of the quarter waveplate is orientated to be 45° with respect to the incident light polarization direction (and PBS through-beam output axis) so the σ^+ and σ^- circular polarization components are split into separate paths after the PBS. The transmitted intensity of each component is detected and the signals are combined to form a difference signal. The laser is scanned over a range of frequencies and the net result is a broad antisymmetric signal with an approximately linear slope ideal for stable side-locking.

3.3.1 Laser Beam Manipulation Tools

Having a coherent light source tuned to a desired frequency is critical for our experiments, but it is not the only requirement. During the course of an experiment, it is often necessary to change the frequency of a laser beam. The servo-loop electronics allow for digitally switching between preset set-points corresponding to different voltages (i.e. frequencies) on the linear slope of a DAVLL signal (see figure 3.3(c)). This provides the capability of jumping the laser frequency to different values within a hyperfine manifold (see figure 3.1) during the course of an experiment. Further frequency control comes from acousto-optic modulators (AOMs) that produce deflected beams with a known frequency shift. We commonly use 40 MHz (IntraAction Corp. Model AOM-

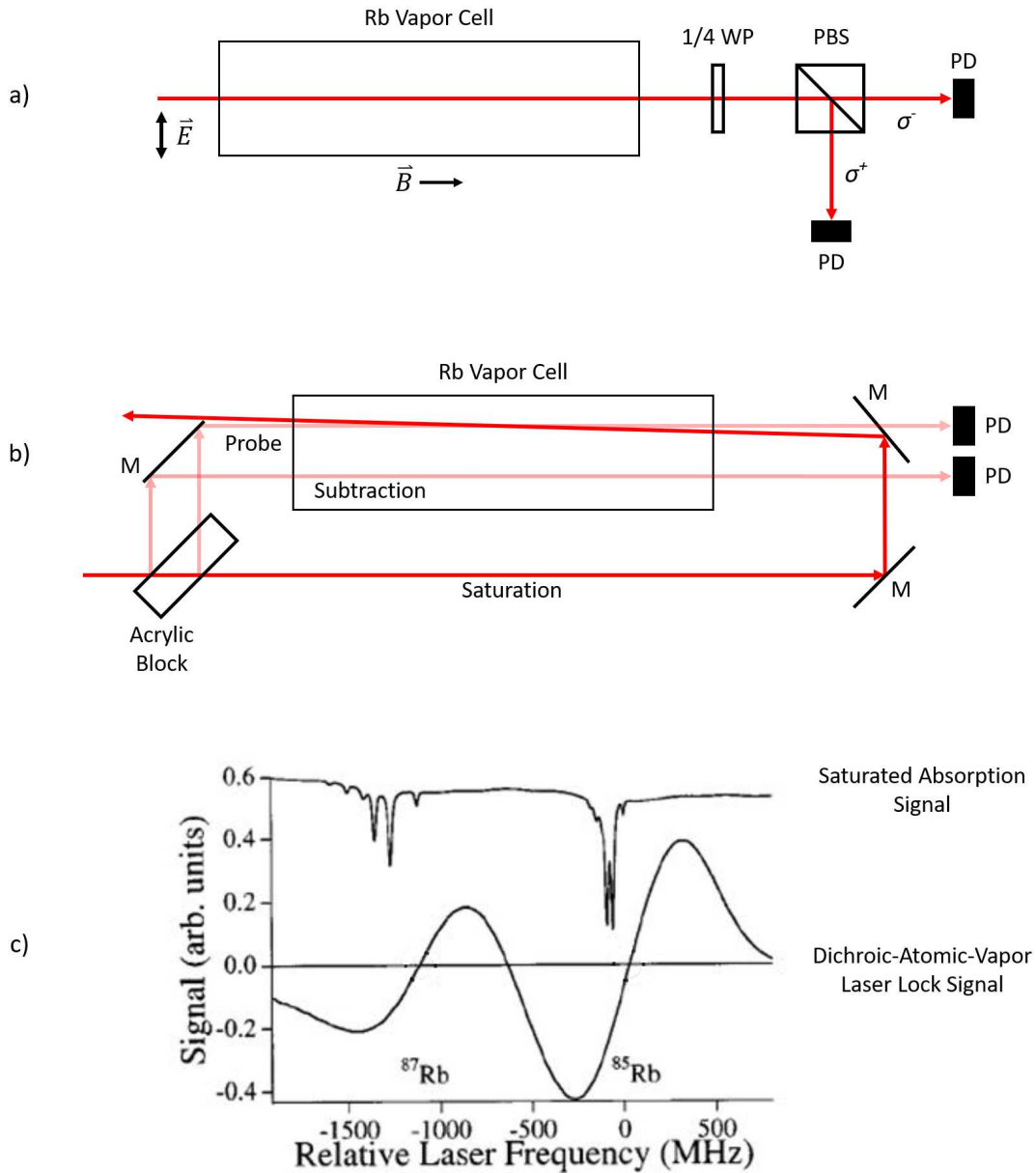


Figure 3.3: Schematic of laser beam and vapor cell arrangements used for creating signals to calibrate and lock the diode laser frequency. Part a) shows the dichroic-atomic-vapor laser lock set-up, and part b) shows the Doppler-free saturated absorption spectroscopy set-up. Part c) is adapted with permission from [5] © The Optical Society and shows the resulting signal shape produced by each type of set-up when the laser frequency is scanned over the ^{87}Rb $F = 2 \rightarrow F' = 1, 2, 3$ and ^{85}Rb $F = 3 \rightarrow F' = 2, 3, 4$ transitions. The labels indicate photodiodes (PD), a waveplate (WP), a polarizing beam splitter (PBS) cube, and mirrors (M). In both set-ups, the PD signals are combined such that one PD is forward-biased and the other is reverse-biased to form a difference signal.

402AF3) and 80 MHz (Isomet Model 1205C-2) AOMs driven by homebuilt RF signal generators comprised of voltage-controlled oscillators (VCO) in series with RF switches, attenuators, and amplifiers (Mini-Circuits components). The combination of set-point jumps and AOM frequency shifts gives us a wide range of frequency control during an experiment.

In addition to changing the laser frequency, we require the ability to alter the intensity of laser beams during an experiment. AOMs provide a means of doing so by varying the amplitude of the RF drive signal. This is accomplished via RF switches that lead to different levels of RF attenuation in the homebuilt driver circuits. Alternatively, a programmable function generator can be used in series with a power amplifier to vary the intensity of the RF signal sent to an AOM. Laser beam intensity control means that AOMs also serve as effective shutters, where a deflected beam path can typically be extinguished by more than a part in 10^3 . We generally use an AOM "backed-up" by a mechanical shutter (Uniblitz Model LS6) to ensure any undesirable leakage light along a beam path is blocked.

The general experimental layout on the optical table includes many optical components that are used to reshape, resize, or redirect laser beams. Reshaping and resizing is accomplished by anamorphic prism pairs and lens combinations, respectively. Redirecting laser beams is accomplished by mirrors and beamsplitter cubes. Additionally, some of our experimental layout requires two laser beams to propagate along the same path. This is achieved by rotating (using a half waveplate) the linear polarization of the two beams to be in orthogonal directions, and then directing them along orthogonal paths into a polarizing beam splitter cube. One beam passes directly through the cube and the other beam reflects at the inner surface so that both beams exit the cube along the same path. Beamsplitter cubes (or wedges) are also used to provide "pick-off" laser beams. Pick-offs serve a variety of purposes such as providing light for frequency references and lock signals (i.e. SA and DAVLL set-ups), temporary beam paths used for auxiliary measurements, or new beam paths that are essential to an experimental scheme.

3.4 Experiment Magneto-Optical Trap

Whether being the primary trap for an experiment or providing an ultracold gas to be loaded into an optical trap, the MOT is an integral component of our experiments when it comes to producing samples of ultracold atoms. Our MOT consists of three circularly polarized laser beams that are directed through the vacuum chamber along mutually orthogonal directions and retroreflected back along the same paths to produce three pairs of counter-propagating beams intersecting at the center of the vacuum chamber. Opposing magnetic coils are mounted externally on the vacuum chamber and positioned to provide a magnetic field zero at the beam intersection. In addition to the trap lasers that create the optical molasses there is a repump laser beam. The role of the repump laser is to maintain continuous laser cooling by preventing atoms from getting stuck in a dark state.

Our apparatus uses two ECDL lasers to implement the laser cooling in our experiments. These consist of the trap laser and the repump laser. The trap laser provides the three pairs of counter-propagating laser beams for the optical molasses. The frequency is tuned to drive transitions starting from the upper hyperfine ground state (see figure 3.1). All three beam pairs are derived from a single ECDL through appropriate placement of beam-splitter cubes along the beam paths. Each beam is linearly polarized until passing through a quarter waveplate just before entering the vacuum chamber. The beams pass through the center of the chamber and exit through a port window opposite to the input side. A quarter waveplate and mirror are positioned just after the output window so the beams retroreflect back through the vacuum chamber to form circularly polarized counter-propagating laser beams in the σ^+ - σ^- configuration. The repump laser is a separate ECDL with the frequency tuned to drive transitions starting from the lower hyperfine ground state. A single beam from the repump laser is overlapped with one of the σ^+ - σ^- beam pair paths through the vacuum chamber, and its role is to optically pump atoms from the lower hyperfine ground state back into the upper hyperfine ground state so the trap laser can continue to laser cool the atoms.

With the counter-propagating laser beam pairs arranged to intersect orthogonally at the center of the vacuum chamber, the remaining piece needed for the MOT is the inhomogenous magnetic field with a magnetic field zero at the laser intersection. Our experimental apparatus has two

opposing magnetic coils that are attached externally on opposite sides of the vacuum chamber. Each coil is mounted concentrically on a vacuum arm that coincides with one of the laser beam pair propagation axes. The spherical quadrupole magnetic field is produced by applying current to the coils, and the resulting magnetic field induces the Zeeman splitting necessary to introduce a spatially dependent force on the atoms in the laser cooling region. A schematic depicting the arrangement of our MOT is shown in figure 3.4.

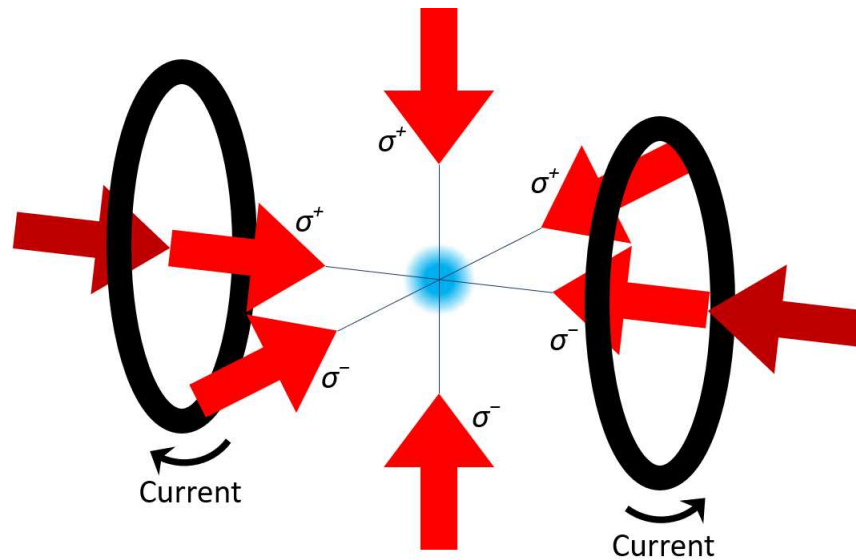


Figure 3.4: Schematic of the three-dimensional MOT configuration implemented experimentally. The light-red arrows correspond to red-detuned laser beams for laser cooling, where the circular polarization of each beam is labeled. The counter-propagating laser beam pairs are mutually orthogonal and intersect at the center of the vacuum chamber. The dark-red arrows correspond to the repump laser. The black circles represent opposing magnetic coils mounted external to the vacuum (see main text), and the light-blue circle in the center represents a laser cooled and spatially confined gas of atoms.

3.4.1 Loading Atoms into the MOT

For our experiments, the method of introducing Rb atoms into the vacuum chamber is to heat a Rb getter (SAES Getters Rb/NF/3.4/12 FT10+10), also referred to as an alkali metal dispenser (AMD). The getter is a device comprised of a reducing agent and rubidium chromate mixture housed in a small metal container. The container has electrical terminals on both ends and a small slit to allow the alkali metal to escape. When the device is heated (by supplying current),

a reduction reaction occurs and the alkali metal evaporates out of the container. This provides a source of Rb atoms that thermalize to a Maxwell-Boltzmann velocity distribution inside of the vacuum chamber. As discussed in section 2.3, there is a finite velocity capture range over which atoms can be effectively Doppler cooled and then confined in the MOT. The Rb vapor introduced into the vacuum contains a subset of atoms with suitably low velocities, and it is these atoms that are laser cooled and trapped for our experiments. Of course, there are also atoms with velocities that are too high to be cooled and trapped for our experiments. Those atoms, along with impurities that may still be present from opening the chamber or those introduced by outgassing, are what constitute the primary source of room temperature atoms and molecules that limit the trap lifetimes through background-gas collisions [26].

3.5 Experiment Optical Dipole Trap

A subset of our experiments require a sample of ultracold atoms spatially confined in the vacuum chamber, but without near-resonant light or magnetic fields doing the trapping. We accomplish this by trapping ultracold atoms in an optical dipole trap. Our particular optical dipole trap is a single focused Gaussian laser beam produced by a high-power RF excited CO₂ laser (Coherent Model GEM Select 100). The laser output wavelength is 10.6 μm , which is far red-detuned from the 780 nm resonance wavelength of the D2 line transition in Rb. Therefore, our optical dipole trap operates as a FORT, as described in section 2.4. The confining potential is derived from the main CO₂ laser output using a 40 MHz AOM (IntraAction Model AGM-406B1) driven by a commercial RF driver (IntraAction Model GE-4030).

The peak laser intensity of the FORT is the beam property that determines the depth of the trapping potential and the spatial oscillation frequencies associated with the axial and radial directions. The depth of the optical dipole trap establishes the maximum temperature an atom can have while being spatially confined in the trapping potential. When an atom has a large initial kinetic energy compared to the potential depth, it will pass through the FORT light and not be trapped. However, when the kinetic energy of the atom is less than the potential depth, there is an increasing likeli-

hood the atom will become spatially confined in the FORT. Since the optical trap only provides a conservative force, atoms need to be laser cooled into the FORT (i.e. via a simultaneous MOT or optical molasses). Once trapped, the characteristic spatial oscillation frequencies determine the timescale of exchange between potential and kinetic energy as the atom moves in the confining potential.

The radial oscillation frequency is determined by performing a parametric heating measurement [57–59]. This works by heating the trapped atoms through sinusoidal modulation of the laser power [28]. For small modulation amplitudes, the change in characteristic oscillation frequencies follows the change in trap depth. When the trap depth is varied at a frequency close to twice the characteristic oscillation frequency [60], a large amount of energy is put into the gas. We perform trap depth modulation experiments over a range of frequencies (see figure 3.5) and then measure the final temperature (as described in section 3.6.1) after the atoms are heated. The frequency that leads to the largest temperature increase corresponds to twice the radial oscillation frequency. The axial oscillation frequency can be calculated once the gas temperature and axial spatial extent are known (see section 3.6.1). Alternatively, the axial oscillation frequency can be measured by observing the time required for a fraction of atoms at the edge of the trap to move to the center of the trap along the axial direction using absorption imaging techniques (as described in section 3.6).

3.5.1 Aligning and Loading the FORT

Our optical dipole trap is created by focusing the FORT beam to a location external to the vacuum chamber, and then that focus is 1:1 imaged into the center of the vacuum chamber using a lens positioned inside the vacuum. This is a somewhat unusual arrangement compared to other systems used elsewhere, which generally employ a single lens to directly focus to the desired trap location. The FORT wavelength is in the infrared region of the electromagnetic spectrum, so we rely on careful geometric positioning for the initial beam alignment. The challenge is to overlap the roughly mm^3 trapping volume of the laser with the roughly mm^3 volume of trapped atoms at the center of the vacuum chamber, which is about 10 cm away from the outside of the

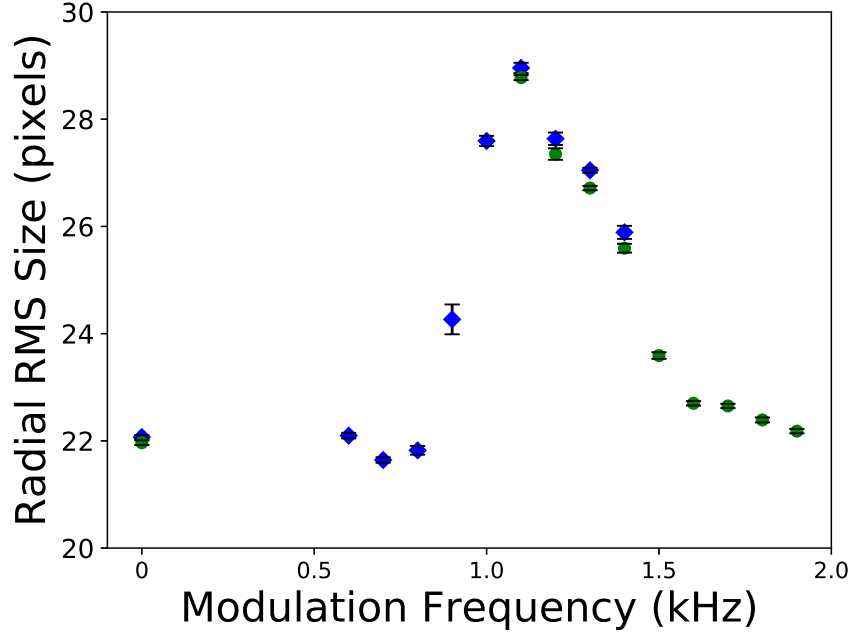


Figure 3.5: Radial oscillation frequency data collected via parametric heating (see main text) over a range of power modulation frequencies. The radial spatial extent is plotted and is related to the temperature of the gas. The largest spatial extent corresponds to the highest temperature gas. The blue diamonds and green circles are data collected on consecutive days. The peak position in this data indicates a radial oscillation frequency of 550 Hz.

vacuum chamber. We start by forming a MOT in the vacuum chamber, which we view using a security camera with sensitivity into the infrared and a video monitor. This allows us to observe the fluorescence of the atoms as they scatter light from the laser cooling beams. An aperture in steel plate is placed directly in front of the FORT beam input window, and a security camera is mounted to a translation stage at the location where the external lens will be positioned. The aperture is adjusted so the MOT appears centered in the aperture hole on the video monitor. Next, the security camera is translated along the direction defined by the input vacuum arm, and if necessary, the aperture position undergoes small corrections to ensure the MOT stays visibly centered. Once the first aperture is positioned, another aperture is placed at the location where the external lens focus will be located. The centering procedure is repeated for the second aperture so that its final position allows the security camera to be translated while keeping the MOT visibly centered between both apertures on the video monitor. Finally, the security camera is removed and the external lens is positioned so the FORT beam passes through the center of the lens. To check the initial beam

alignment, we place Tyvek[®] paper on the output window and send a short pulse from the FORT laser through the chamber. If the beam is able to pass through the apertures and exit the chamber, which is detected when the beam burns a hole in the Tyvek[®] paper, then the rough alignment is complete. Figure 3.6 depicts the aligned FORT laser path through the vacuum chamber.

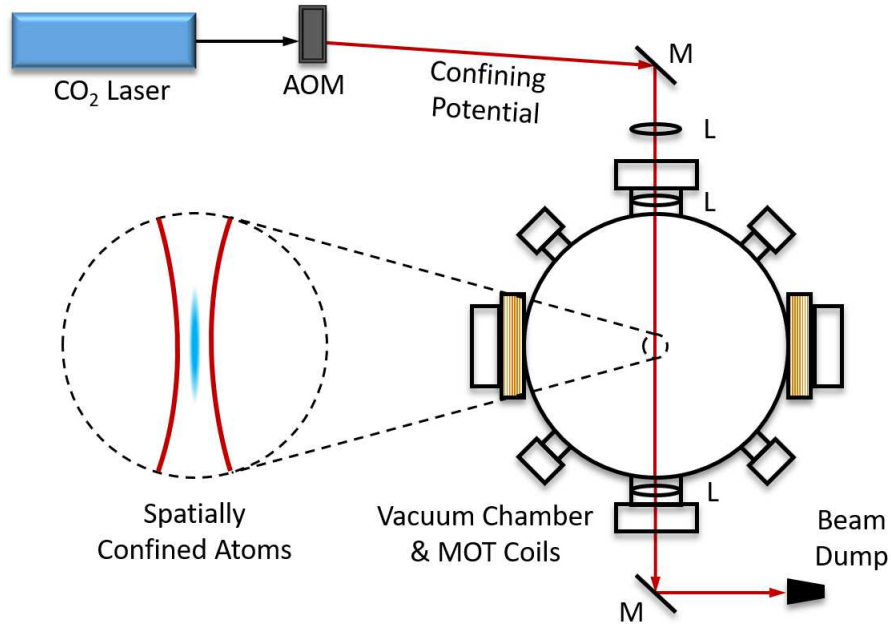


Figure 3.6: Schematic of the FORT beam path through the vacuum chamber. The lens (L) before the chamber creates a beam focus external to the vacuum port. The next lens (internally mounted in the chamber) images the beam focus to the center of the vacuum, where atoms become spatially confined in the optical dipole trap. The third lens in the beam path focuses the beam to a location outside of the chamber so a mirror (M) can direct it into a beam dump. The inset shows an elongated gas of trapped ultracold atoms (light-blue) at the focus of the laser beam (outlined by dark-red curved lines). Distances are not drawn to scale.

The alignment procedure is a reliable method for making contact with the atoms in the MOT, resulting in a detectable number of trapped atoms in the FORT. We detect the trapped atoms by performing absorption imaging (described in the following section 3.6), and the initial signals provide a baseline that we use to optimize the trap load. The adjustable parameters available for optimizing the number of trapped atoms include the optical trap alignment, trap laser alignments, trap laser frequency detuning, repump beam intensity, and shim coil currents. Shim coils are magnetic coils positioned along mutually orthogonal axes around the vacuum chamber and are used

to eliminate stray magnetic fields to produce the lowest possible optical molasses temperatures. They also have the effect of changing the location of the magnetic field zero, and hence the center of the MOT, which can be compensated for by adjustments to the optical trap alignment. Coarse adjustment of the shim coil fields is accomplished by turning off the opposing MOT coils and altering the applied currents so the amount of time that atoms remain in the optical molasses is maximized. We perform this maximization qualitatively by observing the fluorescence of the atoms using security cameras positioned along different axes. The coarse adjustment current values become the starting point for further adjustments during the trap load optimization.

In addition to the above adjustable parameters, there is the computer controlled timing sequence that dictates how long a particular combination of trap laser detuning, repump intensity, and magnetic field environment are applied before and after the optical trap is turned on. The large parameter space available for the trap load optimization makes searching for the global optimum corresponding to the highest number of trapped atoms a futile exercise. Instead, we perform several iterations of each adjustable parameter until we arrive at a sufficiently dense and reproducible number of atoms for our experiments. The long-term stability of the FORT load (with respect to experiment timescales) is more important than operating at the global optimum.

3.6 Imaging Ultracold Gases

Characterization of our ultracold gases is performed using standard absorption imaging techniques. This is the main diagnostic tool that we use to optimize the number of atoms in our traps and to measure the temperature of those atoms. A laser (probe) beam used to image the atoms is derived from the trap laser and overlapped with the ultracold gas in the vacuum chamber. A converging lens placed on the output side of the vacuum chamber collects the transmitted probe light and overlaps it onto a CCD camera (Roper Scientific Model 7404-0001). Proprietary software (WinView) provided by the camera manufacturer converts the CCD data to image files that can be viewed directly, or the files can be manipulated using a variety of software tools (i.e. basic arithmetic operations, binning, scaling, etc.) to produce processed images.

A vast majority of the absorption imaging measurements collected for the experiments described in this dissertation were performed with atoms that were confined in a FORT, and so the following discussion will focus on that particular system (though the general approach also applies to imaging atoms in a MOT). It is useful to identify two categories of images that can be collected: in-trap images and out-of-trap images. As the name suggests, an in-trap image is collected when atoms are confined in the FORT, whereas an out-of-trap image is collected after the atoms have been released from the FORT. Due to the tight radial confinement and high number density in the optical dipole trap, it is usually most useful to perform out-of-trap imaging.

3.6.1 Basic Atomic Gas Characteristics

The most common images we collect are after the trapped atoms have reached thermal equilibrium. To ensure the atoms have sufficiently thermalized, we "hold" the trapped atoms in the FORT for a period of several seconds. We assume a Maxwell-Boltzmann distribution can be used to describe the positions and velocities of the trapped atoms and also approximate the trapping potential as harmonic, which leads to the spatial number density distribution of the cylindrically symmetric gas being expressed as [61]

$$\begin{aligned} \rho(r, z) &= N\omega_r^2\omega_z \left(\frac{m}{2\pi k_B T}\right)^{3/2} \exp\left(-\frac{m}{2k_B T}(\omega_r^2 r^2 + \omega_z^2 z^2)\right) \\ &= \frac{N}{(2\pi)^{3/2}\sigma_r^2\sigma_z} \exp\left(-\frac{1}{2}\left(\frac{r^2}{\sigma_r^2} + \frac{z^2}{\sigma_z^2}\right)\right), \quad \sigma_i = \frac{1}{\omega_i} \sqrt{\frac{k_B T}{m}}, \end{aligned} \quad (3.1)$$

where the subscript, i , corresponds to the spatial dimension (i.e. r, z , where $r^2 = x^2 + y^2$), σ_i is the root-mean-square (RMS) width of the confined atoms' spatial density distribution, ω_i is the characteristic oscillation frequency (rad s⁻¹), N is the number of atoms, T is the temperature of the gas, and m is the atomic mass of the trapped species. The elongated shape of a FORT means

that the radial direction is more tightly confining as compared to the axial direction, so the radial oscillation frequency is larger than the axial frequency by an amount equal to σ_z/σ_r .

Suddenly turning off the FORT leads to the gas undergoing three-dimensional ballistic expansion as a result of the atoms' thermal energy. The equipartition theorem states that the atoms have an average kinetic energy of $k_B T/2$ in each spatial direction with a one-dimensional RMS speed of $v_{\text{rms}} = (k_B T/m)^{1/2}$, so the time dependent spatial extent in each dimension can be expressed as

$$\sigma_i(t) = \sqrt{\sigma_i^2 + v_{\text{rms}}^2 t^2}, \quad (3.2)$$

where t is the amount of time the gas expands (from $t = 0$). Inserting the expression for σ_i into (3.2) leads to

$$\sigma_i(t) = v_{\text{rms}} t \sqrt{1 + \frac{1}{\omega_i^2 t^2}}. \quad (3.3)$$

The trap parameters used for our FORT result in large radial oscillation frequencies (i.e. hundreds of Hertz) and the ballistic expansion time is usually a few milliseconds, so (3.3) for the radial direction can be well-approximated as $\sigma_r(t) \approx v_{\text{rms}} t$. Therefore, the temperature of our ultracold gas can be expressed approximately as

$$T = \frac{m}{k_B} \left(\frac{\sigma_r(t)}{t} \right)^2. \quad (3.4)$$

3.6.2 Probe Beam and Optical Depth

Measuring the spatial extent (and thus the temperature) of our ultracold gas is performed by illuminating the expanded cloud with a low-intensity probe beam set to be resonant with the cycling transition of the particular species being imaged. Before applying the probe beam, the atoms are optically pumped into the upper hyperfine ground state. Once the atoms are in the upper hyperfine ground state, the probe beam is applied. The atoms scatter light out of the probe beam along the direction of light propagation, and a lens positioned on the opposite side of the atoms (and external

to the vacuum chamber) images the resulting shadow onto the CCD camera. The amount of light scattered out of the probe beam is proportional to the number of atoms in the gas, so the shadow imaged onto the CCD has a two-dimensional Gaussian shape. A schematic of the probe beam path is shown in figure 3.7.

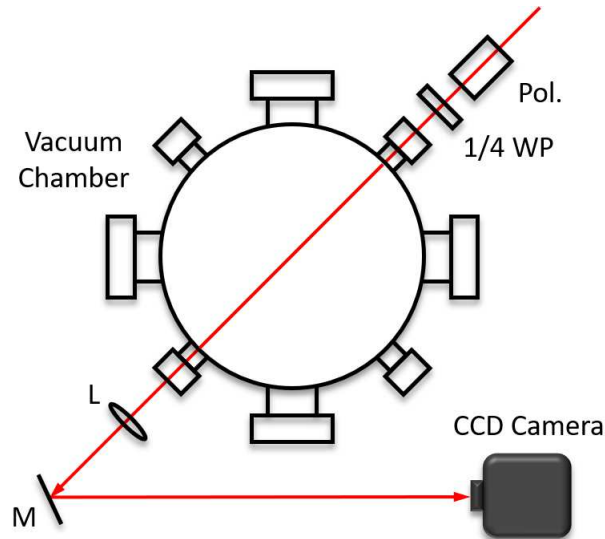


Figure 3.7: Schematic showing the probe beam path through the chamber and overlapped onto the CCD camera. Before entering the chamber, the beam passes through a linear polarizer (Pol.) then a quarter waveplate to create circularly polarized light. A magnification lens (L) on the output side of the vacuum chamber images the light onto a CCD camera. The beam path is directed using a gold-plated mirror (M).

To simplify the image analysis, the probe beam is circularly polarized such that the atoms are spin polarized in the outermost ground state magnetic sublevel via optical pumping. From this energy state, the atoms can only make a closed two-level transition with the corresponding outermost excited state magnetic sublevel. For example, ^{87}Rb atoms illuminated with a σ^+ circularly polarized probe beam will scatter light on the $m_F = +2$ ground state sublevel to $m_F = +3$ excited state sublevel transition. The intensity of the probe beam is attenuated as it propagates (chosen here to be in the \hat{x} -direction) through the gas, which is expressed as

$$\frac{dI}{dx} = -\sigma_0 \rho I, \quad (3.5)$$

where $\sigma_0 = 3\lambda^2/(2\pi)$ is the polarized resonant cross-section, $\rho \equiv \rho(x, y, z)$ is the spatial density distribution (see (3.1)) of the gas, and I is the spatially-dependent light intensity. Integrating (3.5) along the direction of light propagation leads to a simple solution expressed as

$$I(y, z) = I_0 \exp(-\text{O.D.}(y, z)), \quad (3.6)$$

where I_0 is the incident light intensity and $\text{O.D.}(y, z)$ is the optical depth at a position in the two-dimensional plane perpendicular to the probe beam propagation direction. The optical depth can be expressed as

$$\text{O.D.}(y, z) = -\ln\left(\frac{I(y, z)}{I_0}\right) = \sigma_0 \frac{N}{2\pi\sigma_y\sigma_z} \exp\left(-\frac{1}{2}\left(\frac{y^2}{\sigma_y^2} + \frac{z^2}{\sigma_z^2}\right)\right). \quad (3.7)$$

3.6.3 Data from CCD Camera

The role of the CCD camera is to measure the intensity of the transmitted probe light through our vacuum chamber (see figure 3.7). The probe light is collected by a lens and overlapped onto the CCD surface, where each square pixel records a value (i.e. counts) that is proportional to the energy associated with the portion of the beam incident on that pixel area. The net result is a two-dimensional intensity pattern corresponding to the transmitted light. A sequence of four images are collected during each absorption imaging measurement. The first image prepares the CCD by clearing out any dark counts on the pixels. The next image (Im1) is collected when atoms are present in the beam path, which is followed by an image (Im2) of the probe beam when no atoms are present. Lastly, an image (Im3) is collected when no light is directed through the chamber. The final three images are used to calculate an optical depth for each pixel. The two-dimensional optical depth calculated from the images can be represented by

$$\text{O.D.}(x', y') = -\ln\left(\frac{\text{Im1} - \text{Im3}}{\text{Im2} - \text{Im3}}\right), \quad (3.8)$$

where x' and y' are spatial coordinates in the image frames (i.e. represent the location of a pixel). The measured two-dimensional optical depth is fit to (3.7) via least-squares-minimization. The numerical fit parameters are the peak optical depth, radial and axial RMS widths, and center-of-mass position in the image. Since the ultracold gas is elongated in one direction, and since that axis is not necessarily horizontal with respect to a side of the image frame, the fit routine (written in Fortran) also includes an angle of rotation.

The spatial resolution of the imaging system is limited to around $10 \mu\text{m}$ due to the quality of the imaging lens used to collect the probe light. This hinders the ability to resolve the radial spatial extent of a confined gas, since it is near or below the resolution limit (in-trap images do provide information about the axial direction owing to the larger extent in that spatial dimension). Releasing the atoms from the trap allows the gas to expand to a size greater than the resolution limit. During this ballistic expansion, the radial extent quickly reaches a regime where it is determined by the gas temperature, with the initial in-trap size adding only a negligible contribution (see (3.3)). The expanded radial extent thus gives the radial temperature, and the overall absorption gives the total number. In-trap densities are calculated using the temperature and radial oscillation frequency measured by parametric heating (as described in section 3.5). The peak number density, ρ_0 , and the average number density, $\langle\rho\rangle$, are expressed as

$$\rho_0 = \frac{N}{(2\pi)^{3/2}\sigma_r^2\sigma_z}, \quad \langle\rho\rangle = \frac{N}{8\pi^{3/2}\sigma_r^2\sigma_z}. \quad (3.9)$$

The ability to use the images to determine quantities in meaningful units requires calibrating the CCD pixel size with respect to the magnified object size. To perform the pixel calibration, we take advantage of the center-of-mass free fall when the atoms are released from the FORT. We collect images at different times, and then we fit kinematic equations to the center-of-mass motion. Assuming a value for the local gravitational acceleration results in a measurement of the apparent pixel size in the image, including the magnification from the light collection lens. An example of data collected for a pixel calibration is shown in figure 3.8. The data shown in figure 3.8 resulted in

a calibration of $6.6 \pm 0.5 \mu\text{m side}^{-1}$, where "side" corresponds to the one-dimensional side length of a square CCD pixel.

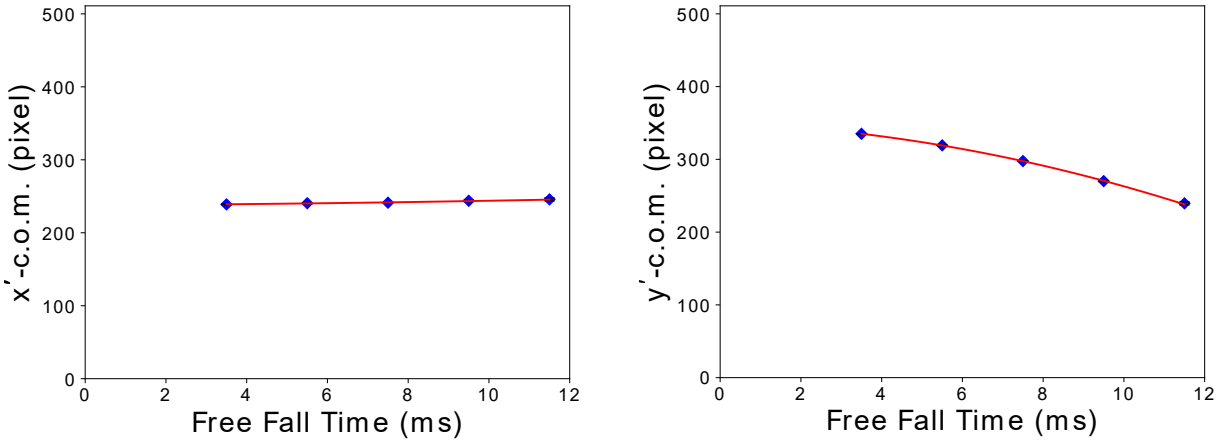


Figure 3.8: Pixel calibration data collected over a range of free fall times. The center-of-mass location of the ultracold gas is determined through absorption imaging performed at specified times after releasing the atoms from the trap. The x' and y' center-of-mass (c.o.m.) positions are plotted separately for clarity. The blue diamonds correspond to data and the red curves correspond to best-fit functions. In both cases, the fit function is a quadratic free fall equation with three fit parameters.

3.7 Measuring Transmission Signals

The experiments that will be presented in chapter 6 use all of the previously described MOT components to produce and characterize an ultracold gas, but the data collection technique used for the main results requires an additional set of apparatus components. In those experiments, the ultracold gas is initially trapped in a MOT, and we measure the intensity of near-resonant light transmitted through the released gas under various experimental conditions. The light is rapidly turned on over a few nanoseconds and we study the time-dependent evolution of the transmitted light over several atomic excited state lifetimes. Rather than using absorption imaging for the data collection, we use a set of fast photoreceivers and preamplifiers to detect the transmission signals. A digital storage oscilloscope is used to save the data.

3.7.1 Laser Beam with Rapid Turn-on

Our method for producing a laser beam with a fast turn-on has been previously implemented both by our group and others. However, given the less common use of an acousto-optic modulator (AOM) as a nanosecond scale turn-on device in ultracold atom experiments, it is worth including a brief summary of the technique we used. A laser beam is derived from the trap laser via a pick-off and tightly focused ($15\ \mu\text{m}$ spot size) into a 200 MHz center frequency AOM (ISOMET Model 1250C). Having a small transverse spatial extent of the beam inside the interaction medium of the AOM minimizes the time required for the generated acoustic wave to propagate across the laser beam. The deflected beam turn-on time is thus determined largely before by the acoustic velocity ($3.63\ \text{mm s}^{-1}$) in the interaction medium and the transverse beam width. We experimentally measured a 10% to 90% 1st order deflection turn-on time of 9 ns, which agrees with simple estimates. The AOM drive frequency comes from a commercial RF driver output (IntraAction Model ME Modulator Driver) that is triggered on by a 5 ns rise-time function generator (Agilent Model 33250A). The function generator output is triggered on by a pulse generator (Berkeley Nucleonics Corporation Model 505), which also provides a delayed trigger for the oscilloscope so that the experiment and data collection are synced in time.

3.7.2 Electronics and Detectors

The detectors we use for measuring short-timescale transmission signals are low noise free space silicon optical receivers (New Focus Model 1601FS-AC). These detectors have 1 GHz bandwidths and 400 ps rise times, and so are well-suited for the measurement. Because of the low laser intensity necessary for the experiment, the resulting signals must be amplified before reaching the oscilloscope. Characterization of test signals was performed to ensure the amplifiers we use do not impart signal distortions with time variations as fast as our measurement timescales. We accomplish signal amplification by using four RF preamplifiers in series (Stanford Research Systems Model SR445A), with each preamplifier having a gain of 5 and a 1 ns rise/fall time. The amplified output signal is directed to a 200 MHz bandwidth digital storage oscilloscope (Tektronix

TDS 2024C). The oscilloscope has universal serial bus (USB) connectivity allowing for direct data transfer to a removable flash drive. Data is collected and saved over a 500 ns time window that includes a detector background signal, the laser turn-on period, and the intensity transmission over several hundred nanoseconds. The resulting signals are used to compare to theoretical predictions of the transmission and to calculate the optical depth associated with the orthogonal light polarization components (as will be described in chapter 6).

Chapter 4

Spatially Truncated Optical Pumping Cooling

The following chapter is dedicated to presenting both the theoretical description and experimental implementation of a laser cooling technique for ultracold atoms trapped in a confining potential. The technique is known as "spatially truncated optical pumping (STOP) cooling" [6], and it uses near-resonant light to preferentially select high energy atoms and then slow those atoms. This selection and velocity reduction occurs by applying pulses of near-resonant light that manipulate the internal state of an atom and scatter photons while that atom oscillates spatially in a confining potential. The STOP cooling technique involves multiple steps that we collectively refer to as a STOP cooling cycle.

The first iteration of this laser cooling technique is described in a dissertation written by a previous graduate student from our research group [30], Rebekah Wilson. In that prior implementation, the ability to directly measure the temperature reduction was hindered due to substantial atom loss from the optical trap over the time required to complete a cooling experiment. The short optical trap lifetime (with respect to rethermalization timescales) in those experiments also meant that the effect of applying multiple STOP cooling cycles could not be easily studied. Furthermore, the optical trap configuration used in this prior work had an evaporation rate of atoms out of the trap that was too high. Lowering the background-gas pressure in the vacuum chamber was essential for performing a direct temperature reduction measurement and also for implementing multiple cooling cycles. Changing trap parameters to lower the evaporation rate was important as well. The solution to these two problems will be presented in turn.

In the absence of vacuum leaks, simply waiting a long enough period of time can lead to improved vacuum conditions. This is because the ion vacuum pump is continuously working to remove gaseous contaminants in the system. Between the first iteration of STOP cooling and the experiments presented in this chapter, the apparatus sat dormant for 6 - 12 months. This allowed the vacuum pressure to reach a level that led to improved optical trap lifetimes. The experimental

apparatus was revived from its dormant state, and we were able to perform direct temperature measurements of the ultracold gas after applying STOP cooling cycles. Unfortunately, this period of operation was short-lived due to the finite number of Rb getters in the vacuum chamber. We were forced to open the vacuum system to replace the Rb getters before we had completed the STOP cooling measurements we had planned. However, opening the system proved to be a blessing in disguise, as the newly baked vacuum system rapidly reached low pressure ($\sim 10^{-9}$ Torr), and ultimately the system produced an even longer optical trap lifetime. We not only had a fresh supply of new Rb getters to use for our experiments, but the optical trap lifetime was long enough to implement many successive STOP cooling cycles.

In addition to an improved vacuum environment, there was a modification of the optical trap parameters. The optical trap used in the first implementation had beam characteristics that resulted in power being displaced from the center of the beam when focused and imaged into the vacuum chamber. The effect from these optical aberrations was an anharmonic potential in the radial direction. In any confining potential with a finite potential depth, the highest energy atoms can gain enough energy to escape from the potential. The rate this occurs is a function of the atom temperature and the trap depth. This mechanism for atom loss was exacerbated by the radial anharmonicity in the first implementation. While there are subtleties [29], in general the initial temperature of the atoms changes more slowly than linearly with the trap depth. By changing optical trap optics, the confining laser beam was made to be smaller on the focusing lens to reduce optical aberrations, which had the effect of increasing the peak intensity at the optical trap focus despite the smaller spot size incident on the lens. This increased the trap depth, and in the end, the radial direction was more harmonic and the atom loss was reduced.

The following sections of this chapter will provide a detailed description of the STOP cooling technique. The description will include the theory used to model STOP cooling, predictions for expected energy reduction from applying STOP cooling to an ultracold gas, and our initial experimental implementation used to perform measurements of STOP cooling. A comparison between

model predictions and experimental results will be discussed, along with proposed improvements to the apparatus that are expected to increase the cooling performance.

4.1 A Novel Nonevaporative Technique

Laser cooling has enabled a large number of experiments at ultracold temperatures [10, 62–65]. The most common forms of laser cooling, Doppler and polarization gradient cooling, are useful as a first stage in laser cooling in a wide variety of systems. These have temperature limits such that additional cooling is needed in order to perform experiments in Bose-Einstein condensation [66, 67], Fermi degenerate gases [68, 69], precision atomic clocks [70, 71], ultracold molecule physics [72, 73], and other areas [74, 75]. Both evaporative cooling [76, 77] and laser cooling methods [35, 78, 79] beyond Doppler and polarization gradient cooling have been used to extend the temperature range for such experiments. Each method has advantages and disadvantages, and so the exploration of new techniques broadens the range of possible experimental parameters for advantageous laser cooling, allowing either improvements in experiments or enabling experiments to be performed that otherwise could not be.

STOP cooling is a novel nonevaporative cooling technique that adds to the viable methods available to the laser cooling community. The technique is designed to cool a gas of ultracold atoms that have been initially cooled and then confined in a conservative potential. In STOP cooling, the atoms need to have multiple ground states (e.g. different hyperfine states) so that some atoms can selectively be made to interact with a particular laser frequency while the remainder do not. Atoms in the latter category are referred to as being in "dark states" while those in the former are in "bright states". The main idea behind the cooling scheme is to use the fact that the atoms in a conservative potential oscillate spatially in that potential. The atoms thus continuously trade energy back and forth between potential energy and kinetic energy. By selecting atoms with high potential energy, waiting for that energy to be converted to kinetic energy, and then removing that kinetic energy via light scattering, STOP cooling reduces the temperature of the gas.

Our cooling technique has several advantages. First, STOP cooling is straightforward to implement in most ultracold atom experiments that use a MOT [62–64] (see section 2.3) as the first stage of laser cooling. Through the use of acousto-optic modulators (AOMs), all of the required STOP laser beams can be derived from the existing MOT beams. More broadly, STOP cooling makes efficient use of photons for cooling in that, as will be described in detail below, they are all directed opposite to average atom motion and only high-energy atoms scatter the light. Since cooling limitations are very often ultimately linked to the rate of photon scattering [80–82] efficient use of cooling photons is potentially quite advantageous. Experiments that can only initially achieve a limited number of trapped atoms would benefit from the fact that STOP cooling does not require the loss of the trapped atoms in order to cool. This technique has relatively few requirements for the internal structure of the atoms to be cooled, and so should be widely applicable. Again, the main requirements are the presence of dark and bright states and a confining potential. The availability of a cycling transition is useful, but not critical. This means that STOP cooling can be extended to cooling some types of ultracold molecules, although in that case an additional laser or lasers may be necessary, as will be discussed later in this chapter.

4.1.1 Overview of a STOP Cooling Cycle

As a first step in describing STOP cooling, we present an overview of the cooling technique. Our implementation of STOP cooling consists of a sequence of four steps, which are illustrated in figure 4.1. The starting point for STOP cooling begins with atoms in thermal equilibrium and trapped in a confining potential. It is assumed that all of the atoms are optically pumped into one or more dark states. The first step is to spatially overlap a laser beam with the edge of the trapped gas where the potential energy of the trapped atoms is the highest. The atoms that are in the region of overlap are optically pumped into an internal bright state. The optically pumped atoms are then given time to move on average to the center of the confining potential, where much of their initial potential energy is converted into kinetic energy. At this time, a scattering beam is directed opposite to the optically pumped atoms’ center-of-mass motion. By transferring linear

momentum from the scattering beam photons to the atoms that have been optically pumped, those atoms' center-of-mass velocity is reduced to zero. Once they have been slowed, the final step is to optically pump the atoms back into dark states. This results in a reduction of the average energy. Upon rethermalization, the temperature of the gas is reduced. STOP cooling is similar in some ways to one-way wall [83–86] and Sisyphus cooling techniques that rely on trapping potentials [87–90], but is very different from those in how the cooling mechanism works and because there is no need for the confining potential to depend on the internal state.

4.2 STOP Cooling Theory

To model STOP cooling, we begin with an idealized system where the confining potential is assumed to be a one-dimensional simple harmonic oscillator potential, and the spatial distribution of the atoms placed into the bright state at the edge of the confining potential is assumed to have an infinitely sharp axial cut-off position (the spatial position, z_c , in figure 4.1). The net result of these calculations are predictions of the average energy reduction in an ultracold gas after applying one STOP cooling cycle. We then extend our theoretical calculations to a three-dimensional system that includes the possibility of elastic collisions between atoms as the atoms oscillate in the trapping potential. This allows us to study how the cooling efficiency is impacted over a range of gas densities and therefore collision rates. Lastly, the simple harmonic oscillator potential is replaced with a more realistic trap shape, and we investigate the impact of using an anharmonic confining potential and a non-ideal (i.e. imperfect axial cut-off) initial bright-state atom distribution. To provide additional context for this last set of theoretical calculations, they will be presented (in section 4.7.2) after the experimental implementation and results sections.

4.2.1 Simple Harmonic Oscillator Model

In order to predict STOP cooling performance in a general way, we perform a series of calculations assuming idealized conditions. In these calculations, the atoms are assumed to be confined in a one-dimensional simple harmonic oscillator potential. The atoms are also assumed to be in

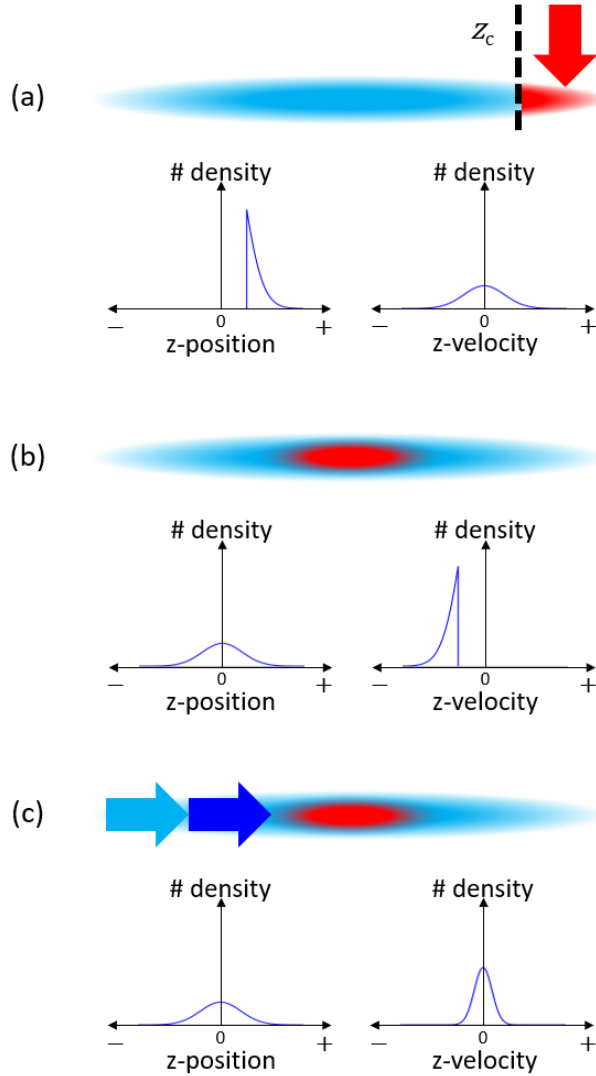


Figure 4.1: Depiction of a STOP cooling cycle. The light-blue oval represents confined ultracold atoms in a dark state, where the horizontal direction is the z -axis. The red represents atoms in a bright state. (a) Step 1 is the application of the laser beam (red arrow) that optically pumps atoms into a bright state. The dotted line, z_c , represents the edge of the laser overlap region where optical pumping is spatially truncated, leaving the remainder of the atoms in a dark state. (b) Step 2 is giving the bright state atoms' center-of-mass time to move to the center of the confining potential. (c) Step 3 is the application of the scattering beam (dark-blue arrow) that slows the bright state atoms' center-of-mass once it reaches the center of the confining potential. Step 4 is the application of the laser beam (light-blue arrow) that optically pumps atoms back into a dark state. The curves shown in each subfigure correspond to the bright state atoms' z -coordinate position and velocity distributions at the end of the corresponding step(s). The vertical axis for each curve is the number density of bright state atoms. Figure reproduced from [6].

thermal equilibrium. A characteristic oscillation frequency, ω , is chosen for the atoms. Their time-dependent positions and velocities are then determined using the basic equations of motion for a simple harmonic oscillator.

Assuming the atoms are in thermal equilibrium leads to a spatial density distribution proportional to $\exp(-U/(k_B T))$, where U is the harmonic trapping potential, k_B is Boltzmann's constant, and T is the temperature of the gas. The experiment is performed with ^{87}Rb , so its mass, m , and parameters appropriate to its $5S_{1/2}$ to $5P_{3/2}$ cycling transition (see figure 3.1) are used for these calculations. To model the spatial selection in the first step of the technique, a cooling cycle calculation starts by identifying all of the atoms with a spatial position greater than an axial cut-off distance, denoted by z_c in figure 4.1, as atoms that will be subjected to the STOP laser beams. To model the optical pumping process in the first step of STOP cooling, each of these atoms is assumed to randomly scatter photons from the first STOP cooling beam such that each photon scatter has a 50% probability of transferring the atom into the bright state. It is also assumed that enough photons are scattered by these atoms so that all are in the bright state, and the number of photons scattered by a given atom is labeled as n_1 . Physically, the cut-off distance corresponds to the ideal edge of the laser overlap region in the experiment where atoms with the highest potential energy were optically pumped into a bright state.

With a well-defined fraction of atoms in a bright state, the next step of the calculation is to allow those high-energy atoms' center-of-mass to move to the center of the harmonic potential. The ideal time that allows the atoms' center-of-mass to reach a maximum velocity is used ($\frac{1}{4}$ period of the atoms' oscillation in the potential). After this time, the bright state atoms' center-of-mass is slowed by simulating the application of a scattering laser beam. This is done by simulating scattering photons directed opposite to the atoms' center-of-mass motion. We assume that each bright state atom randomly scatters n_2 photons according to a Poisson distribution, $P_{\bar{n}}(n_2)$, where \bar{n} is the mean number of photon scatters. Once the atoms' center-of-mass has been slowed, the last step is to close the STOP cooling cycle by optically pumping the atoms back into their original dark state. It is assumed that each atom randomly scatters photons from this final beam with each scatter

resulting in a 50% probability of the atom being optically pumped to the dark state. The number of photons scattered by an atom in this step is labeled n_3 . Since this final optical pumping beam propagates in the same direction as the scattering beam, it also provides slowing power for the atoms' center-of-mass motion. An absorbed photon from the scattering beam or the final optical pumping beam is assumed to impart $\hbar k$ of momentum (where \hbar is the reduced Planck constant and $k = 2\pi/\lambda$ where λ is the wavelength) directed along the z -axis.

Putting the above considerations together leads to the following set of equations to model the change in energy from a single STOP cooling cycle. Equation (4.1) is the normalized one-dimensional Maxwell-Boltzmann thermal phase space density describing the position and velocity distribution of the atoms at time $t = 0$ (where z_0 is the initial position and v_0 is the initial velocity). Equation (4.2) is the average energy of the bright state atoms as a function of n photons scattered, where $n = n_2 + n_3$. Equation (4.3) is the average single-cycle energy reduction as a function of \bar{n} . Note that the integrations in (4.2) and (4.3) are over the initial condition variables and the limits of integration extend over all relevant positions and velocities for the bright state atoms

$$f(z_0, v_0) = \frac{m\omega}{2\pi k_B T} \exp\left(-\frac{m}{2k_B T}(v_0^2 + \omega^2 z_0^2)\right), \quad (4.1)$$

$$E(n) = \int_{-\infty}^{\infty} dv_0 \int_{z_c}^{\infty} dz_0 f(z_0, v_0) \left\{ \frac{m}{2} \left[\left(n \frac{\hbar k}{m} - \omega z_0 \right)^2 + v_0^2 \right] \right\} \\ + n \frac{(\hbar k)^2}{2m} \int_{-\infty}^{\infty} dv_0 \int_{z_c}^{\infty} dz_0 f(z_0, v_0), \quad (4.2)$$

$$\Delta E = \sum_{n_1=1}^{N_1} \frac{(n_1 + n_1^2)}{2^{n_1}} \frac{(\hbar k)^2}{2m} \int_{-\infty}^{\infty} dv_0 \int_{z_c}^{\infty} dz_0 f(z_0, v_0) \\ + \sum_{n_3=1}^{N_3} \sum_{n_2=1}^{N_2} \frac{1}{2^{n_3}} P_{\bar{n}}(n_2) [E(n) - E(0)]. \quad (4.3)$$

The second double integral term in (4.2) accounts for the recoil energy from a spontaneously-emitted photon that occurs after each absorption from the scattering beam or final optical pumping beam. Additionally, the energy imparted from absorbing and scattering n_1 photons from the first optical pumping beam is included as the first summation in (4.3). The upper limits for the summations are chosen to be large enough to ensure convergence of the sums to our desired precision. Using parameters based on our experiment, we calculate the cooling-cycle-induced change in energy ΔE . The mean number of photons scattered in the Poisson distribution is optimized to produce maximum cooling. The net result of this calculation is a prediction of the amount of energy removed in one STOP cooling cycle.

Figure 4.2 shows the results of this calculation for a range of initial temperatures. For each curve, the axial cut-off distance is continuously adjusted so that the selected bright state atom fraction remains constant. This calculation is repeated for several different optically pumped fractions. Being more selective by optically pumping a smaller fraction tends to increase the amount of energy removed per selected atom, but tends to decrease the total energy removed from the gas since fewer atoms are selected. In figure 4.2, the 25% fraction of optically pumped atoms has the highest predicted energy reduction rate, although the 15% and 10% fractions are only slightly lower. As the temperature decreases the energy reduction becomes less efficient as the heat imparted by absorption and random recoils during scattering becomes more important.

4.2.2 Impact of Elastic Collisions

The rate at which energy is removed depends on the time that a STOP cooling cycle takes. For typical confining potentials this will often be on the order of several ms. For a sense of scale, the per atom energy removal rate for the whole gas for a 25% selected fraction and 50 μK initial gas temperature with a 20 ms STOP cooling cycle time is $5.8 \times 10^{-27} \text{ W} = k_{\text{B}} \cdot 420 \mu\text{K s}^{-1}$. While this provides a scale for the energy removal rate, it is not directly a temperature reduction rate as energy is removed in one dimension and STOP cooling distorts the velocity distribution away from equilibrium. Depending on different alignments of lasers, STOP cooling can in principle

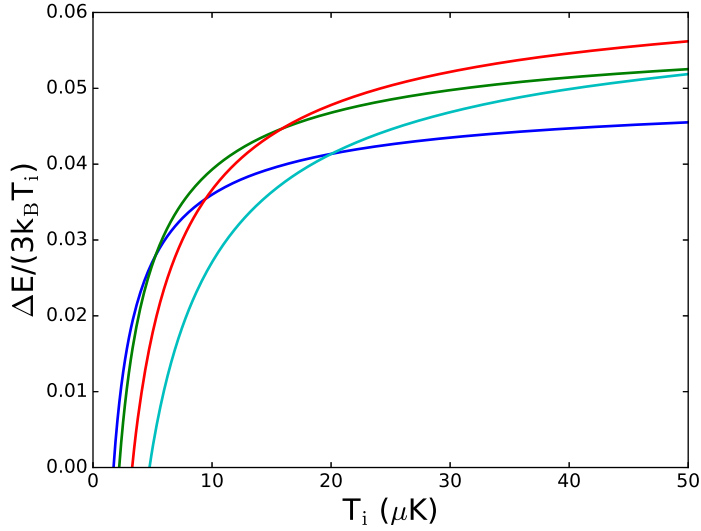


Figure 4.2: Energy reduction per atom in the gas from a single STOP cooling cycle for a selected fraction of bright state atoms. T_i denotes the initial temperature of the gas. The blue curve corresponds to a 10% selected fraction, the green curve corresponds to a 15% selected fraction, the red curve corresponds to a 25% selected fraction, and the teal curve corresponds to a 35% selected fraction. While the calculation is performed in a one-dimensional model, the energy reduction fraction is calculated using a denominator appropriate to the total energy of a gas confined via a simple harmonic oscillator potential in three dimensions for easier comparison to experiments. Figure reproduced from [6].

be applied in three-dimensions or there can be mixing of motion between the dimensions through energy mixing in the confining potential. In the absence of those mechanisms, energy mixing between dimensions will occur naturally via collisions between atoms. To characterize collision-induced cross-dimensional energy reduction rates and the effect of collisions on STOP cooling, we performed an additional set of calculations.

These additional calculations consisted of a three-dimensional calculation of STOP cooling where we included the possibility of collisions for any atom during the bright state atoms' center-of-mass motion. To avoid the computational difficulties of a direct N^2 -type binary collision simulation, we calculated an average collision probability for each atom in each timestep based on local density and temperature parameters and then generated a random number to see if a collision occurred. If a collision occurred for an atom, its velocity was changed by simulating an isotropic collision of that atom with a randomly-generated representative "target" atom given the temperature-determined velocity distribution. While computationally more efficient than a more

complete N^2 -type calculation, this treatment ignores the possibility of non-isotropic scattering and precise details of the atoms' density and velocity distribution during STOP cooling. However, we expect these considerations to be small and this calculation sufficient for characterizing the general impact of collisional effects on STOP cooling.

To evaluate the effect of collisions, we identified the following timescale to quantify the energy reduction rate of STOP cooling: the time period, Δt , required to reach 20% overall energy reduction in the gas using continuous STOP cooling cycles. This time period was determined for both a 10% selected fraction and a 25% selected fraction over a range of collision rates spanning two orders of magnitude. We calculated both the total energy reduction rate over time Δt and the energy reduction rate in only the non-STOP-cooled radial directions as well. Since energy in the radial directions is removed only through the actions of collisions, examining radial energy reduction is useful for evaluating the influence of collisions. The results of these calculations are shown in figure 4.3.

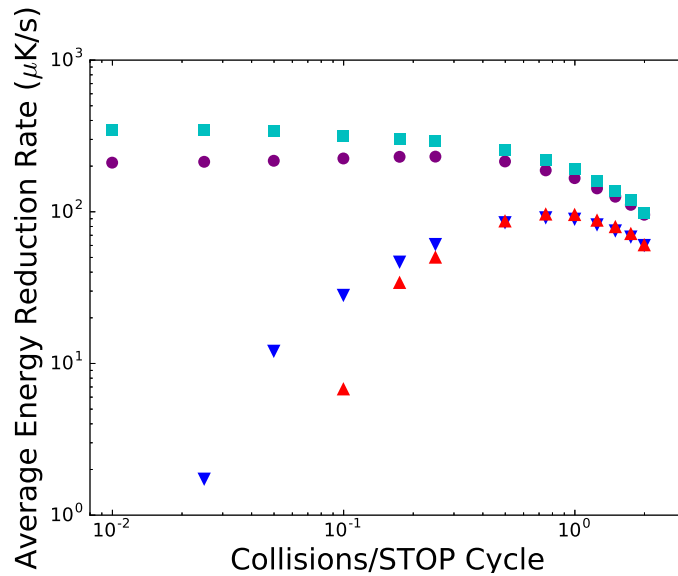


Figure 4.3: Impact of elastic collisions on total and radial energy reduction rates (in temperature units, i.e. average energy divided by k_B) in STOP cooling. The purple circles correspond to total energy reduction rates from STOP cooling using a 10% selected fraction. The teal squares correspond to total energy reduction rates from STOP cooling using a 25% selected fraction. The blue downward triangles correspond to radial energy reduction rates from STOP cooling using a 10% selected fraction. The red upward triangles correspond to radial energy reduction rates from STOP cooling using a 25% selected fraction. Note that the horizontal and vertical axes have logarithmic scales. Figure reproduced from [6].

Figure 4.3 indicates that STOP cooling results in energy reduction over a range of gas densities and collision rates. Because collisions disrupt the bright state atoms' center-of-mass motion during the second step of STOP cooling (see figure 4.1(b)), total average energy reduction is highest when no collisions are present. For the radial directions, (under the assumptions used for the calculation) energy reduction can only occur through collisions. This leads to the radial energy reduction rate increasing as the collision rate increases and then turning over as collisions reduce the STOP cooling energy reduction rate. The calculation included some heating in the radial direction from random photon scatters, and so a minimum collision rate is necessary to achieve net energy reduction in the radial direction.

Techniques or trap configurations that mix radial and axial energy will result in faster radial energy reduction rates than the rates shown in figure 4.3. Even in the absence of such considerations, STOP cooling is still effective for three dimensional cooling even when applied along one dimension over a range of collision rates. STOP cooling's reliance on the motion of the atoms reduces its intrinsic cooling rate to be less than some other extensions to laser cooling (e.g. Raman cooling [79, 91]). Ultimate achievable temperatures, however, are a balance between cooling and heating effects and STOP cooling has favorable considerations in that regard. Because the direction of the scattering beam is directly opposed to the atoms' center-of-mass motion, the atoms' center-of-mass motion is slowed with a small number of photon scatters. Since the typical timescale of trapped ultracold atoms is on the order of milliseconds and the technique works with the scattering beam on or near resonance, intensities on the order of 10^{-3} of the saturation intensity are sufficient for the scattering beam. Alternatively, substantially larger detunings and correspondingly larger intensities could be used instead if that were advantageous. In addition to practical advantages, this low level of photon scattering rate can be used to mitigate reabsorption-based heating effects [62, 63, 80, 92] that limit light-based cooling. Moreover, the most effective radial cooling range in figure 4.3 corresponds to the range where collisions typically start to disrupt other laser cooling techniques (e.g. [79, 91]).

4.2.3 Comparison to Evaporation

In the presence of elastic collisions, it becomes relevant to compare predicted STOP cooling energy reduction rates to a purely collision based cooling mechanism. To perform such a comparison, we calculate the average energy reduction rate from simple evaporative cooling that would occur during a time required to reach 20% overall energy reduction in the gas using continuous STOP cooling cycles. This is the same time defined as Δt in section 4.2.2. The final average energy of the gas after evaporation can be expressed as

$$E_f = \frac{3k_B T - \eta \nu_c U_0 \exp(-\eta) \Delta t}{1 - \eta \nu_c \exp(-\eta) \Delta t}, \quad (4.4)$$

where U_0 is the depth of the confining potential, $\eta = U_0/(k_B T)$, and ν_{col} is the collision rate in the gas. This is an approximate treatment of evaporative cooling, since here the temperature and density are considered constants during Δt . We use (4.4) to calculate the average energy reduction rate, $(E_f - 3k_B T)/\Delta t$, that results from evaporation. We then determine the ratio of STOP cooling rates to evaporative cooling rates for the Δt of the 10% selected fraction and the Δt of the 25% selected fraction. The results of these calculations are shown in figure 4.4.

Figure 4.4 shows that the STOP cooling energy reduction rate is faster than that of evaporation over the entire range plotted. At the lowest collision rates used for the calculations, STOP cooling results in an average total energy reduction rate that is orders of magnitude larger than what would be expected when relying solely on evaporative cooling. While STOP cooling works over a large range of gas densities, it is best adapted to low density situations and would be particularly advantageous in situations where low density is either desirable or necessary. When no collisions (or other energy mixing mechanisms) are present, the gas will not rethermalize and STOP cooling is asymptotically limited to an amount of energy that can be removed from the axial direction. As collisions begin to increase from non-zero, STOP cooling is able to remove additional energy from the radial direction (see figure 4.3) while also staying closer to thermal equilibrium. There is a wide range of collision rates where STOP cooling is 10 - 100 \times faster than evaporative cooling where there are still collisions that can thermalize the gas.

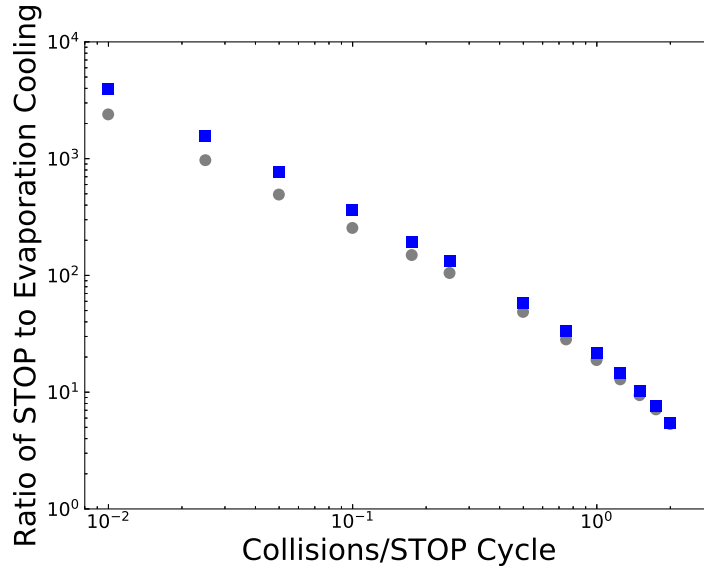


Figure 4.4: Ratio of STOP cooling total average energy reduction rate to simple evaporative cooling average energy reduction rate. The gray circles correspond to the ratio of energy reduction rates from STOP cooling using a 10% selected fraction to evaporative cooling. The blue squares correspond to the ratio of energy reduction rates from STOP cooling using a 25% selected fraction to evaporative cooling. Each ratio is determined using an equivalent time for STOP cooling and evaporation at a particular collision rate (see main text for definition of timescale used). Note that the horizontal and vertical axes have logarithmic scales.

4.3 Extension to Molecules

While we have focused on atoms so far, STOP cooling can be extended to cooling of molecules. Those molecules which can be cooled and trapped in a MOT are prime candidates [93–96]. Recent progress in laser cooling optically trapped diatomic calcium monofluoride [97, 98] motivates the following described adaptation of STOP cooling, and so the following discussion will be presented in the context of that particular system.

Figure 4.5 shows the relevant energy levels [99] that could be used to implement STOP cooling in optically trapped CaF. Initializing the molecules by placing them into a dark state is accomplished by optically pumping into the $X(\nu = 1)$ electronic ground state via the $X(\nu = 0) - A(\nu' = 1)$ transition. The first step of STOP cooling is the application of the beam that optically pumps the molecules into a bright state (see figure 4.1(a)). In this case, the bright state is the $X(\nu = 0)$ electronic ground state. After waiting for the bright state molecules' center-of-mass to move to the center of the optical trap (see figure 4.1(b)), a scattering beam slows the center-of-mass velocity

by scattering photons on the $X(\nu = 0) - A(\nu' = 0)$ transition. The final step is to optically pump the molecules back into the $X(\nu = 1)$ dark state (see figure 4.1(c)). Many of these beams are duplicates of those used in the MOT cooling stage. Hyperfine structure would require either AOMs or a few stages of each STOP cooling step. It is likely the trapped molecule densities will continue to improve as techniques develop, making the advantages of STOP cooling increasingly relevant to such systems.

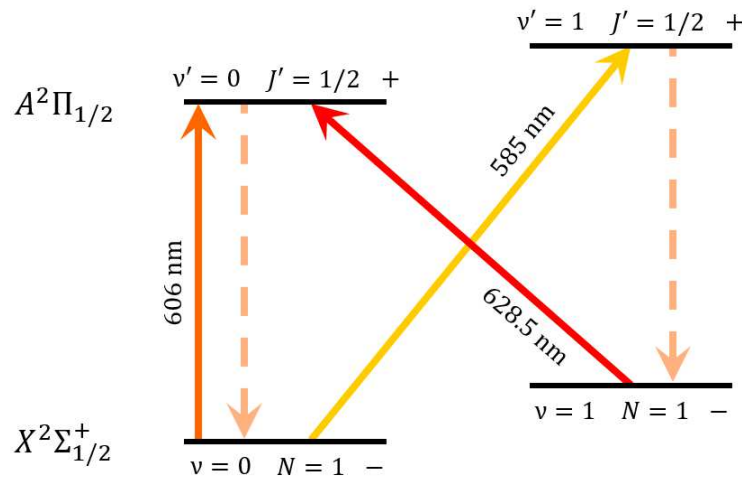


Figure 4.5: Relevant energy levels for STOP cooling CaF molecules. The red solid arrow (628.5 nm) corresponds to the beam used to optically pump molecules into a bright state. The orange solid arrow (606 nm) corresponds to the scattering beam used to slow the bright state molecules' center-of-mass. The yellow solid arrow (585 nm) corresponds to the beam used to optically pump atoms into the dark state. The dotted lines correspond to spontaneous emission (606 nm). Figure reproduced from [6].

An alternative implementation of STOP cooling optically trapped CaF could rely on the hyperfine structure in $X^2\Sigma_{1/2}^+(\nu = 0, N = 1)$ [96, 99, 100] to serve as dark and bright states. The 606 nm laser (see figure 4.5) with AOMs is then used to both optically pump and cool the molecules so the need for a 585 nm laser is eliminated. The 628.5 nm laser remains in the scheme to pump molecules back to the $X(\nu = 0)$ electronic ground state in the event of vibrational branching that will occur over the course of many STOP cooling cycles. By using only the hyperfine levels, existing experiments that laser cool optically trapped CaF can immediately adapt STOP cooling into their system without requiring an additional laser. The disadvantage with this implementation is

that the comparatively close (~ 100 MHz) resonant frequencies between the different hyperfine states will limit the range of detunings that can be used as compared to the scheme shown in figure 4.5. However, as long as conditions allow for all of the STOP beams to be nearly on-resonance, this alternate approach should be effective for STOP cooling in this system.

4.4 Experimental Implementation

Our experimental measurements of STOP cooling were conducted with ultracold ^{87}Rb atoms. In our experimental realization of STOP cooling there is a laser beam for each beam depicted in figure 4.1. These beams are straightforwardly derived by inserting an AOM into beam paths associated with the usual MOT cooling and repump lasers as appropriate. The first laser beam is responsible for optically pumping atoms from the lower hyperfine ground state ($5S_{1/2} F = 1$; dark state) into the upper hyperfine ground state ($5S_{1/2} F = 2$; bright state). We will refer to this beam as the "up-pump" beam and atoms in the upper hyperfine ground state will be referred to as "up-pumped" atoms. The next step in the cooling cycle is the application of the scattering beam that opposes the up-pumped atoms' center-of-mass motion at the center of the confining potential. This beam will be referred to as the "stop" beam. The light of the stop beam is tuned to the $5S_{1/2} F = 2$ to $5P_{3/2} F = 3$ cycling transition. Finally, the last step in the cooling cycle is to optically pump atoms back into the lower hyperfine ground state ($5S_{1/2} F = 1$). The laser beam responsible for this will be referred to as the "down-pump" beam. A schematic depicting the experimental implementation of STOP cooling is shown in figure 4.6.

We started our experiments by loading ultracold ^{87}Rb atoms from a MOT into a FORT [27] (see section 2.4). The MOT was prepared using standard techniques [22] and the FORT was created using an AOM-controlled 60 W (10.64 μm wavelength) CO_2 laser beam focused to a spot size of approximately 120 μm . The focus of the CO_2 laser beam was overlapped with the MOT atoms and loading from the MOT into the FORT was performed following the techniques of [101, 102]. Once loaded into the FORT, the atoms were given several seconds to reach thermal equilibrium. This resulted in a trapped gas of ultracold ^{87}Rb atoms with a peak spatial density of $5 \times 10^{11} \text{ cm}^{-3}$ and

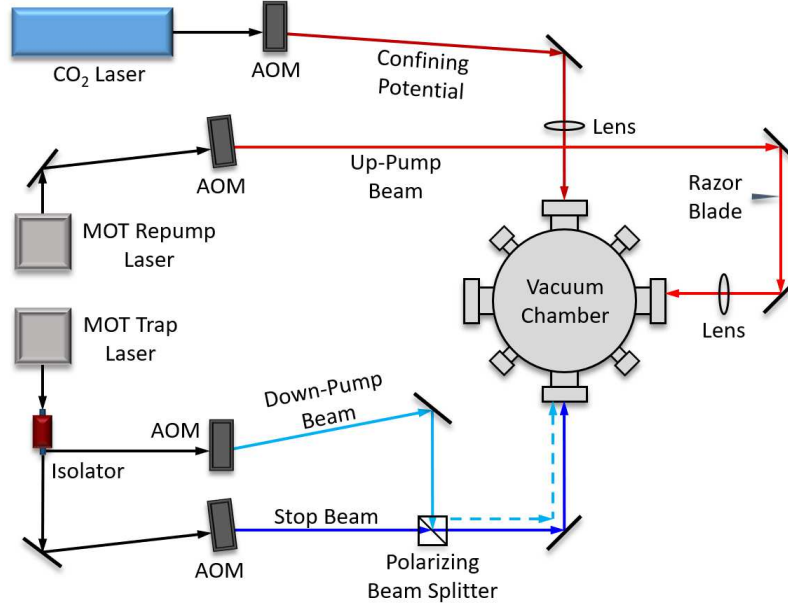


Figure 4.6: Schematic of the experimental set-up used to perform STOP cooling. The confining potential, up-pump beam, stop beam, and down-pump beam are pictured. The portion of the down-pump beam depicted as a dotted line is overlapped with the stop beam. The beams used to form the initial MOT and the probe beam used for absorption imaging are left out for clarity. Note that all three beams used for STOP cooling are derived from existing MOT lasers. Figure reproduced from [6].

a temperature of $45 \mu\text{K}$. The atom temperature is measured to a precision of less than a percent while the accuracy of the measurement is estimated to be about 20%. The confined atoms had axial and radial oscillation frequencies of 14 Hz and 550 Hz, respectively, measured with an accuracy at the 10% level. These parameters lead to a collision rate of approximately 0.16 Collisions per STOP cycle.

4.4.1 STOP Cooling Beams

After reaching thermal equilibrium in the confining potential, the trapped atoms were optically pumped into the lower hyperfine ground state ($5S_{1/2} F = 1$). STOP cooling cycles were then applied to the gas. The up-pump laser beam was overlapped with the edge of the FORT for $500 \mu\text{s}$ to "up-pump" the selected atoms. A sharp edge corresponding to the axial cutoff position for the overlap region was realized by partially blocking the up-pump beam with a razor blade external to the vacuum chamber. The edge of the razor blade was imaged onto the atoms using a lens.

After being up-pumped, those atoms' center-of-mass was then allowed to move to the center of the trapping potential, where it reached a maximum velocity. At that time, a 1 ms duration stop beam pulse was applied to slow the center-of-mass velocity of the up-pumped atoms. Immediately following the stop beam was a 1 ms down-pump beam used to optically pump the up-pumped atoms back to the lower hyperfine ground state ($5S_{1/2} F = 1$), thus completing a single cycle of STOP cooling.

Each intermediate step of the STOP cooling cycle was individually optimized. The up-pump beam was tuned 25 MHz below the $5S_{1/2} F = 1$ to $5P_{3/2} F = 2$ transition and the intensity of the beam was set to optically pump all of the overlapped atoms into the upper hyperfine ground state ($5S_{1/2} F = 2$). The experiments were performed using a 10% selected fraction. With a well-defined fraction of up-pumped atoms, we then measured the amount of time it took the atoms' center-of-mass to reach the middle of the optical trap to determine the time to apply the stop laser pulse. The stop beam was tuned to be approximately on-resonance with the $5S_{1/2} F = 2$ to $5P_{3/2} F = 3$ cycling transition and its intensity was adjusted to reduce the up-pumped atoms' center-of-mass velocity to zero at the optical trap center. Finally, the down-pump beam was tuned 5 MHz below the $5S_{1/2} F = 2$ to $5P_{3/2} F = 2$ transition and the intensity of the beam was set to optically pump all of the up-pumped atoms back into the lower hyperfine ground state ($5S_{1/2} F = 1$). The selected fraction of up-pumped atoms, the time for the atoms' center-of-mass to reach the middle of the optical trap, and the optimal intensity of each beam were determined through absorption imaging. For instance, after applying the stop beam, images of the up-pumped atoms were collected at increasingly later times to observe whether or not the atoms' center-of-mass had moved between frames. The stop beam intensity was adjusted using absorptive neutral density filters until the center-of-mass remained in the middle of the optical trap in each of the images.

4.4.2 Single Cycle to Multiple Cycles

Once the single-cycle optimizations had been determined, the application of multiple cycles was performed. We began by measuring the cooling from 3 successive cycles and then from

5 successive cycles. From there, we added 3 additional STOP cooling cycles to each cooling experiment (i.e. 8 cycles, 11 cycles, etc.) until reaching 20 successive cooling cycles. At that point, we broke up the application of STOP cooling into "blocks", which consisted of 20 cooling cycles applied successively. Blocks were then separated by a rethermalization time estimated from collision rate calculations. This gave time for the gas to reestablish thermal equilibrium, allowing for further temperature reduction through the application of additional STOP cooling blocks. Our final STOP cooling experimental procedure consisted of 3 blocks of 20 successive cycles, with each block followed by a 500 ms rethermalization time. The total duration for 3 blocks of 20 successive cycles plus rethermalization periods was between 2.64 s to 2.76 s, with the variation owing to slight differences in the time between the up-pump and the stop pulses that we deliberately introduced to search for optimal multi-cycle cooling parameters.

4.5 STOP Cooling Data

After the STOP cooling cycles and rethermalization were completed, data collection was performed using standard time-of-flight and absorption imaging techniques. The absorption imaging allowed the determination of the number of atoms in the trap and the temperature of the gas. This is the main diagnostic that we use in order to evaluate how much cooling has occurred.

Three types of absorption measurements were taken to characterize the amount of STOP cooling. The first type of measurement was taken at the beginning of the STOP cooling sequence to measure the initial temperature of the gas. The second type of measurement was taken after the STOP cooling cycles had been applied to measure the final temperature of the gas. The third type of measurement was taken at an equivalent time required to complete the STOP cooling cycles, but without applying any STOP cooling to the gas. The difference between the first and third types of measurements indicated there was a small amount of evaporative cooling over the time scale measured.

As one way to analyze our data, our two-dimensional absorption images of the the gas were integrated along the shorter (radial) extent of the gas to produce one-dimensional spatial density

distributions. To do this, the pixels in a processed image file were divided into bins along the axial direction of the gas. The pixel values were summed in each bin to produce a one-dimensional spatial density profile of the confined atoms. Figure 4.7 shows such a set of binned data depicting the spatial density profiles of each of the three types of measurements described in the previous paragraph. STOP cooling produces a clear reduction of high energy atoms at the edges of the spatial density distribution and a corresponding increase in peak spatial density at the center of the distribution.

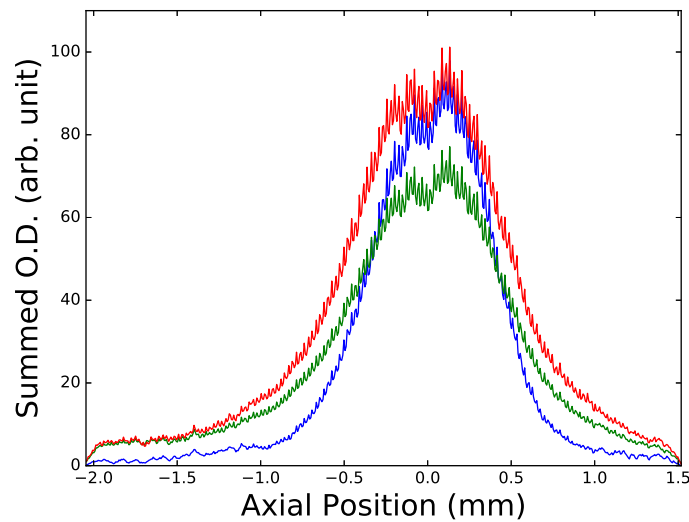


Figure 4.7: One-dimensional spatial density profiles of confined atoms. O.D. is the optical depth. The blue curve is a measurement taken after STOP cooling cycles have been applied to the gas. The green curve is a measurement of atoms that have been held for an equivalent amount of time required to complete the STOP cooling cycles but without applying any cooling cycles. The red curve is a measurement taken at the beginning of a STOP cooling experiment before any cycles have been applied to the gas. Figure reproduced from [6].

4.6 STOP Cooling Results

Figure 4.8 shows the results for the temperature reduction as a function of an increasing number of applied STOP cooling cycles. From these data we derived a single-cycle cooling efficiency of 0.0091(5) fractional temperature reduction. For our STOP cooling experiment consisting of

3 blocks of 20 successive cycles conducted under the optimal conditions that we examined, we measured a 0.282(4) fractional temperature reduction for the cooled atoms compared to the initial gas temperature. Over the same time period, the mild evaporation described in section 4.5 resulted in only a 0.031(4) fractional temperature reduction. Thus, STOP cooling produced a significant and well-resolved temperature reduction in the gas.

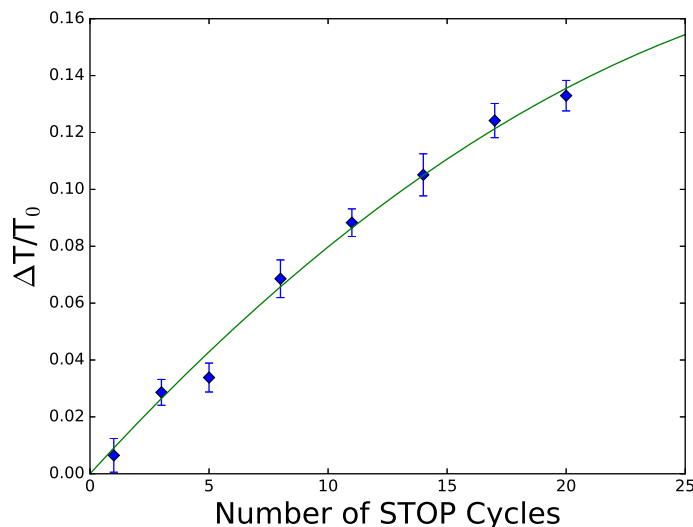


Figure 4.8: Fractional temperature reduction resulting from the application of successive STOP cooling cycles. T_0 is the temperature of the gas when no STOP cooling cycles have been applied. T_0 is measured at an equivalent amount of time required to complete the corresponding number of STOP cooling cycles and rethermalization for a given data point (blue diamonds). ΔT is the difference between T_0 and the temperature of the gas after STOP cooling cycles have been applied. The green curve is a second-order polynomial fit to the data. Figure reproduced from [6].

The number of atoms in each measurement were also calculated, and we observed a 0.71(1) fraction of atoms remaining in the gas that had STOP cooling applied versus a 0.75(2) fraction of atoms remaining in the gas with no STOP cooling applied. The majority of the atom loss in both cases is due to the background-gas-determined 10 second lifetime of atoms in the optical trap. The difference with and without STOP cooling translates to $7(4) \times 10^{-4}$ fractional atom loss per cooling cycle. Therefore, substantial cooling with small atom loss was observed with STOP cooling. We attribute the small loss from applying STOP cooling cycles to be a result of light-assisted collisional loss effects [103–105] where near-resonant laser light induces dipole moments

in the atoms. These dipoles can produce interatomic forces strong enough to accelerate some pairs of atoms out of the optical trap.

In terms of a cooling rate, the 3 blocks of 20 successive cycles resulted in a temperature reduction rate of $4.7 \mu\text{K s}^{-1}$, as determined by the radial temperature. Converting this rate to a total energy reduction rate results in $k_B \cdot 14.1 \mu\text{K s}^{-1}$ and converting to a total radial energy reduction rate results in $k_B \cdot 9.4 \mu\text{K s}^{-1}$. These rates demonstrate the efficacy of the cooling technique and we expect these rates to increase with improvements to the experimental apparatus. While clear evidence of successful cooling was obtained, the measurement of $0.0091(5)$ fractional temperature reduction from a single cycle of STOP cooling is approximately 5 times smaller in magnitude than the temperature reduction predicted from the harmonic oscillator potential model in this implementation of STOP cooling. Details of why this is the case along with improvements to the experiment will be discussed in the next section.

4.7 Comparing Measurements to Predictions

The difference between predicted and measured temperature reduction is due to the fact that our experimental system deviated from the assumptions of the ideal calculation. First, the actual confining potential was not harmonic. Second, the axial cut-off distance for the optically pumped atoms at the edge of the potential was not infinitely sharp. Finally, the confining potential in the experiment was non-separable in the radial and axial directions. For the most part, these deviations are not inevitable and so understanding them is useful in achieving closer-to-ideal performance in future implementations.

4.7.1 Possible Heating from Optical Pumping

Before describing the impact of the known imperfections on the cooling rate, we consider the possibility of additional heating beyond the minimum amount of recoil heating from the beams used to optically pump the high energy atoms in the first and last step of a STOP cooling cycle. To search for any unusually large heating from such a mechanism, a fraction of atoms at the edge of

the trap was optically pumped to the $5S_{1/2} F = 2$ state, allowed to move to the center of the trap, and then was optically pumped back to the $5S_{1/2} F = 1$ state. This was performed using 10 or more successive cycles, all of which were in the absence of the intermediate stop beam. The same experiments were repeated but without performing any optical pumping (i.e. the atoms were held for an equivalent amount of time without applying any light). Comparing the temperatures with and without the atoms being optically pumped indicated a decrease in temperature of approximately 70 nK per cycle. Rather than heating, this test produced a small amount of cooling, likely owing to the fact that the down-pump beam has stop beam-like characteristics. In any case, there was no evidence of any excess heating.

4.7.2 Realistic Optical Trap Shape

To gain further insight as to where cooling efficiency losses may have occurred, we developed a more extensive model of STOP cooling than the idealized collisionless calculation described in section 4.2.1. We replaced the harmonic oscillator potential with a more realistic optical trapping potential and performed a three-dimensional calculation. We also included a non-ideal axial cut-off region instead of an infinitely sharp cut-off.

In this more extensive model we simulated atom motion and all of the applied STOP beam pulses numerically. We used random number generation to initialize atom positions and velocities given a thermal equilibrium distribution, and modeled photon scattering through determining the random number of photons scattered given the average photon scattering rate. For the optical potential, we used the approximate potential

$$U = U_0 \frac{1}{1 + (z/z_R)^2} \exp\left(-\frac{2r^2}{w_0^2(1 + (z/z_R)^2)}\right), \quad (4.5)$$

where z and r are the axial and radial position coordinates, respectively, U_0 is the trap depth, $z_R = \pi w_0^2 / (\Lambda M^2)$ is the Rayleigh length, w_0 is the spot size of a Gaussian laser beam, Λ is the optical trap wavelength, and M^2 is to correspond to the beam quality factor. For $M^2 = 1$ this would be exact, but our beam did not have an M^2 value of one and the potential in (4.5) allows

an approximation of the effect that will have, without being an exact match to an optical potential. Through this simulation, we could model the energy reduction in a single cycle of STOP cooling for more realistic experimental parameters.

We concentrated our initial studies assuming a 10% up-pumped fraction and we varied the M^2 value to alter the anharmonicity of the potential. The deviation from $M^2 = 1.0$ estimated through the effective axial oscillation frequency and the confined atoms' spatial extent was determined to be $M^2 = 1.65$. The increased axial anharmonicity in the model potential resulted in further reduction of cooling efficiency compared to the harmonic confining potential predictions. We also conducted calculations where we accounted for the influence of the non-ideal edge of the axial cut-off. Given the measured experimental axial cut-off width, a sigmoid function was used to model the non-ideal cut-off for the initial spatial density distribution of the 10% up-pumped fraction and additional lowering of the cooling efficiency was observed. With these considerations, the experimentally observed reduction in single cycle cooling efficiency can be reproduced by model parameters consistent with the non-TEM₀₀ optical trap beam and imperfect axial cut-off.

4.7.3 Apparatus Improvements

While cooling was experimentally observed, more realistic modeling suggests that our single-cycle temperature reduction could be increased by at least a factor of 2 for the same initial conditions while still using a realistic optical trap. To realize this increase in cooling, several improvements for the next iteration of experiments are expected to be advantageous. A sharper edge for the optically pumped region of the gas can be achieved by using a higher-quality lens to image the razor edge. Since our modeling indicates the amount of cooling depends on the shape of the confining potential, the trapping potential specific to our experiment can be improved by switching to a fiber laser, resulting in a higher quality TEM mode.

Additionally, other gains in the temperature reduction can be made in the multi-cycle cooling experiments. As the gas cools, the axial extent becomes smaller. This in turn reduces the region of overlap between the confining potential and the beam used for optically pumping atoms in the

first step of STOP cooling. Rather than a static overlap position, the relevant lens can be mounted to a motorized translation stage and used to deflect the optical pumping beam during multi-cycle cooling to better maintain an optimal optically pumped fraction as the cooling proceeds. In fact, such an improvement is required in order to obtain a meaningful determination of the lowest temperatures that could be achieved with this cooling technique.

4.7.4 Ways to Mitigate Limitations

For this initial implementation of STOP cooling, the long cooling time combined with the finite background lifetime resulted in losses that hindered the phase space density increase of the gas. Enhancing the cooling rate through addressing the imperfections described above and extending the cooling further to lower temperatures will improve this factor substantially. The phase space density increased by a factor of 2.3 over the course of the 3 block experiment. Addressing the known imperfections identified in the prior section would result in a higher phase space density increase. After addressing the known imperfections of the system, the limitations to further performance increases due to other factors may become significant, however.

For instance, light-assisted collisional losses will become more significant at higher atom densities [106], and would be substantial at a density an order of magnitude higher than that of the current experiments. Due to the flexibility of the scheme, the wide parameter space (i.e. detuning, intensity) available for exploration, and the difference in the dependence of light-assisted collision rates and light scattering rates on experimental parameters, we expect an acceptable region of operation could very likely be found. Searching for such an acceptable region is far easier when the light-assisted collision losses are more easily detectable.

Light-based cooling schemes also suffer when the gas being cooled becomes sufficiently optically thick [80–82]. Adjusting the detuning of the light used for cooling cannot remove this issue as two-photon detuning-independent effects contribute to heating. We saw no evidence of reabsorption-related effects for our conditions, but again an increase in performance and therefore optical depth could possibly cause this common limitation to cooling to become significant for

STOP cooling. The efficient use of photons, very low required photon scattering rates, and the fact that the cooling does not have to occur between particular magnetic sublevel combinations means that STOP cooling is much less sensitive to this physics than other cooling techniques, however. Additional routes to mitigate this optical-density-related limit include reducing the selected fraction of bright state atoms or applying a magnetic field to produce slight Zeeman shifts. These mitigation techniques may introduce different problems (e.g. smaller fractions would result in a slower cooling rate) so any implementation would need to be evaluated.

4.8 STOP Cooling Conclusions

We have presented a description of a new cooling technique for ultracold gases. The technique is based on using STOP to create a group of atoms that move in a known direction at a known time such that they can be slowed with light. The cooling technique only requires that a gas be trapped and that a dark state exists for the technique to be applicable. We have performed experimental measurements that demonstrated the cooling method. We observed a $0.0091(5)$ fractional single-cycle temperature reduction and a $0.282(4)$ fractional temperature reduction from 60 cycles. These measurements were less than the predicted ideal cooling but the observed reduction is explicable through the non-harmonic oscillator nature of the confining potential and other non-ideal factors. Our numerical modeling of the cooling technique indicates that with reasonable improvements to the experimental system increased cooling performance should be realizable.

We note there are several advantages to using the STOP cooling technique. Since photons are used efficiently in the cooling process, a minimal amount of power is required for the laser beams. This is beneficial for experiments cooling on transitions where laser light is difficult to produce. Light-assisted collision losses and reabsorption effects [80, 92, 107] that often limit laser cooling techniques were small for the amount of cooling obtained in STOP cooling. This is advantageous for experiments that begin with small initial numbers. Furthermore, the STOP cooling that we implemented is not the only way that this cooling scheme could be applied. Rather than resonant

scattering, stimulated Raman transitions could be used to slow the selected atoms and would be expected to have even higher efficiency.

Chapter 5

Intensity Pattern Formation in a Trapped Gas

The role of this chapter is to present our work [7] on light intensity pattern formations that can develop in elongated ultracold gases such as those used for our STOP cooling experiments described in chapter 4. A collection of ultracold atoms generally has an index of refraction that varies depending on the spatial density distribution of the gas. For many confined gases commonly found in ultracold atom experiments, there can be a substantial gradient in the spatial density distribution and hence the index of refraction. In addition, these gases can have a smaller spatial extent than that of the cross section of a laser beam that illuminates them. With a sufficient gradient in density under these conditions, the resulting index variation leads to frequency-dependent focusing or defocusing of incident near-resonant light as demonstrated by the calculations in this work. Non-intuitive intensity pattern formations result within the gas from the combination of refraction and diffraction of the incident light, including focusing effects that substantially increase the intensity of the light as compared to its incident value despite the nominally absorptive nature of the gas.

5.1 A Detour from STOP Cooling

During the set-up and optimization of the up-pump beam used for our experimental implementation of STOP cooling (see section 4.4), we varied the beam alignment, light intensity, length of time the beam illuminated the edge of the confined ultracold gas, and the laser frequency. These measurements were performed to ensure that we could generate a well-defined and reproducible fraction of up-pumped atoms at the edge of the gas for our STOP cooling experiments (see figure 4.1(a)). Changing each parameter resulted in a predictable change in the absorption imaging measurements (e.g. adjusting the beam alignment caused the fraction of up-pumped atoms to increase/decrease in the expected direction). That was until we began to vary the laser frequency. For those data sets where the laser frequency was the only variable, we encountered unexpected signals in our absorption imaging measurements. Specifically, we measured atoms in the bright state at

positions in the gas that did not have up-pump light directly illuminating the atoms. Figure 5.1 shows examples of these signals for various up-pump beam frequencies.

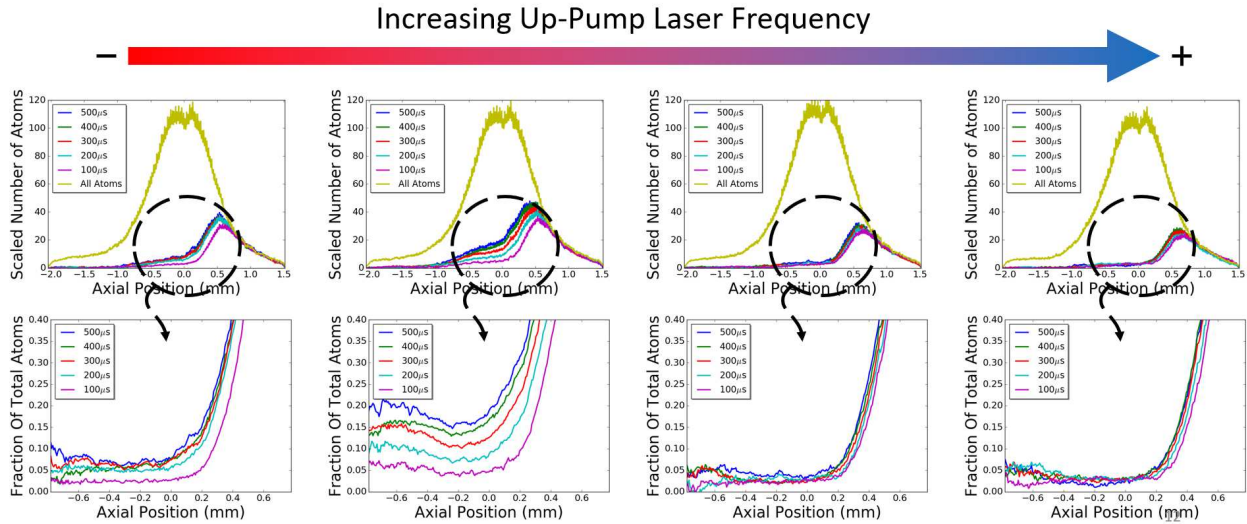


Figure 5.1: One-dimensional spatial density profiles of bright state atoms (top) and the corresponding fraction of bright state atoms along the axial direction of the confining potential (bottom). The yellow spatial density profiles are when the entire confined gas is optically pumped into the bright state. The other curves are when only the edge of the confined ultracold gas is optically pumped into the bright state. The length of time the up-pump beam is applied is shown in the inset legend. The frequency of the up-pump beam is below resonance (red-detuned) on the left and increases to above resonance (blue-detuned) on the right.

The one-dimensional spatial density distributions shown in figure 5.1 are data from absorption images represented in the binned format described in section 4.5. Each subfigure along the top of figure 5.1 shows a spatial profile when the entire confined ultracold gas is up-pumped into the bright state, along with separate spatial profiles when only the edge of the gas is up-pumped into the bright state. The data in each top subfigure corresponds to measurements performed using a different up-pump beam frequency. The up-pump beam was tuned to be either red or blue-detuned with respect to the $5S_{1/2} F = 1$ to $5P_{3/2} F = 2$ transition in ^{87}Rb (see figure 3.1). The up-pump pulse length applied to the edge of the gas ranged from 100 to 500 μs , but the applied pulse lengths were the same for all data sets. In addition, the alignment and intensity were the same for all data sets, too.

To further illustrate the frequency-dependent difference between the data sets, it is useful to divide the spatial profile of the up-pumped atoms by the spatial profile of the entire confined gas for each data set. This ratio is simply the number of bright state atoms as a function of position along the axial direction of the ultracold gas, and the results are shown in the subfigures along the bottom of figure 5.1. For red-detuned light, the resulting fractions show a clear non-zero signal corresponding to bright state atoms in the gas at positions where no up-pump light was directly illuminating the atoms. The frequency-dependence of this effect is apparent when looking at the blue-detuned data, where there are little to no bright state atoms at the same positions. It was these types of signals that motivated us to temporarily postpone our work on STOP cooling and investigate the underlying physics present in our system. The remainder of this chapter is dedicated to describing our efforts to quantify the effects of illuminating an elongated ultracold gas with near-resonant light.

5.2 Near-Resonant Light in Optically Thick Gases

A critical parameter in evaluating how light will propagate through a gas is the absorption length of light in that gas. The absorption length is inversely proportional to the density of atoms in the gas and the light absorption cross section, and it is not uncommon to have a system where the absorption length is much smaller than the spatial size of the system. This is true for ultracold atom experiments where it is possible to create gases in which the absorption length is smaller than the spatial extent of the gas in one or more dimensions [108–122]. This condition is most easily obtained when the light being considered is resonant or nearly-resonant with an atomic transition. In general, one would expect that in a gas where the absorption length is much smaller than the spatial extent of the gas along which the light propagates, the light would not be able to penetrate far into the gas and would attenuate quickly. However, in some ultracold atom experiments the atoms are trapped in an elongated confining potential where one spatial dimension is much larger than the other two (i.e. a so-called "cigar-shape") [25, 27, 51, 101, 120–122]. While the long axial direction of such a gas can be hundreds of absorption lengths in extent, the shorter radial direction

can be comparable to the absorption length. For light propagating along the long direction of the gas, if the light extends beyond the radial extent of the gas diffraction and refraction effects radically alter how far the light can penetrate into the gas. This can lead to non-intuitive intensity variations. A theoretical calculation of light propagation in these circumstances is the primary topic of this chapter.

The main question that we address in this chapter is the following: "For an optically thick elongated gas illuminated by a laser beam propagating along its elongated direction, what is the predicted maximum intensity of light near the center of the gas?" The answer that we derive for easily obtained experimental conditions is "up to an order of magnitude greater than the intensity of the original incident light." In other words, despite absorption lengths far shorter than the length of the trapped gas, rather than a decrease in peak intensity as the light propagates Maxwell's equations predict an increase and even large enhancement of the peak intensity for light with the appropriate near-resonant detuning. This applies to a range of atom densities near, but below, the density where atom-atom interactions would be expected to have significant influences on light propagation [123]. Understanding the intensity patterns of light in such gases is a necessary prerequisite for understanding either optomechanical forces or atom excitation (e.g. Rydberg atom excitation) resulting from such light.

The calculations that show this behavior are performed in a model system that consists of two-level atoms that are confined such that their density is described by a three-dimensional cylindrically symmetric Gaussian spatial density distribution with an axial rms size of $\sigma_z = 700 \mu\text{m}$ and a radial rms size of $\sigma_r = 20 \mu\text{m}$ along one of the radial directions (see figure 5.2). The confined gas is considered to be illuminated with a wide beam of near-resonant or resonant low-intensity light propagating in the elongated direction of the distribution. For these conditions, it is possible to determine the total optical depth (i.e. number of e^{-1} absorption lengths) along the elongated axis for a given laser detuning using the Beer-Lambert law, on-resonant cross section (taken to be equal to the unpolarized cross section $\lambda_0^2/(2\pi)$), and gas density. This is done by simply integrating the predicted amount of absorption based on the cross section and gas density as a function of the

distance along the center axis of the gas and translating that into an optical depth. The results of such a calculation are shown in figure 5.3.

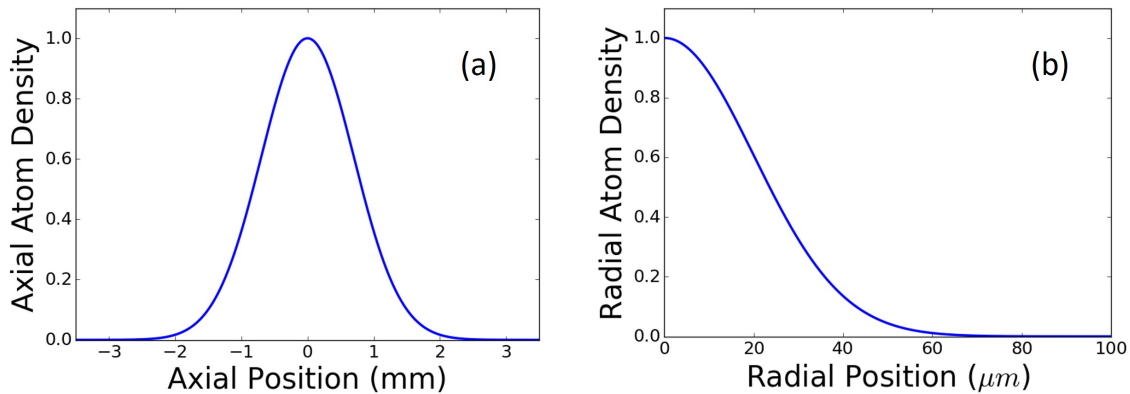


Figure 5.2: Normalized Gaussian spatial density distribution along the (a) axial direction and (b) radial directions. The horizontal axis for the axial distribution extends from $z = -5\sigma_z$ to $z = 5\sigma_z$. The horizontal axis for the radial distribution extends from $r = 0$ to $r = 5\sigma_r$. These plots were included to allow for ease of comparison between the density of atoms at a given position with the amount of light intensity predicted (shown in later figures) to be at that same position. Figure reproduced from [7].

Additionally, applying the Beer-Lambert law in the same way also yields a prediction for the intensity of light as a function of position along the elongated central axis of the gas. Figure 5.4 shows the result of such a calculation for two different peak densities in the density range of interest. As expected, the intensity of on-resonance light is quickly reduced to near-zero levels before reaching the center of the spatial density distribution. Detuning away from resonance allows for the light to penetrate further into the gas, but for moderate detunings the intensity reaching the opposite end of the gas is still only a fraction of the initial intensity.

In the remainder of this chapter, we go beyond such calculations and more carefully consider how near-resonant or resonant low-intensity light propagates in such a model system. Because the system has a monotonically decreasing density gradient away from the center of the gas in the radial and axial directions, there is a spatially dependent index of refraction in the medium. Depending on the frequency of the light, the incoming wave intensity is either focused (negative-detuned light) or defocused (positive-detuned light) by this index gradient. As a result of focusing, light intensity can be drawn from regions outside the trapped gas into the gas, increasing the light

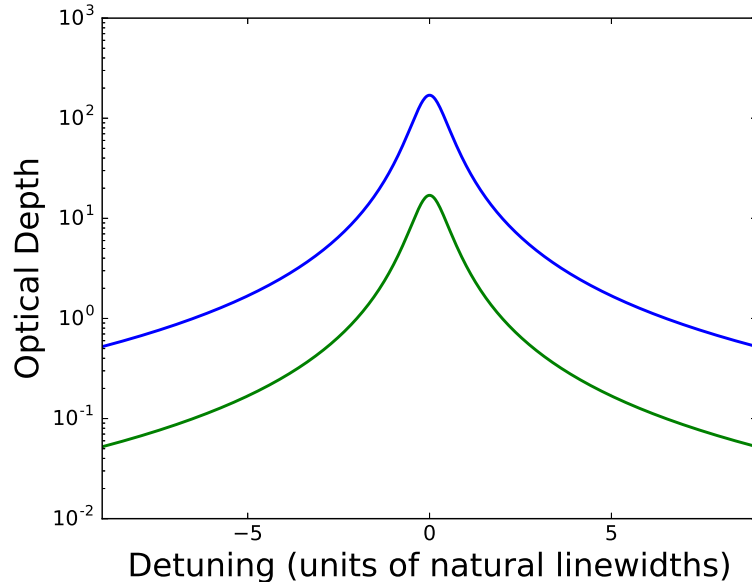


Figure 5.3: Beer-Lambert-law-based calculations of the optical depth (O.D.) along the long central axis of an elongated trapped ultracold gas. The variation in calculated O.D. with detuning is shown. The O.D. is determined by integrating along the axial length of the gas as described in the main text. The resonant wavelength is 780 nm. The green curve corresponds to a peak spatial density of 10^{11} cm^{-3} and the blue curve corresponds to a peak spatial density of 10^{12} cm^{-3} . Note that the vertical axis has a logarithmic scale. Figure reproduced from [7].

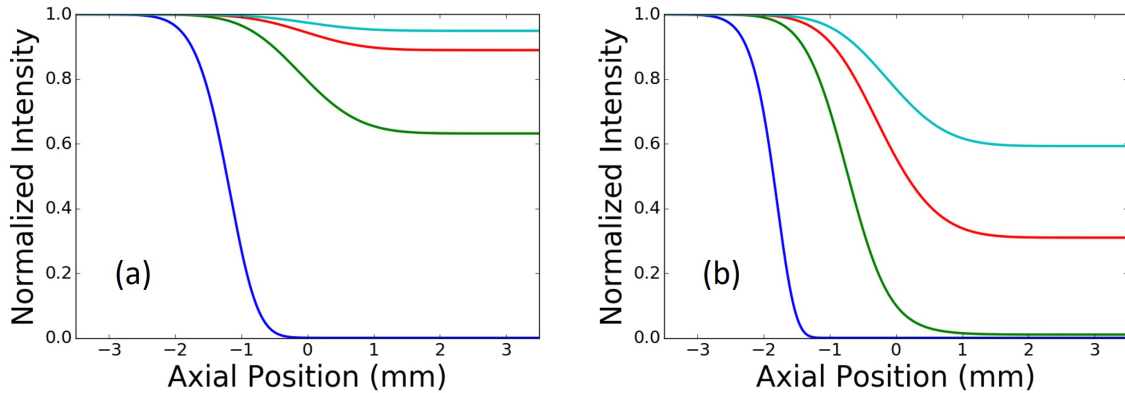


Figure 5.4: Beer-Lambert law predictions for the intensity of light propagating through the model system with a peak spatial density of (a) 10^{11} cm^{-3} and (b) 10^{12} cm^{-3} . The initial position is $z = -3.5 \text{ mm}$ (well outside of the volume with significant gas density). The blue curve is 0Γ detuning, green is $\pm 3\Gamma$, red is $\pm 6\Gamma$, and teal is $\pm 9\Gamma$, where Γ is the natural linewidth of the resonance transition. Figure reproduced from [7].

intensity in the trapped gas despite the fact that it is optically thick. The opposite can happen for light of opposite detuning with respect to resonance where it is defocused by the index gradient. Furthermore, the radial extent of the spatial density distribution is within about an order of magnitude in size of the wavelength of the propagating light. This introduces diffraction effects that also contribute to frequency-dependent intensity patterns in the trapped gas.

5.3 Envelope Wave Equation

This more careful consideration of the behavior of the light intensity as it propagates through a confined ultracold gas begins with Maxwell's equations and a wave solution that varies periodically in time as $e^{-i\omega t}$. This is often done in other treatments of light propagation in a physical situation exhibiting cylindrical symmetry [120, 124, 125]. As usual, the physical part of the wave in this treatment is given by the real part of the solution. The spatial part of the wave's electric field for a wave propagating in the elongated direction of the gas (the z -axis; see figure 5.5) is given as

$$E = E_0 \psi(x, y, z) e^{ik_0 z}, \quad (5.1)$$

where E_0 is the amplitude, $k_0 = \omega/c = 2\pi/\lambda_0$ where λ_0 is the vacuum wavelength, and $\psi(x, y, z)$ is the envelope of the wave. The envelope of the wave has unit magnitude for all positions during propagation through vacuum. The wave evolves away from uniformity when it encounters the (complex) index of refraction associated with the ultracold gas. The envelope is expected to vary slowly in the distance of a wavelength, allowing the use of the slowly varying envelope approximation [126] to write the following equation as a result of Maxwell's equations:

$$\frac{\partial \psi}{\partial z} = \frac{i}{2k_0} \nabla_{\perp}^2 \psi + \frac{ik_0}{2} (n^2 - 1) \psi, \quad (5.2)$$

where ∇_{\perp}^2 is the second-order spatial derivative in the transverse direction and n is the complex index of refraction. Replacing $(n^2 - 1)$ in (5.2) with the frequency dependent complex susceptibility for a two-level atom leads to a term associated with the index of refraction (real part) and the

absorption of light (imaginary part). The complex susceptibility for a two-level atom is expressed as [127]

$$\chi = -\frac{\sigma_0}{k_0} \rho(x, y, z) \frac{2\delta/\gamma - i}{1 + I/I_{sat} + 4 \left(\frac{\delta}{\gamma}\right)^2}, \quad (5.3)$$

where σ_0 is the unpolarized cross section, $\rho(x, y, z)$ is the spatial density distribution, and $I/I_{sat} \ll 1$. This more careful treatment allows us to account for the wave nature of the light as it propagates through an absorptive spatially anisotropic ultracold gas.

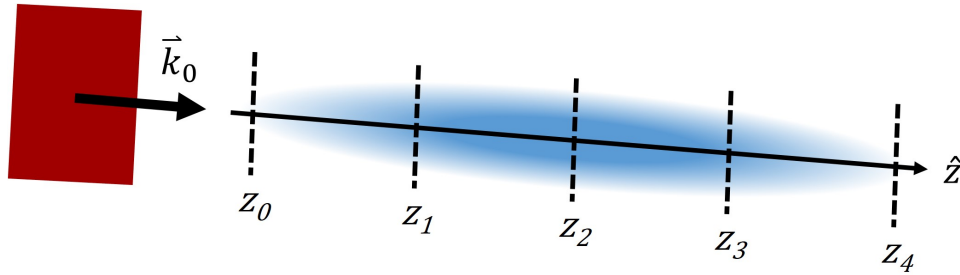


Figure 5.5: Schematic of a plane wave (red) encountering an ultracold gas (blue) of two-level atoms. The axial positions $z_0, z_1, z_2, z_3,$ and z_4 identify the locations of evenly spaced planes perpendicular to the light propagation direction in the spatial density distribution (see main text). Figure reproduced from [7].

5.3.1 Integration Method

To calculate results within this model, we use a variation of the Crank-Nicolson method with a fixed mesh grid in the radial ($r = \sqrt{x^2 + y^2}$) and axial directions to numerically integrate (5.2). We define $w_{k,m} \equiv \psi(k\Delta r, z_0 + m\Delta z)$, where the indices $k = 0, 1, 2, \dots, K$ and $m = 0, 1, 2, \dots, M$ are integers labeling a particular grid point. The discretized spatial coordinates are expressed as $r = k\Delta r$ and $z = z_0 + m\Delta z$, where $\Delta r, \Delta z$ are the grid point spacings in the radial and axial direction, respectively, and $z_0 = -5\sigma_z$. For the radial boundary conditions, we assume $\frac{\partial \psi}{\partial r} = 0$ at $r = 0$ and $r = K\Delta r$. For the axial boundary conditions, we assume a plane wave ($w_{k,0} = 1$ for all k) at $z = z_0$ and then propagate the wave in the positive z -direction.

The first step is to formulate (5.2) as an explicit difference equation (forward Euler method) and as an implicit difference equation (backward Euler method). The Crank-Nicolson method then uses $\frac{1}{2}$ the sum of the explicit and implicit difference equations to give the following expression:

$$\begin{aligned} \frac{w_{k,m+1} - w_{k,m}}{\Delta z} &= \frac{i}{4k_0} \frac{1}{\Delta r^2 k} \left[\left(k + \frac{1}{2}\right) w_{k+1,m} + \left(k - \frac{1}{2}\right) w_{k-1,m} - 2kw_{k,m} \right] \\ &+ \frac{i}{4k_0} \frac{1}{\Delta r^2 k} \left[\left(k + \frac{1}{2}\right) w_{k+1,m+1} + \left(k - \frac{1}{2}\right) w_{k-1,m+1} - 2kw_{k,m+1} \right] \\ &+ \frac{ik_0}{4} (\chi_{k,m} w_{k,m} + \chi_{k,m+1} w_{k,m+1}), \end{aligned} \quad (5.4)$$

where $\chi_{k,m} \equiv \chi(k\Delta r, z_0 + m\Delta z)$ and the $\frac{1}{2}$ factors make the spatial derivative work out in cylindrical coordinates to second order in an expansion of ψ . Collecting like-terms in (5.4) leads to

$$\begin{aligned} &\left(\frac{1}{\Delta z} + \frac{i}{2k_0} \frac{1}{\Delta r^2} - \frac{ik_0}{4} \chi_{k,m+1} \right) w_{k,m+1} - \frac{i}{4k_0} \frac{1}{\Delta r^2} \left(1 + \frac{1}{2k} \right) w_{k+1,m+1} \\ &- \frac{i}{4k_0} \frac{1}{\Delta r^2} \left(1 - \frac{1}{2k} \right) w_{k-1,m+1} \\ &= \\ &\left(\frac{1}{\Delta z} - \frac{i}{2k_0} \frac{1}{\Delta r^2} + \frac{ik_0}{4} \chi_{k,m} \right) w_{k,m} + \frac{i}{4k_0} \frac{1}{\Delta r^2} \left(1 + \frac{1}{2k} \right) w_{k+1,m} \\ &+ \frac{i}{4k_0} \frac{1}{\Delta r^2} \left(1 - \frac{1}{2k} \right) w_{k-1,m}. \end{aligned} \quad (5.5)$$

Next, the boundary condition at $r = K\Delta r$ means $w_{K+1} = w_{K,m}$, so from (5.5) we get another equation expressed as

$$\begin{aligned}
& \left(\frac{1}{\Delta z} + \frac{i}{4k_0} \frac{1}{\Delta r^2} \left(1 - \frac{1}{2K} \right) - \frac{ik_0}{4} \chi_{K,m+1} \right) w_{K,m+1} \\
& - \frac{i}{4k_0} \frac{1}{\Delta r^2} \left(1 - \frac{1}{2K} \right) w_{K-1,m+1} \\
= & \\
& \left(\frac{1}{\Delta z} - \frac{i}{4k_0} \frac{1}{\Delta r^2} \left(1 - \frac{1}{2K} \right) + \frac{ik_0}{4} \chi_{K,m} \right) w_{K,m} \\
& + \frac{i}{4k_0} \frac{1}{\Delta r^2} \left(1 - \frac{1}{2K} \right) w_{K-1,m}. \tag{5.6}
\end{aligned}$$

Lastly, at $r = 0$, cylindrical symmetry leads to another difference equation that can be expressed as

$$\begin{aligned}
& \left(\frac{1}{\Delta z} + \frac{i}{k_0} \frac{1}{\Delta r^2} - \frac{ik_0}{4} \chi_{0,m+1} \right) w_{0,m+1} - \frac{i}{k_0} \frac{1}{\Delta r^2} w_{1,m+1} \\
= & \\
& \left(\frac{1}{\Delta z} - \frac{i}{k_0} \frac{1}{\Delta r^2} + \frac{ik_0}{4} \chi_{0,m} \right) w_{0,m} + \frac{i}{k_0} \frac{1}{\Delta r^2} w_{1,m}. \tag{5.7}
\end{aligned}$$

With known values for $w_{k,m}$, the primary task is to calculate the values for $w_{k,m+1}$. To do so, (5.5) is solved for the interior grid points, (5.6) is solved for the $r = K\Delta r$ grid points, and (5.7) is solved for the $r = 0$ grid points. In each case (i.e. interior and boundaries), the corresponding linear system of equations can be expressed using a tridiagonal matrix representation, and so can be solved efficiently using a tridiagonal matrix algorithm (e.g. Thomas algorithm). Solving the three systems of equations results in the solution advancing by Δz in the positive z -direction, and a new set of equations are generated until the solution reaches $z = z_0 + M\Delta z$. The normalized intensity of the wave at any grid point can be determined by $|w_{k,m}|^2$.

5.3.2 Calculation Parameters

The axial and radial spatial parameters relevant to the spatial density distribution are set to be similar to those found in experiments where ultracold atoms are confined in an elongated optical

trap. Convergence tests are performed on the number of mesh grid points and the spacing between grid points. For the predictions presented in the following sections, we use 1251 radial grid points with a spacing of $\Delta r = 320$ nm and 5001 axial grid points with a spacing of $\Delta z = 1.4$ μm . Calculations that result in intensity features extending beyond 3.5 mm in the axial direction have additional axial grid points included. The partial differential equation is then integrated to obtain solutions for the envelope of the wave under various spatial density and frequency detuning conditions.

As detailed in section 5.2, we model the spatial density distribution as a three-dimensional Gaussian distribution with an elongated axis in the axial direction (aspect ratio = 35). The radial grid size is large enough to ensure $\frac{\partial \psi}{\partial r}$ is well-approximated by 0 at the radial boundary for all axial positions, which is a reasonable approximation. We set the direction of the incident wave vector to be colinear with the axial direction of the spatial density distribution, and set the initial plane wave to be at an axial position where the atom density is negligible ($z_0 = -5\sigma_z$). The calculations are performed with peak spatial densities of 10^{11} cm^{-3} and 10^{12} cm^{-3} . Working in units of natural linewidths, $\Gamma = (2\pi\tau)^{-1}$ (where τ is the excited state lifetime), we vary the frequency detuning over an interval spanning nearly an order of magnitude above and below the resonance frequency.

5.4 Calculation Results

The results of the simulation were very different from the Beer-Lambert law predictions (see figure 5.3 and figure 5.4). For instance, the expectation from those predictions is that practically no light will make it across the length along the center axis of the gas for a wide range of parameters. Instead, for negative-detuned frequencies the penetration of the light along the axis can easily be such that it increases and actually forms intensity peaks past the center position of the spatial density distribution. For positive-detuned frequencies, the intensity of the light along the axial direction can often be attenuated far more than predicted by the calculation using the Beer-Lambert law. Moreover, examining radial distributions of light intensity in planes along the light propagation direction show the formation of light intensity patterns reminiscent of Airy patterns.

5.4.1 Elongated-Axis Intensity Profiles

Figure 5.6 shows the intensity along the axial direction at the radial center of the spatial density distribution when a plane wave is propagated through the model system. The negative-detuned light experiences very little attenuation, and after the peak of the spatial density distribution the light intensity begins to increase. Most notably, for the 10^{12} cm^{-3} peak spatial density and -6Γ frequency detuning the intensity maximum is more than 12 times the initial intensity. This is approximately 40 times larger than what would be expected at that same position given the Beer-Lambert law prediction. The on-resonance light has the same axial intensity behavior as the Beer-Lambert law case until the end of the spatial density distribution, where the light undergoes a "recovery" of intensity owing to the influence of diffraction. For the positive-detuned frequencies, the intensity falls off more rapidly than in the Beer-Lambert law prediction. For the 10^{12} cm^{-3} peak spatial density and $+6\Gamma$ frequency detuning, the intensity is nearly 70 times less than what the Beer-Lambert law predicts at the final axial position ($z = 3.5 \text{ mm}$).

5.4.2 Pattern Formation in Radial Directions

Examples of radial intensity patterns that form in planes perpendicular to the light propagation direction are shown in figure 5.7. The positions of the planes represented in the corresponding subfigures are evenly spaced as illustrated by planes $z_{1,\dots,4}$ in figure 5.5. For visual comparison, all of the subfigures are plotted using the same false-color scale. In the case of -6Γ frequency detuning, this scale results in heavy saturation of the intensity values, but serves to demonstrate the large increase in expected intensity in downstream planes. Alternatively, the intensity can be visualized in a plane that cuts through the atom distribution such that the $r = 0$ axis is included in the plane. Such a representation is shown in figure 5.8. Figure 5.9 shows the radial distribution of light intensity at several axial positions under the -6Γ detuning condition.

We have examined the intensity patterns represented in figures 5.6, 5.7, 5.8 and 5.9 over a wider range of density and detuning parameters, too. The relevant features (e.g. the peak intensity) change smoothly as parameters are varied. At peak densities much smaller than 10^{11} cm^{-3} there is

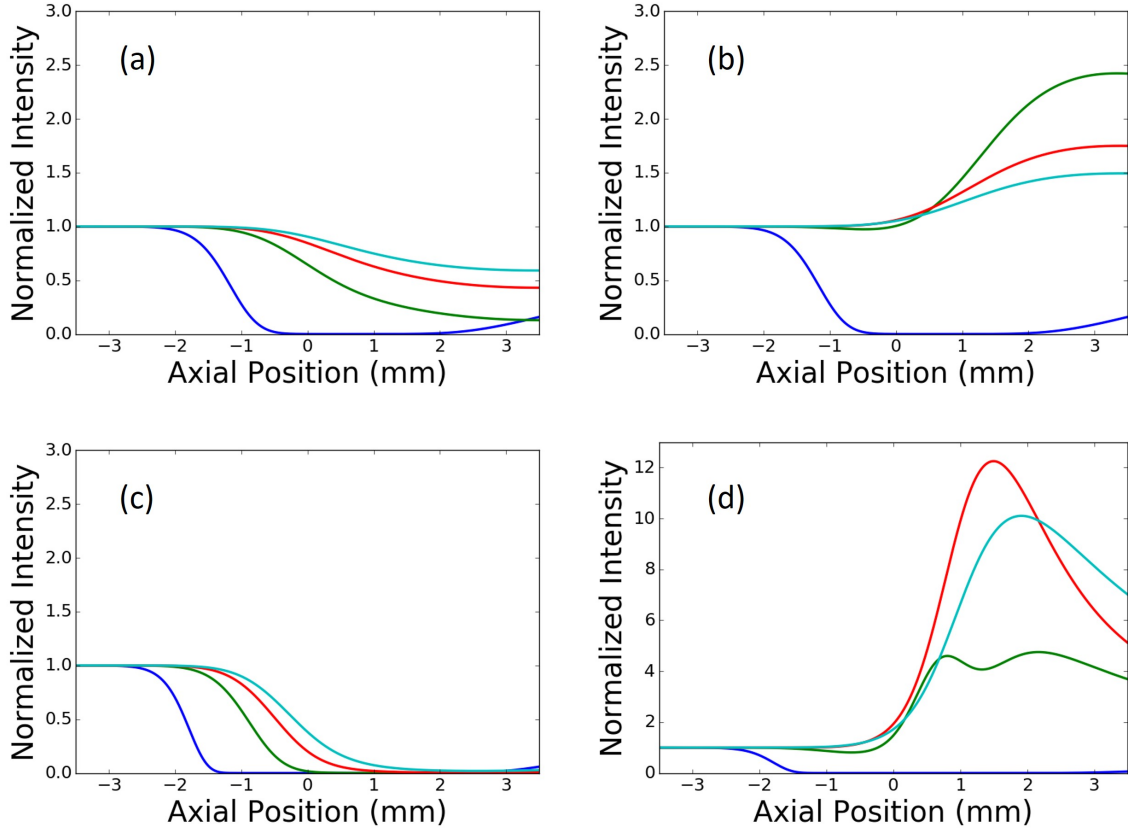


Figure 5.6: Wave propagation model predictions for the intensity along the elongated axis of the spatial density distribution. The plots (a) and (b) both have a peak spatial density of 10^{11} cm^{-3} . The plots (c) and (d) both have a peak spatial density of 10^{12} cm^{-3} . The blue curve for all four plots is 0Γ detuning. For (a) and (c) the green curve is $+3\Gamma$, red is $+6\Gamma$, and teal is $+9\Gamma$. For (b) and (d) the green curve is -3Γ , red is -6Γ , and teal is -9Γ . Note that the vertical axis scale for (a)-(c) is different than the vertical axis scale for (d). Figure reproduced from [7].

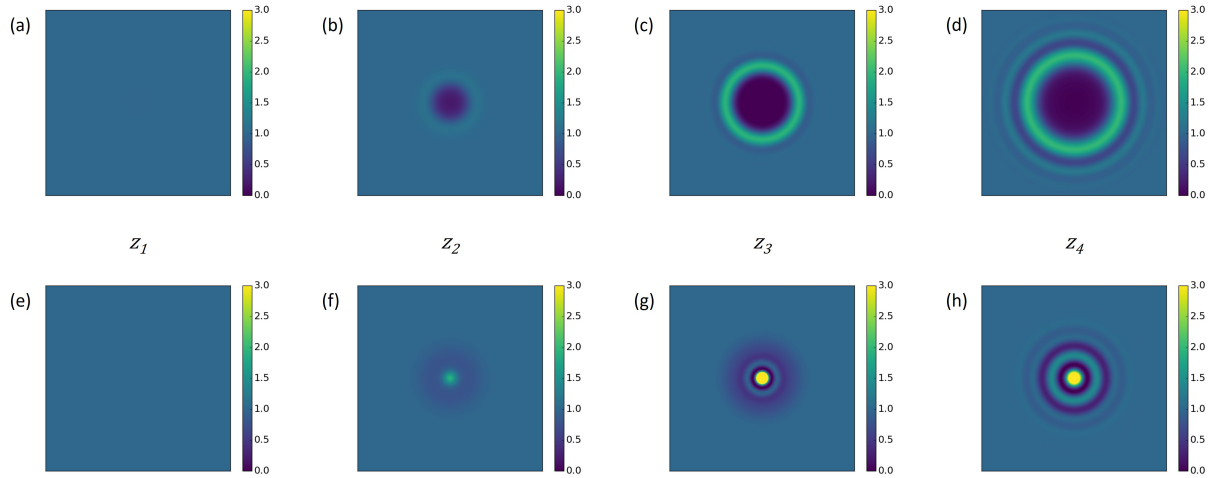


Figure 5.7: Intensity patterns located at evenly-spaced planes perpendicular to the axis of propagation for a peak spatial density of 10^{12} cm^{-3} . (a)-(d) correspond to a frequency detuning of $+6\Gamma$ and (e)-(h) correspond to a frequency detuning of -6Γ . The planes are located at $z_1 = -1.75 \text{ mm}$, $z_2 = 0$, $z_3 = 1.75 \text{ mm}$, and $z_4 = 3.5 \text{ mm}$. The horizontal and vertical widths are equal to $16\sigma_r$ for all of the subfigures. Figure reproduced from [7].

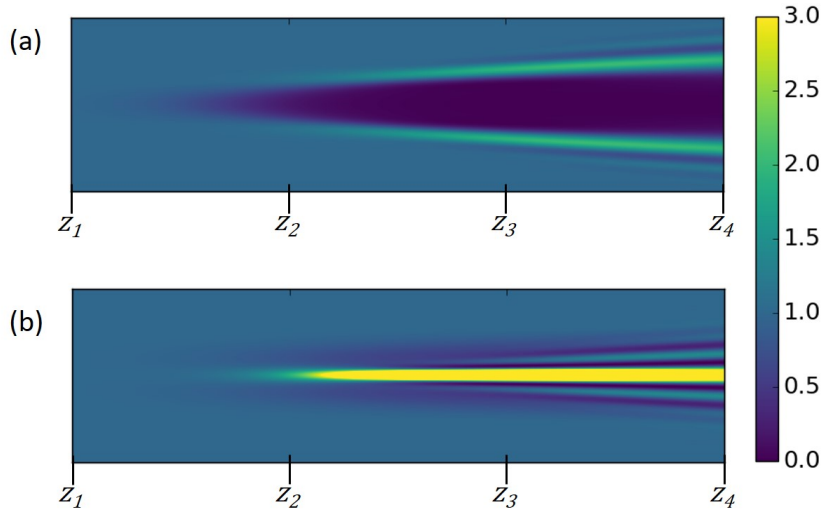


Figure 5.8: Intensity patterns formed in a plane that intersects the central elongated axis of the spatial density distribution for a peak spatial density of 10^{12} cm^{-3} . (a) corresponds to a frequency detuning of $+6\Gamma$ and (b) corresponds to a frequency detuning of -6Γ . The horizontal axes are parallel to the axis of propagation and the tick marks are located at $z_1 = -1.75 \text{ mm}$, $z_2 = 0$, $z_3 = 1.75 \text{ mm}$, and $z_4 = 3.5 \text{ mm}$. The vertical width is equal to $16\sigma_r$ (aspect ratio not to scale) and the center of the vertical axis is $r = 0$ for both subfigures. Figure reproduced from [7].

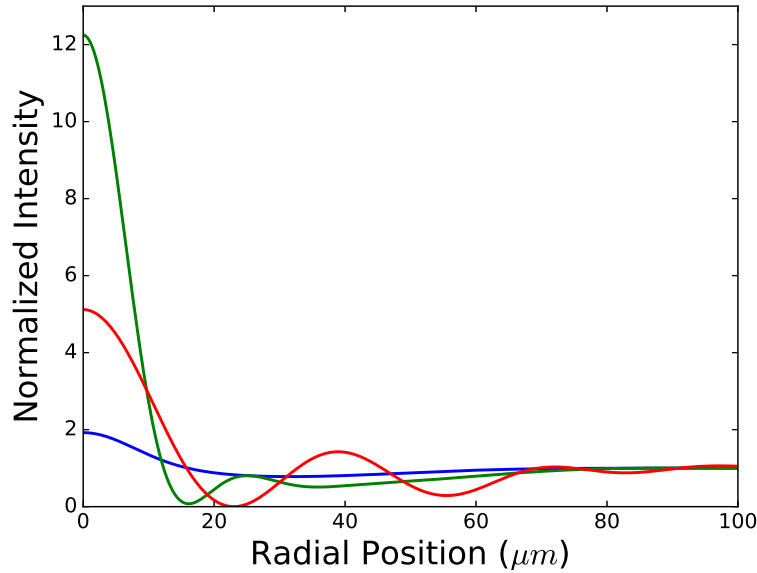


Figure 5.9: Radial plot of intensity patterns formed during propagation through the model system with a peak spatial density of 10^{12} cm^{-3} . The horizontal axis extends out to $5\sigma_r$, where $r = 0$ lies on the elongated central axis of the gas. The peak spatial density is 10^{12} cm^{-3} and the frequency detuning is -6Γ . The blue curve corresponds to the radial intensity at $z = 0$, the green curve corresponds to $z = 1.498 \text{ mm}$, and the red curve corresponds to $z = 3.5 \text{ mm}$. Figure reproduced from [7].

hardly a noticeable effect as compared to the Beer-Lambert law either along the central radial axis or in radial intensity patterns. As the density is increased, patterns emerge along the lines described in the examples shown above and become more and more pronounced. This continues past 10^{12} cm^{-3} , but at that point approximations that we made to obtain (5.2) are starting to break down, and in addition the physics of atom-atom interactions (e.g. dipole coupling [123,128]) would start to be expected to play a role and that is not included in this model. We don't expect that such additional considerations would make the general behavior presented here to become ignorable. The effects would still be there – they would just be harder to model accurately.

Additionally, we have also examined the influence of the radial extent of the spatial density distribution on the formation of the intensity peak along the central axis of the gas. Using a peak spatial density of 10^{12} cm^{-3} and frequency detuning of -6Γ , we varied the radial rms size from $10 \mu\text{m}$ to $40 \mu\text{m}$ while keeping the axial rms size fixed. A large enhancement of the initial intensity occurs over the entire range of radial sizes, and the axial position of the intensity peak shifts further

away from the center of the gas when the radial extent increases. For the smallest radial size tested ($10 \mu\text{m}$), the maximum intensity is less than the peak in figure 5.6(d), but only by approximately 20%. As the radial extent increases, the resultant maximum intensity becomes larger, reaching several percent higher than the peak in figure 5.6(d), until turning over near the end of the range of radial sizes tested.

Beyond varying the radial extent, we also increased the propagation distance from $z = 5\sigma_z$ out to $z = 30\sigma_z$ to examine the "recovery" feature for on-resonance light shown in figure 5.6. At $z = 30\sigma_z$, the intensity along the axis of propagation is approximately 80% of the originally incident value for a peak spatial density of 10^{12} cm^{-3} . Performing the same calculation using a peak spatial density of 10^{11} cm^{-3} results in a "recovery" to more than 90% of the incident value, with a curve that is trending smoothly toward unity. We note that while the on-axis intensity tends toward the value of the incident intensity infinitely far from the gas, the total power in the forward direction is reduced.

5.4.3 Total Scattered Power

While it is evident that the Beer-Lambert law and wave propagation model produce different predictions for the light intensity, it is also reasonable to consider whether these two treatments are in agreement with regard to the total power of the light propagating through the system. Total power as a function of position is the light intensity integrated over a plane perpendicular to the elongated axis as a function of the position of that plane along the axis. The radial extent of the plane is taken to be well beyond the radial extent of the gas. As a plane wave propagates through the model system, the total power as a function of axial position will decrease monotonically along the propagation direction. This is due to light being scattered by the atoms, which causes the power reaching subsequent axial planes in the forward direction to continually decrease. Figure 5.10 shows normalized results for the amount of power scattered out of an incident plane wave as it propagates through the model system. The -6Γ detuning results in more power being scattered because of the light intensity being drawn from outside of the trapped gas into the gas causing an

increase in the total power scattered. Similar considerations explain the lower amount of scattered light in the $+6\Gamma$ case.

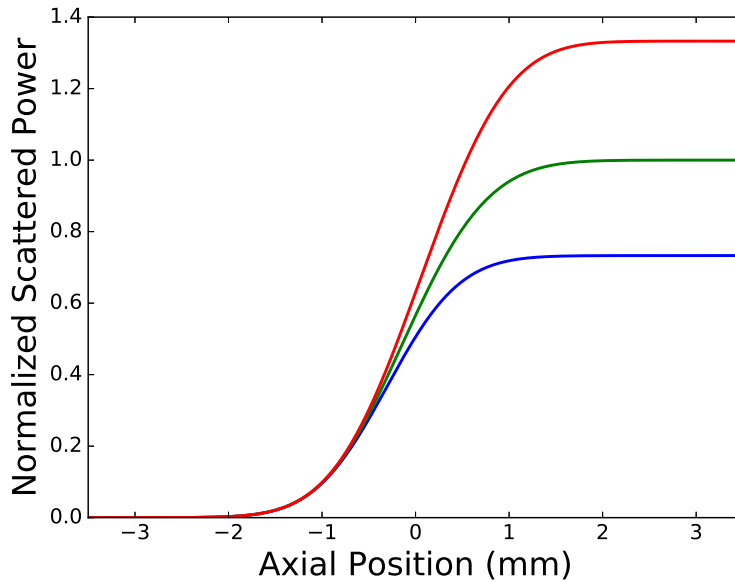


Figure 5.10: Normalized scattered power as a plane wave propagates through the model system with a peak spatial density of 10^{12} cm^{-3} . The blue curve is $+6\Gamma$ and red is -6Γ . The green curve is the prediction from the Beer-Lambert law for $\pm 6\Gamma$. Figure reproduced from [7].

5.5 Intensity Pattern Formation Conclusions

Comparing the Beer-Lambert law predictions to Maxwell’s equations-based predictions for sets of easily achieved ultracold atom parameters demonstrates a clear difference in regard to the behavior of intensity as near-resonant or resonant low-intensity light propagates through the medium. Given the index gradients are not that different from the light wavelength it is not so surprising that refraction and diffraction produce significant effects. Even so, the magnitude of these effects are so large that even for what would be expected to be a highly optically thick and absorptive gas, the on-axis light intensity doesn’t just fail to decrease for some parameters. Rather, the light intensity increases to more than an order of magnitude greater than its initial value. This shows that the considerations listed here would need to be taken into account in any estimation or determination

of the light intensity distribution in similar situations if even only a mildly accurate picture of the resulting intensity pattern of light is of interest.

Simply put, in ultracold atom systems with significant index of refraction spatial variations, the application of the Beer-Lambert law fails spectacularly in regard to the prediction of near-resonant or resonant low-intensity light propagating in a sample. In such cases, the central on-axis light intensity can be well more than an order of magnitude larger (smaller) than expected for negative (positive) detuned light. And, for regions of space surrounding the ultracold atom spatial density distribution, significant radially-varying intensity patterns can form too. The existence of such non-intuitive behavior would be an important consideration in experiments, for instance in those studying optomechanical effects in ultracold atomic gases [119, 121, 129, 130].

5.5.1 Difficulties with Comparing to Data

The experimental signals described in section 5.1 alluded to light propagation physics associated with near-resonant light in our ultracold gas. Those measurements provided qualitative evidence that motivated us to carefully consider near-resonant light propagation using a model system. However, a direct comparison between model predictions and data could not be performed. The signal-to-noise capabilities of the experimental measurements required illuminating the atoms with up-pump light over timescales that were much longer than would be required to observe the intensity formations predicted by the numerical model. Specifically, the timescales were longer than the atom motion in radial directions and comparable to the atom motion in the axial direction. A comparison to experimental light patterns would have required including atom motion and a precise representation of the optical trap in the numerical model. While technically feasible, the degree of optical trap characterization necessary was beyond our capabilities at the time. Furthermore, a comparison to those measurements (see section 5.1) is complicated by the fact that it is not the light intensity patterns that are experimentally detected, but rather the integrated number of atoms that have been optically pumped into the bright state. While the fraction of bright state

atoms is related to the light intensity in the gas, the absorption imaging technique used for those measurements does not allow for discerning the spatial intensity patterns predicted.

Chapter 6

Faraday Rotation at Atomic Lifetime Timescale

This chapter is dedicated to presenting the theoretical description and experimental measurements of the time-dependent development of Faraday rotation in an ultracold gas over timescales on the order of an atomic excited state lifetime [8]. When a gas of ultracold atoms is suddenly illuminated by light that is nearly resonant with an atomic transition, the atoms cannot respond instantaneously. This non-instantaneous response means the gas is initially more transparent to the applied light than in steady-state. The timescale associated with the development of light absorption is set by the atomic excited state lifetime. Similarly, the index of refraction in the gas also requires time to reach a steady-state value, but the development of the associated phase response is expected to be slower than absorption effects. Faraday rotation is one manifestation of differing indices of refraction for orthogonal circular light polarization components. We have performed experiments measuring the time-dependent development of polarization rotation in an ultracold gas subjected to a magnetic field. Our measurements match theoretical predictions based on solving optical Bloch equations. We are able to identify how parameters such as steady-state optical thickness and applied magnetic field strength influence the development of Faraday rotation.

The following sections of this chapter will provide a description of the theoretical modeling of our system along with results based on experimental measurements. The description will include the theory used to model the time-dependent evolution of light in an ultracold gas, predictions of the transmitted intensity through an ultracold gas representative of those used in our experiments, and our experimental measurements of the time-dependent development of Faraday rotation. Parameters that influence the response timescales in the system will be discussed. The work presented will highlight important considerations when dealing with near-resonant light that is suddenly applied to an optically thick ultracold gas.

6.1 Near-Resonant Light and Atoms

Extensive theoretical and experimental research has been performed studying near-resonant light interacting with ultracold atomic gases, ranging from dilute (e.g. low spatial number density) [114, 131] to high density ensembles [132–134]. A description using coupled dipoles adequately captures physics in a low density gas [135, 136]. Accurate predictions for light in high density gases, where atom-atom interactions become relevant, are also being pursued [137, 138]. Identifying subtleties linked to the physics in these systems is ongoing. For instance, recent theoretical calculations indicate that transitioning from a scalar description to one that includes the vector nature of light (i.e. polarization) can significantly alter predictions of phenomena such as Anderson localization of light [139, 140]. While fundamental studies of light and its interactions with matter date back centuries, it is clear there are still open questions highlighted by discrepancies between current theoretical models and experimental results [141]. The important role resonant light plays in a wide variety of fields, including quantum simulation [142], precision spectroscopy [143], optical clocks [144], and ultracold plasmas [145] to name a few, encourages the continued study of near-resonant light interactions. In this article, we examine how a phase-associated effect, Faraday rotation, develops in concert with absorption as atoms in a dilute ultracold gas transition from a state of being transparent to being optically thick.

The characteristic response time of a gas of atoms to light that is near-resonant or resonant with a particular transition is determined by the atomic excited state lifetime of that transition. One implication of this is that if near-resonant or resonant light is suddenly applied to a gas of atoms, the gas will be effectively transparent until the atoms have enough time to develop an appreciable dipole response to the light. This has been demonstrated theoretically and experimentally, for example, in measurements of optical precursors [146], optical free induction decay [147], and related effects [148]. However, these measurements have focused on absorption effects. The atom gas can also shift the phase of incident light (i.e. have a real component of an index of refraction), but similar to absorption, cannot do so instantaneously. Since the phase response

is non-instantaneous, related polarization effects such as Faraday rotation will also take time to develop.

At first glance, the timescale for the phase shifts that underly the phase effects might be expected to be approximately twice as long as for absorption effects since the phase effects manifest themselves linearly with the electric field while absorption effects are observed via light intensity (proportional to the electric field squared). Through the work presented in this article, we find that the associated physics in a realistic system is more complicated than a straightforward ratio of two relationship. We have conducted experiments measuring the time development of Faraday rotation in an optically thick ultracold gas and then compared those experimental results with theoretical predictions. Aside from investigating the associated basic physics, these considerations are relevant if sufficiently short pulses are used in situations where phase shifts are important, as can be the case in cavity QED [149] and interacting Rydberg gases [150].

6.1.1 Implementation Overview

Our experiments consisted of suddenly turning on a resonant linearly polarized laser beam through a gas of ultracold atoms in a magnetic field and monitoring the intensity and polarization of the transmitted light as a function of time. After a sufficiently long period of time, the system reaches quasi-steady state. We refer to this as a quasi-steady state because there is a period in time where the light transmission stops changing rapidly with time, but there is then a slow optical pumping that works to bring the gas to a true steady-state over a longer timescale. Along with a significant absorption of the light determined in part by the atom density, there is a modification of the ellipticity and direction of the light polarization. The latter effect can be understood as being due to different values of the real part of the index of refraction of the right-handed and left-handed circular polarization components of the incident light. By measuring the development of the intensity and polarization of the light as a function of time, the time-dependent absorption and phase shifts of the light in the gas can be characterized and compared to theoretical expectations. Our experimental data is in good agreement with calculations based on optical Bloch equations.

6.2 Treatment of Dipole Response

We use Maxwell's equations and a set of optical Bloch equations based on our experimental conditions to calculate the time-dependent transmitted light intensity and polarization. The spatial extent of the gas as compared to the beam size and wavelength of the incident light is such that diffraction effects are negligible and thus not included in this treatment. One advantage of this is that we can model the gas as having a uniform spatial density of atoms rather than having to model the density variations that exist in the actual experiment. We also ignore the finite speed of light with regard to the propagation of light intensity changes through the ultracold gas, which is a reasonable approximation for our conditions.

To model our experimental measurements, we use parameters appropriate to the D2 line for ^{85}Rb (shown in figure 6.1(a)) for light that is nearly resonant on the $F = 3$ to $F = 4$ cycling transition. The incident light is linearly polarized and propagates along the direction of an applied magnetic field, so it is natural to consider the light as being composed of equal parts σ^+ and σ^- circular polarization components. The applied magnetic field produces Zeeman shifts across the magnetic sublevels which causes the σ^+ and σ^- polarization components to become frequency detuned by different amounts for transitions that share the same ground state magnetic sublevel (see figure 6.1(b)). Accounting for the range of induced detunings along with the atoms' relative transition strengths in the calculation captures both the absorption and the phase shift associated with the σ^+ and σ^- polarization components. If the response of the multi-level atoms subjected to the magnetic field leads to a differential phase shift between the polarization components then the result will be a polarization rotation of the light.

6.2.1 The Polarization Components

Our theoretical treatment begins with a linearly polarized plane wave propagating in the \hat{z} -direction. The plane wave, $\vec{E}(z, t)$, is incident on a gas of effectively stationary atoms, where z is the spatial coordinate and t is time. There is assumed to be no spatial variation in the directions

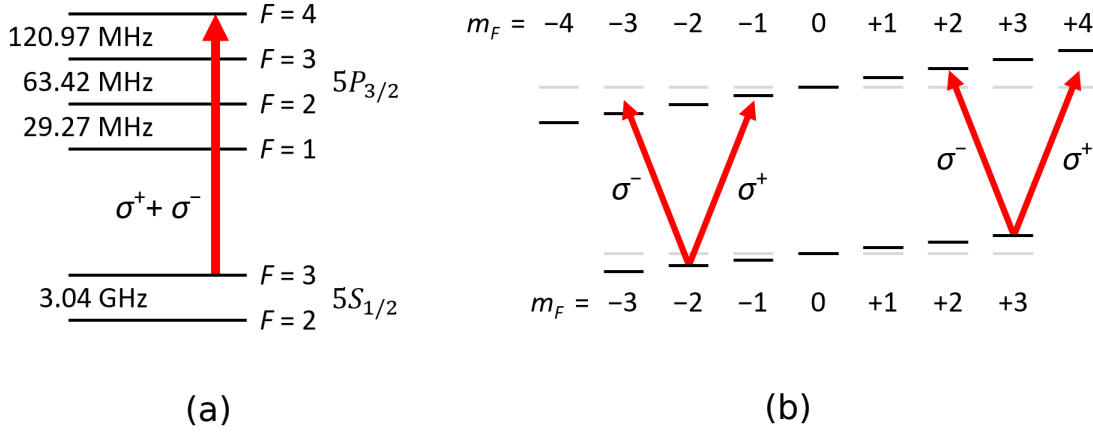


Figure 6.1: Relevant energy levels for our theoretical calculations and experimental measurements of the time-dependent Faraday rotation of light in an ultracold gas. The incident light is composed of equal parts σ^+ and σ^- circular polarization and is represented by the red arrow(s). Part (a) shows the hyperfine structure in the D2 (780 nm) line in ^{85}Rb (the ground state [1] and excited state [3] splittings are not to scale). Polarized light is driving the $5S_{1/2} F = 3$ to $5P_{3/2} F = 4$ cycling transition. Part (b) depicts the magnetic sublevels in the $5S_{1/2} F = 3$ ground state and $5P_{3/2} F = 4$ excited state. The gray lines represent the degenerate (no magnetic field) magnetic sublevels and the black lines represent the Zeeman-shifted sublevels. Two examples of the σ^+ and σ^- polarization components are shown with different amounts of detuning resulting from the energy shifts. Figure reproduced from [8].

perpendicular to the direction of propagation. Starting with Maxwell's equations and the plane wave assumption leads to the wave equation

$$\frac{\partial^2 \vec{E}(z, t)}{\partial z^2} = \mu_0 \frac{\partial^2 \vec{D}(z, t)}{\partial t^2}, \quad (6.1)$$

where $\vec{D}(z, t) = \epsilon_0 \vec{E}(z, t) + \vec{P}(z, t)$, μ_0 is the vacuum permeability, ϵ_0 is the vacuum permittivity and $\vec{P}(z, t)$ is the polarization response of the ultracold gas. The plane wave solution is expressed as

$$\vec{E}(z, t) = \tilde{E}_+(z, t) \hat{\sigma}_+ + \tilde{E}_-(z, t) \hat{\sigma}_-, \quad (6.2)$$

$$\tilde{E}_{\pm}(z, t) = \tilde{A}_{\pm}(z, t) e^{(ik_0 z - i\omega t)}, \quad (6.3)$$

where $\hat{\sigma}_+$ and $\hat{\sigma}_-$ are circular basis unit vectors and the \pm subscript corresponds to the σ^+ and σ^- circular polarization components, respectively. $\tilde{A}_\pm(z, t)$ are the polarization amplitude and phase components of the wave, k_0 is the vacuum wave number, and ω is the optical frequency. The relative phase between the σ^+ and σ^- polarization components of the incident light is initially set to be zero. The atoms' polarization response is expressed as

$$\vec{P}(z, t) = \tilde{P}_+(z, t)\hat{\sigma}_+ + \tilde{P}_-(z, t)\hat{\sigma}_-, \quad (6.4)$$

$$\tilde{P}_\pm(z, t) = \frac{\epsilon_0}{k_0} \tilde{\beta}_\pm(z, t) e^{(ik_0z - i\omega t)}, \quad (6.5)$$

where $\tilde{\beta}_\pm(z, t)$ are complex amplitudes corresponding to the σ^+ and σ^- polarization component dipole responses of the atoms. Steady-state treatments generally express the atoms' polarization response as $\vec{P} = \epsilon_0 \chi \vec{E}$, where the susceptibility, χ , is a constant. This is correct once the system has reached steady-state, but it is not an applicable expression for our calculations since we are interested in what happens in the system while the atoms' polarization response is still developing with time.

To calculate the effect these dynamics have on the light in the gas, we derive an envelope equation by inserting (6.2) and (6.4) into (6.1). We apply the slowly-varying-envelope-approximation and $\frac{\partial \tilde{P}_\pm}{\partial t} \ll \omega \tilde{P}_\pm$, which leads to

$$\frac{\partial \tilde{A}_\pm(z, t)}{\partial z} = \frac{i}{2} \tilde{\beta}_\pm(z, t). \quad (6.6)$$

A key feature of (6.6) is that it captures the time-dependent evolution of the atoms' dipole responses across the \hat{z} -direction spatial extent of the gas. To better appreciate the importance of including the spatial extent in the calculation, it is useful to first examine the evolution of near-resonant light interacting with an optically thin gas of atoms in a simplified system as compared to the real ^{85}Rb states.

6.2.2 Atomic Dipole Response

A simple $F = 0$ to $F = 1$ transition can be used to examine the relevant general physics of driving an optically thin gas with light composed of equal parts σ^+ and σ^- polarization components. An applied magnetic field induces Zeeman shifts in the excited state magnetic sublevels that causes the incident light polarization components to become detuned by an equal and opposite amount with magnitude $|\delta|$ from the zero magnetic field transition resonance (where the sign of the detuning depends on the magnetic field direction and magnetic sublevel quantum number). The optical Bloch equation for the dipole coherence of the $\Delta m_F = +1$ ground-excited state transition in a rotating frame can be expressed as

$$\dot{\rho}_{1,2} = -(i\delta + \gamma/2)\rho_{1,2} + iA'_+(\rho_{1,1} - \rho_{2,2}), \quad (6.7)$$

where the subscripts 1 and 2 denote the $m_F = 0$ ground state and $m_F = +1$ excited state magnetic sublevels, respectively. γ is the damping rate (i.e. inverse excited state lifetime of the transition), and A'_+ corresponds to the σ^+ polarization component of the incident light. The light is assumed to have an instantaneous turn-on and is assumed to be very low-intensity ($A'_+ \ll \gamma$) so that the excited state population remains ignorable. Given the initial condition, $\rho_{1,2} = 0$ at $t = 0$, an analytic solution for (6.7) can be expressed as

$$\rho_{1,2} = \frac{2A'_+}{\gamma} \frac{2\delta/\gamma + i}{1 + (2\delta/\gamma)^2} \left[1 - \exp\left(-\frac{\gamma}{2}(1 + 2i\delta/\gamma)t\right) \right]. \quad (6.8)$$

The imaginary part, $\text{Im}(\rho_{1,2})$, is associated with absorption while the real part, $\text{Re}(\rho_{1,2})$, is associated with an index of refraction. Working in normalized units for the electric field amplitude, the transmitted σ^+ light intensity through the optically thin gas can be characterized by an optical depth (i.e. number of e^{-1} absorption lengths) that is expressed as

$$\text{O.D.}_+ = -\ln\left([1 - \eta \text{Im}(\rho_{1,2})]^2\right), \quad (6.9)$$

where η is a unitless scale factor introduced to account for the gas density and physical constants relating the dipole coherence to the light absorption. For the calculations in this section, we choose $\eta = 1$ such that $\text{O.D.}_+ \sim .01$ for $t \gg 1/\gamma$. Figure 6.2(a) shows (6.9) and $\eta \text{Re}(\rho_{1,2})$ plotted as functions of time with the same horizontal time axis. Figure 6.2(b) shows the same curves, but with the optical depth plotted with an additional time axis that is a factor of 2 shorter, where the new time axis is displayed on the top of the figure. In this case, the amplitude and phase component differ by exactly a factor of 2 with regard to their peak response. A Taylor expansion of (6.8) about $t = 0$ shows the leading order for the amplitude component is linear in time and the leading order for the phase component is quadratic in time. This produces the difference in curvature visible at early times in figure 6.2.

This simple calculation also provides insight into the evolution of the index of refraction of an absorptive medium illuminated by a very short (with respect to the medium's characteristic radiative lifetime) pulse of light. For a sufficiently large detuning, the phase response of the medium oscillates rapidly about an average nonzero value, as shown in figure 6.3. Observation timescales that average over this oscillation period will measure an appreciable index of refraction that develops in a very short amount of time, even for sub-lifetime timescales. In other words, for light detuned much more than a natural linewidth from an atomic transition, the apparent index response timescale will be given by the inverse of the detuning for measurements with sufficiently coarse time sensitivity.

Extending the simple calculation to a transition with an $F > 0$ ground state results in an immediate departure from a factor of 2 difference between the amplitude and phase components. To illustrate this, we use the $F = 3$ to $F = 4$ transition with magnetic sublevels depicted in figure 6.1(b). The additional magnetic sublevels means there is a range of Zeeman induced detunings associated with the various transitions. A transition at the edge of the sublevels (e.g. $m_F = +3$ to $m_F = +4$) has the largest detuning labeled δ . Assuming low-intensity incident light with an instantaneous turn-on, the optically thin gas can be treated by solving 14 independent optical Bloch equations for the dipole coherences. The complex amplitude of the σ^+ (σ^-) polarization compo-

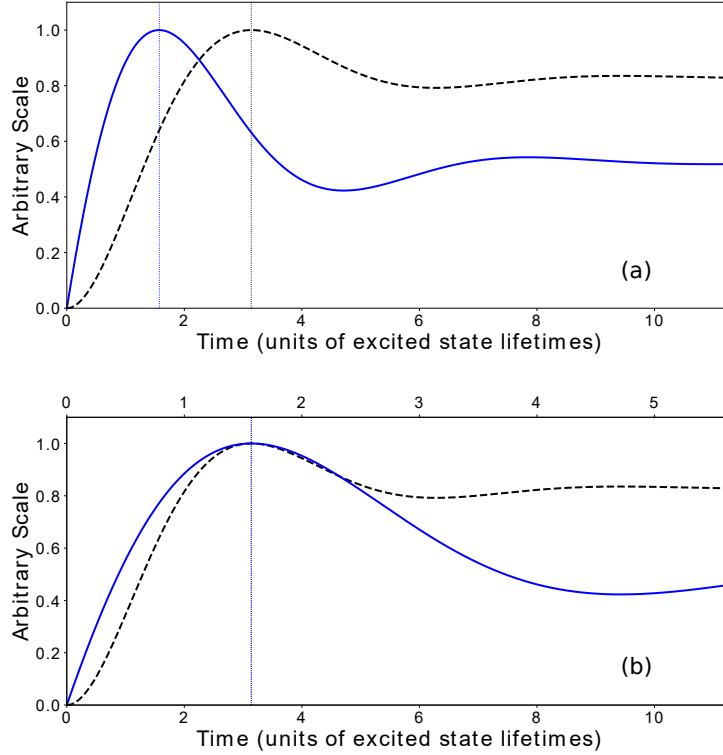


Figure 6.2: Time-dependent optical depth (blue solid curve) and time-dependent phase (black dashed curve) of the transmitted σ^+ polarization component through an optically thin gas of atoms driven on a simple $F = 0$ to $F = 1$ transition, where $A'_+ = .01\gamma$ and $\eta = 1$. The magnitude of the induced detuning in the calculations is $|\delta| = 1.0\gamma$. The blue (black) dotted vertical line indicates the time when the optical depth (phase response) reaches its maximum. Subfigure (a) shows the curves plotted on the same horizontal axis, with a clear separation between the times corresponding to the maximum of each curve. Subfigure (b) shows that when the phase response is plotted with respect to the bottom horizontal axis and the optical depth is plotted with respect to a separate horizontal axis scaled by a factor of 2 (shown on top of the subfigure), the dotted vertical lines exactly overlap. Note that the vertical axis is a normalized scale. Figure reproduced from [8].

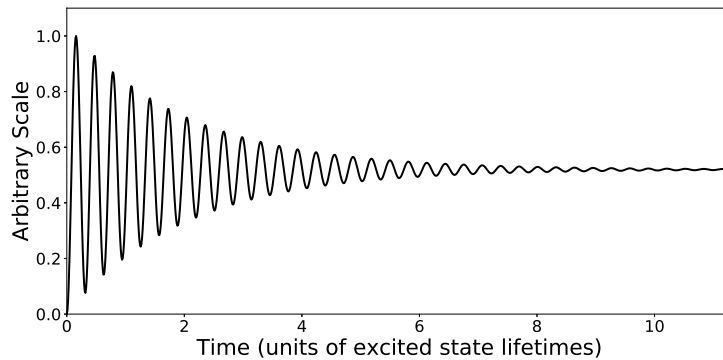


Figure 6.3: Phase response for an optically thin gas of atoms driven on a simple $F = 0$ to $F = 1$ transition with a large detuning, $|\delta| = 20\gamma$. Figure reproduced from [8].

nent dipole response is then proportional to the superposition of dipole coherences corresponding to $\Delta m = +1$ ($\Delta m = -1$) transitions. The dipole coherences have solutions of the form expressed by (6.8), but with a detuning that is different for each transition. Figure 6.4 shows that the additional frequency components lead to less than a factor of 2 between the peak response times for the amplitude and phase. As the magnetic field induced detuning increases there is a faster response for both the amplitude and the phase.

In contrast to these simple systems, our experiments were not performed in an optically thin gas, but rather an optically thick gas. This plays a role in the predictions of the total light transmission through the gas and requires including the \hat{z} -direction absorption of the ultracold gas in the calculations. We describe this inclusion in the next section.

6.2.3 Dividing the Gas into Increments

We return to the envelope equation derived in section 6.2.1 with the motivation of including the \hat{z} -direction absorption to accurately model the time-dependent evolution of light in an optically thick ultracold gas. The general solution to (6.6) with respect to an initial reference position, $z = 0$, can be expressed as

$$\tilde{A}_{\pm}(z, t) = \tilde{A}_{\pm}(0, t) + \frac{i}{2} \int_0^z dz' \tilde{\beta}_{\pm}(z', t). \quad (6.10)$$

We have approximated the gas as having a uniform density, which is reasonable in the absence of diffraction effects. Our theoretical calculations depend on numerically integrating (6.10). To do so, it is necessary to identify the contributions to the dipole response terms in the integrand. We obtain the dipole response terms in the integrand by first calculating the density matrix for all states associated with the $5S_{1/2} F = 3$ to $5P_{3/2} F = 4$ transition in ^{85}Rb . We include the magnetic sublevels of the ground state ($F = 3$) and excited state ($F = 4$) shown in figure 6.1(b). Time-dependent Faraday rotation of the total light is introduced into the calculation by including a magnetic field in the \hat{z} -direction. This incorporates the Zeeman induced detunings associated with

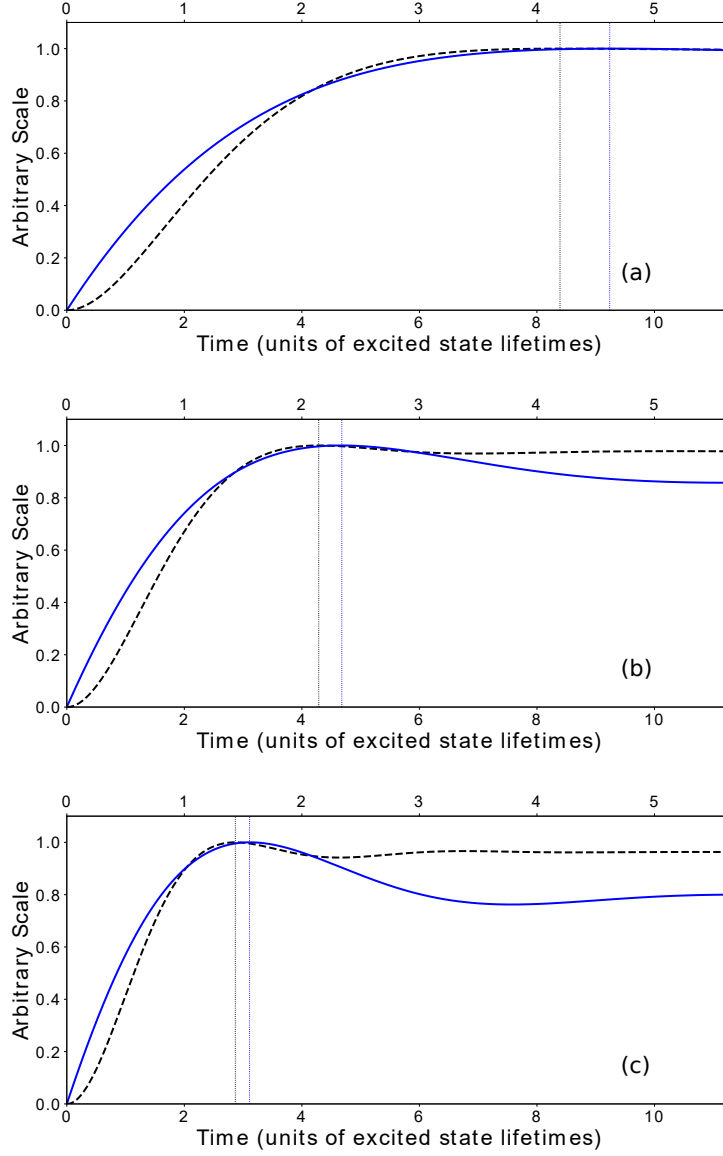


Figure 6.4: Time-dependent optical depth (blue solid curve) and time-dependent phase (black dashed curve) of the transmitted σ^+ light through an optically thin gas of multi-level atoms driven on an $F = 3$ to $F = 4$ transition in the presence of increasing applied magnetic field strengths. The ground state magnetic sublevels have initial populations that are evenly distributed. The optical depth is plotted with respect to the top horizontal axis and the phase response is plotted with respect to the bottom horizontal axis. The subfigures (a)-(c) are the results when the magnitude of the magnetic field induced detuning for the outermost allowed transition between ground and excited state magnetic sublevels is (a) $|\delta| = 0.5\gamma$, (b) $|\delta| = 1.0\gamma$, and (c) $|\delta| = 1.5\gamma$. The blue (black) dotted vertical line indicates the time when the optical depth (phase response) reaches its maximum. Figure reproduced from [8].

the energy level shifts and leads to 256 coupled optical Bloch equations that we solve to determine a 16×16 density matrix

$$\rho = \begin{pmatrix} \rho_{1,1} & \cdots & \rho_{1,16} \\ \vdots & \ddots & \vdots \\ \rho_{16,1} & \cdots & \rho_{16,16} \end{pmatrix}, \quad (6.11)$$

where the subscripts 1 to 7 correspond to the magnetic sublevels ($m_F = -3, \dots, +3$) in the ground state and 8 to 16 correspond to the magnetic sublevels ($m_F = -4, \dots, +4$) in the excited state.

Once the density matrix is determined, we calculate $\tilde{\beta}_+(z, t)$ by summing the dipole coherence terms (i.e. off-diagonal elements) that correspond to $\Delta m_F = +1$ ground-excited state transitions and $\tilde{\beta}_-(z, t)$ by summing the dipole coherence terms that correspond to $\Delta m_F = -1$ ground-excited state transitions. Besides coherences between ground and excited states, there are also ground-ground (e.g. $\rho_{1,2}$) and excited-excited coherences (e.g. $\rho_{8,9}$), and they play different and lesser roles in the overall response of the atoms.

A critical aspect of our calculations is to divide the ultracold gas into equally spaced increments of equal optical depth along the \hat{z} -direction. We calculate the density matrix for each increment at each time step, where the density matrix for an increment is used to calculate the average dipole response of the atoms within that increment. The local driving field for subsequent increments is then the superposition of the incident driving field and the dipole responses from preceding increments. The polarization components of the local driving field for an increment located at position z are given by (6.10), where the position of the increment with respect to $z = 0$ corresponds to the limit of integration.

For our calculations, we use 20 increments with each increment having an optical depth of $1/20$ the total optical depth, where the total optical depth is typically between 1 and 2. Once the complex amplitudes of the polarization components are calculated for each increment at each time step, we can determine the time-dependent phase difference of the transmitted light

$$\Delta\phi(t) = \phi_+(t) - \phi_-(t), \quad (6.12)$$

where $\phi_{\pm}(t)$ are the phases associated with the complex polarization components of the light given by (6.10). Equation (6.12) represents the phase difference between the σ^+ and σ^- polarization components of the total transmitted light after the light has propagated through the full \hat{z} -direction spatial extent of the gas. The amount of polarization rotation incurred by the light as it propagates through the gas is directly attributable to the phase difference.

6.2.4 Constraining Calculation Parameters

To make theoretical predictions that correspond to our experimental conditions, we use experimental data to constrain the physical parameters required for the calculations. These parameters include the magnitude of the magnetic field, the laser detuning, and the average initial ground state magnetic sublevel population distribution (referred to as "m-state distribution" for the remainder of this chapter) in the ultracold gas. The acousto-optic modulator (AOM) that we use to turn the incident light on quickly induces a linear frequency chirp during turn-on. We independently measured that to be the case and so include a linear chirp when calculating the atom response.

Theoretical predictions and experimentally measured transmission data collected over a range of experimental conditions are used to perform a least-squares-minimization to find best-fit values for these parameters. The calculations maintain no assumptions of low-intensity or steady-state. This means that all 256 coupled differential equations required to determine the density matrix must be solved for each set of optimization parameters. Furthermore, this number of equations must be solved for each increment at each timestep, equating to over 5000 coupled equations being solved at each timestep.

Since the optimization parameters associated with the magnetic field and frequency chirp represent quantities that are the same for all data sets, we implement a least-squares-minimization routine that varies those parameters and compares solutions to all experimental data sets simultaneously. The measured signals are far more sensitive to the global parameters than could be determined from other practical experimental measurements, and so fit corrections were included

to capture the deviation from our measured quantities. An auxiliary set of our typical data, but at deliberately varied detunings, was used to determine the laser detuning.

The m-state distribution is expected to vary between experiments, so we implement a separate least-squares-minimization routine that holds the global parameters constant while varying the m-state distributions for individual experimental data sets. The m-state distribution includes seven distinct population values corresponding to the $m_F = -3, \dots, +3$ magnetic sublevels in the ground state. While the general distribution affects the measured signals, the precise individual variation of the m-state distribution has far less effect. For example, a distribution with more population in the positive m-states versus the negative m-states will produce distinct signals, but capturing the exact population in each of the m-states is less crucial. Therefore, we simplify the number of parameters to three such that the populations in an m-state distribution are set by an average, a linear, and a quadratic constant. This simplification also allows for performing the multidimensional optimization in a reasonable amount of time (\sim hours) on a modern desktop central processing unit (CPU). We deliberately varied the magnetic field between different predetermined values during experimental data collection to better constrain the m-state distribution. The net result of these calculations are predictions of the time-dependent light in an ultracold gas of atoms corresponding to our experimental conditions.

6.3 Experimental Methods

Our experimental measurements of the time-dependent development of Faraday rotation were performed using an ultracold gas of ^{85}Rb . A near-resonance laser beam tuned to the $5S_{1/2} F = 3$ to $5P_{3/2} F = 4$ cycling transition was turned on rapidly over a timescale faster than the excited state lifetime ($\tau = 26.25$ ns [54]) of the atoms. This beam was directed through the center of the ultracold gas. The total transmitted light was decomposed into orthogonal polarization components and detected on two independent fast photoreceivers. A schematic depicting the experimental implementation is shown in figure 6.5.

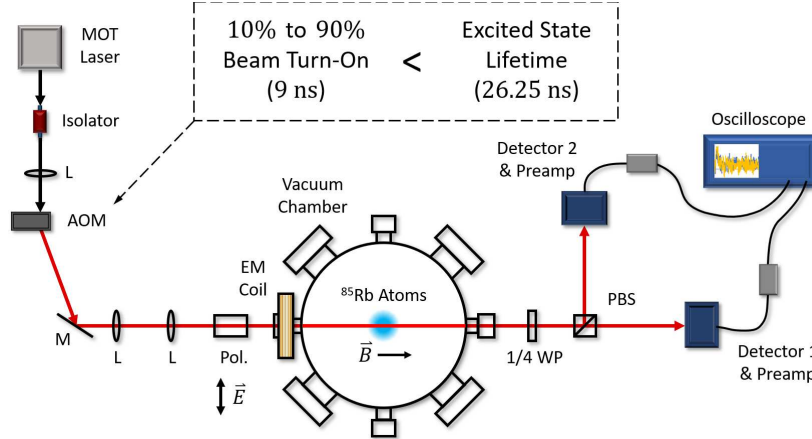


Figure 6.5: Schematic depicting the experimental set-up used to measure the time-dependent Faraday rotation in an ultracold gas. The beams used to form the initial MOT are left out for clarity. Note that the near-resonance beam has a turn-on time that is faster than the excited state lifetime of the atoms. Figure reproduced from [8].

We started our experiments by forming an ^{85}Rb Magneto-Optical Trap (MOT) using standard techniques [22]. After the MOT formation, the trap light and magnetic fields were turned off and the atoms were given 4 ms to expand. This resulted in an ultracold gas with a root-mean-square (RMS) spatial extent in one dimension of approximately 0.9 mm (determined through separate absorption imaging measurements). A magnetic field was then applied to the gas. The magnitude of the magnetic field at the location of the atoms was set to a value between 1.3 Gauss and 6.2 Gauss depending on the experiment. We did not increase the magnetic field further in this iteration of the experiment because doing so results in the development of a non-negligible dipole amplitude associated with the $5S_{1/2} F = 3$ to $5P_{3/2} F = 3$ transition. Including this transition along with possible decay paths substantially increases the number of coupled differential equations required to accurately model the system.

6.3.1 Near-Resonance Beam

With a well-defined axis provided by the magnetic field, we applied a near-resonance laser beam along the same direction through the gas. The near-resonant beam was derived from the MOT laser and a rapid turn-on time was realized by tightly focusing the beam into a 200 MHz AOM. The AOM driver was triggered by a 5 ns rise time function generator which resulted in a

10% to 90% 1st order deflection turn-on time of 9 ns. The deflected beam was collimated and sized to a spot size of $364 \mu\text{m}$, which led to a peak intensity polarization-averaged saturation parameter of $I/I_{sat} = 0.2$, where $I_{sat} = 4.8 \text{ mW cm}^{-2}$. The fast photoreceivers used for detection resulted in a signal-to-noise ratio that limited our ability to reduce the intensity much lower without dramatically increasing the amount of data required for a measurement. The near-resonance beam was passed through a Glan-Thompson polarizer external to the vacuum chamber so the incident light on the atoms was linearly polarized perpendicular to the magnetic field direction.

Positioned on the output side of the vacuum chamber was a quarter waveplate followed by a polarizing beam splitter (PBS) cube. The orientation of the quarter waveplate's fast axis with respect to the input field's polarization direction determined what type of signal we measured. The two primary orientations we used for our measurements were 45° and 0° . Using the 45° orientation led to the σ^+ and σ^- polarization components of the total transmitted light being split into separate paths after the PBS. In this configuration, we measured the transmitted light with and without ultracold atoms present in the vacuum to determine the optical depth associated with each of the polarization components.

Using the 0° orientation and having no ultracold atoms present in the vacuum led to the incident light being transmitted through the PBS onto detector 1 (see figure 6.5), and only a small background signal on detector 2. When atoms were present, any relative phase shift between the σ^+ and σ^- polarization components imparted by the atoms while responding to the incident light caused the polarization vector of the total light to rotate, resulting in a time-dependent transmission signal developing on detector 2.

6.4 Experimental Data and Predictions

Data collection was performed by interleaving measurements using the 0° and 45° orientations and two predetermined magnetic field values. The data collection sequence constrained the parameters in our theory calculations. Approximately 24 repeated measurements were taken for each specific waveplate and magnetic field combination, and the measurements were combined together

to produce curves like those shown in figures 6.6-6.8. Each of those figures show experimental data collected in the presence of ultracold atoms in the vacuum and corresponding theoretical transmission curves.

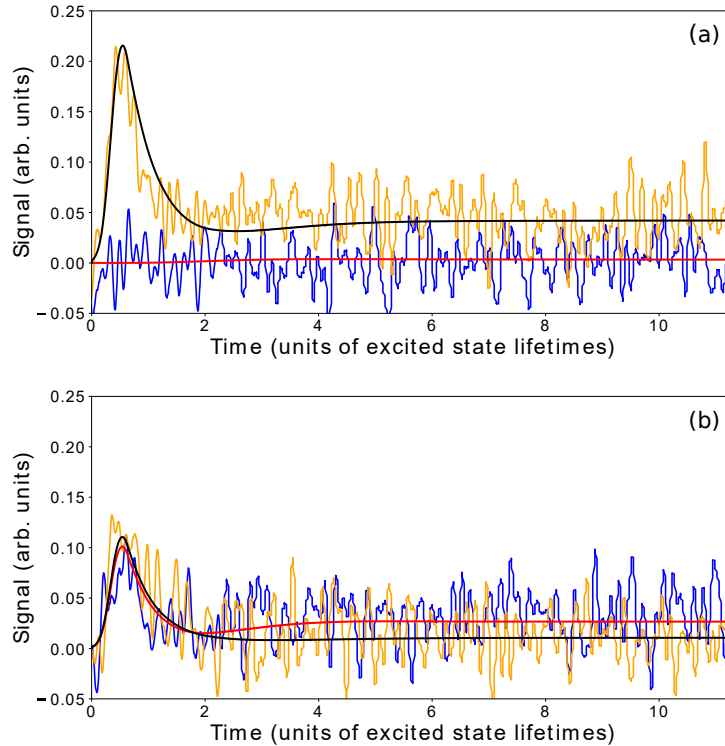


Figure 6.6: Experimental data and theoretical calculations in the presence of a $B = 1.3$ Gauss magnetic field along the axis of light propagation. Subfigure (a) is data and predictions when the quarter waveplate’s fast axis is positioned at 0° , and subfigure (b) is data and predictions when the quarter waveplate’s fast axis is positioned at 45° . The yellow and blue data are measurements collected on detector 1 and 2, respectively. The black and red curves are the predicted transmission corresponding to the light on detector 1 and 2, respectively. Figure reproduced from [8].

As shown in figures 6.6-6.8, the initial transparency of the gas leads to a peak in the transmission as the incident light turns on, and this intensity peak is visible in data collected using both waveplate orientations. The initial transparency is a direct result of the atoms requiring a finite amount of time to develop an appreciable dipole amplitude in response to the incident light. Before this happens, the incident light is able to transmit through the gas nearly unattenuated. The transmission peak then decays to a steady-state value as the atoms begin to radiate in response to the driving field. As well as the transmitted amplitude, a time-dependent polarization rotation

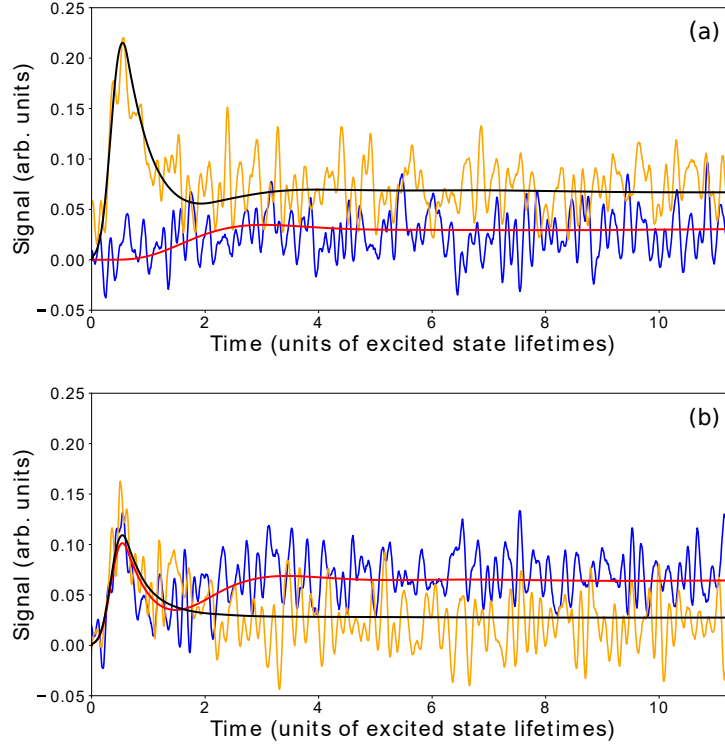


Figure 6.7: The same type of data as shown in figure 6.6, except $B = 4.4$ Gauss. Figure reproduced from [8].

develops as the atoms impart a differential phase shift between the polarization components of the light. The signal from this Faraday rotation can be seen in the data collected with detector 2 using the 0° waveplate orientation. From data collected using the 45° waveplate orientation, we calculate the overall transmission associated with each polarization component. This data also provides sensitivity to the m-state distribution in the gas.

6.5 Time-Dependent Response

We have compared our experimental data to theoretical predictions, and good agreement was obtained. While the data itself was used to constrain the precise value of some experimental parameters, this was done either across all of the data sets collected or across alternating conditions to produce a meaningful comparison. To characterize the time-dependent Faraday effect, we use the phase difference defined by (6.12). The phase difference, $\Delta\phi(t)$, can also be extracted through fitting smooth curves directly to the measured data. Given the agreement between data and the-

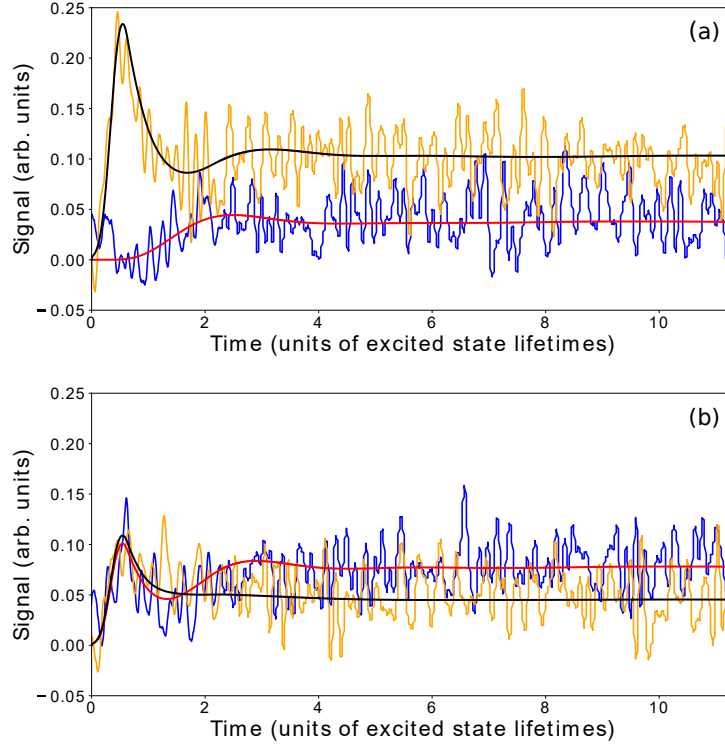


Figure 6.8: The same type of data as shown in figure 6.6, except $B = 6.2$ Gauss. Figure reproduced from [8].

ory predictions, however, the basic features of the time-dependent development of the polarization rotation can be extracted from the matched theory curves with little difference from a direct determination from the data.

In addition to determining the phase response, we calculate the time-dependent development of the opacity in the ultracold gas (i.e. the evolution of the optical depth). This is expressed as

$$\text{O.D.}(t) = -\ln\left(\frac{I(t)}{I_0(t)}\right), \quad (6.13)$$

where $I(t)$ is the total transmitted light intensity as a function of time and $I_0(t)$ is the total incident light intensity as a function of time. The results of the phase response calculations and the evolution of the opacity calculations for data sets collected using three different magnetic fields are shown in figure 6.9.

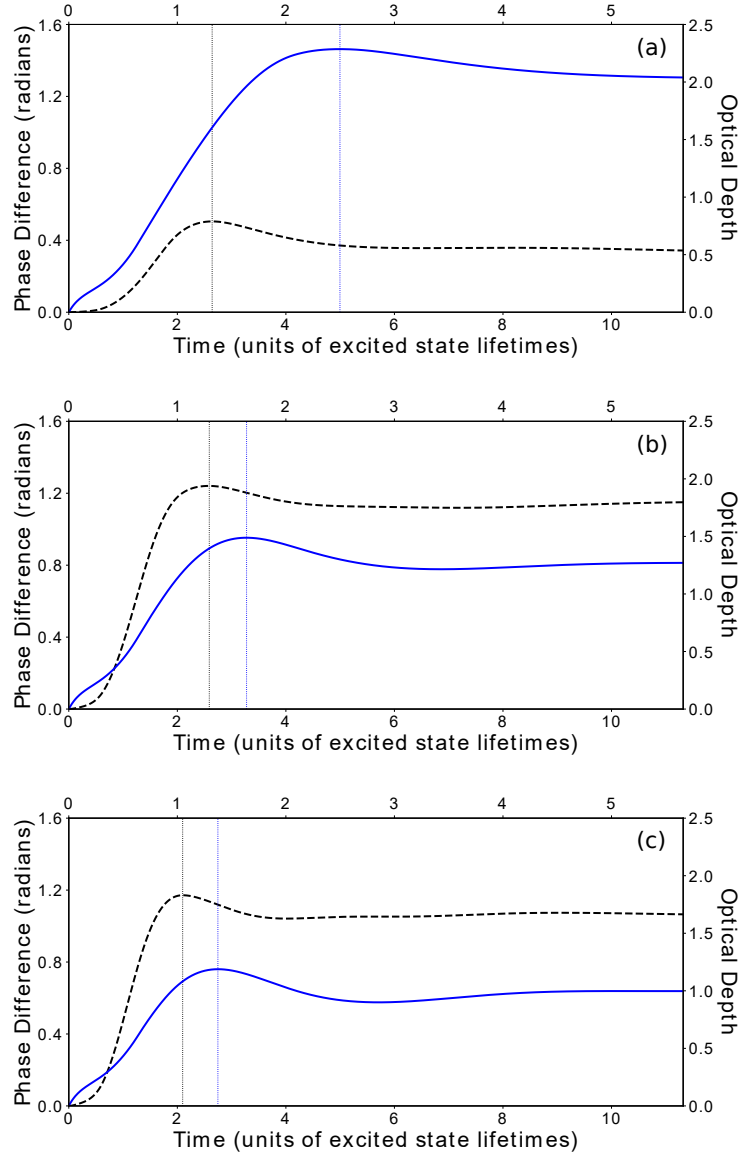


Figure 6.9: Time-dependent optical depth (blue solid curve) and time-dependent phase difference (black dashed curve) calculated from the theory curves of figures 6.6-6.8. The optical depth is plotted with respect to the top horizontal axis and the phase response is plotted with respect to the bottom horizontal axis. The subfigures (a)-(c) are the results when the magnitude of the magnetic field quantization axis is (a) $B = 1.3$ Gauss, (b) $B = 4.4$ Gauss, and (c) $B = 6.2$ Gauss. The blue (black) dotted vertical line corresponds to the time when the optical depth (phase response) reaches its maximum. Figure reproduced from [8].

The curves shown in figure 6.9 share expected characteristics with the simple calculations (see section 6.2.2) for an ultracold gas of atoms with multiple ground state magnetic sublevels. These characteristics include a clear separation between the peak response times of the optical depth and phase difference, along with increasingly faster response times for larger applied magnetic fields. Figure 6.9 also illustrates the difference between the time-dependent response of the amplitude component and the time-dependent response of the phase component near $t = 0$ for a realistic finite turn-on time. The amplitude response begins to develop almost immediately after the incident light is turned on, whereas the phase response has a delayed onset under all conditions. This is expected given the functional time-dependence of the amplitude and the phase components of the light, as discussed in section 6.2.2.

6.5.1 Influences on Response Times

From the model developed using a multi-level atom gas with no constraints on the incident light intensity, it is straightforward to identify various parameters that can influence the optical depth and phase response times in a detectable way. These parameters include the incident light frequency detuning and the magnetic field. For instance, larger magnetic fields have larger detunings and that drives the dipole response to a peak value more rapidly than for smaller magnetic fields. Additionally, the particular m-state distribution plays a role by weighting the Zeeman induced detuning contributions associated with each transition. Also, saturation effects influence the response times by making them shorter, although for our conditions the impact of saturation effects on the fitted response times is only a few percent.

As discussed in section 6.2, the optical thickness plays a role in the gas response time in a way that is different than the factors discussed above. For an optically thick gas in steady-state, the atoms on the side of the gas opposite to the incident light will have relatively small dipole amplitudes. This is a result of the light intensity at those atoms' location being less than the incident light due to absorption in the gas [151]. When the light is initially applied to the gas, though, there is much less absorption, and the atoms on the opposite side of the gas are driven by light that has

a higher intensity than in steady-state. This does not persist for long, since the gas absorbs the incident light more and more as a function of time. However, the larger-than-steady-state intensity drives those atoms toward (or even past) their steady-state dipole response much faster during the period of relative transparency (as shown in figure 6.10). This means that the larger the optical thickness of the gas, the shorter the timescale for the gas to absorb the light, since more atoms will be strongly "overdriven" at early times. The result is a total transmitted intensity that has a characteristic timescale that is faster than the excited state lifetime of the atoms. The faster response times due to this effect were apparent in our theoretical calculations, and necessitated breaking the gas up into increments (see section 6.2.3) along the light propagation direction. We also observed this effect in general with some of our data sets, but those sets were not included in our most comprehensive analysis due to insufficient information necessary for characterizing the m-state distributions.

A similar effect occurs for the development of polarization rotation with time as a function of the optical thickness of the gas, but the effect is not as pronounced as in the absorption case. As discussed above, the phase response of the atoms is slower than the absorption response and so the polarization component overdrive is reduced as the intensity falls relatively faster than the phase response. In addition, at early times (after the incident light turn-on) the atoms are being driven by light with a phase that is different than in steady-state. This tends to mute the polarization overdrive effect to a greater extent than the absorption effect. Nevertheless, a reduction in the time to reach steady-state as much as a factor of 2 is not uncommon for our conditions, and so this is still a significant effect.

6.6 Time-Dependent Faraday Rotation Conclusions

Atoms in an ultracold gas do not respond instantaneously to the sudden application of near-resonant light, and this has important consequences for the underlying dynamics in the system before it reaches steady-state. We have theoretically described and experimentally measured the time-dependent development of Faraday rotation in an ultracold gas subjected to an applied mag-

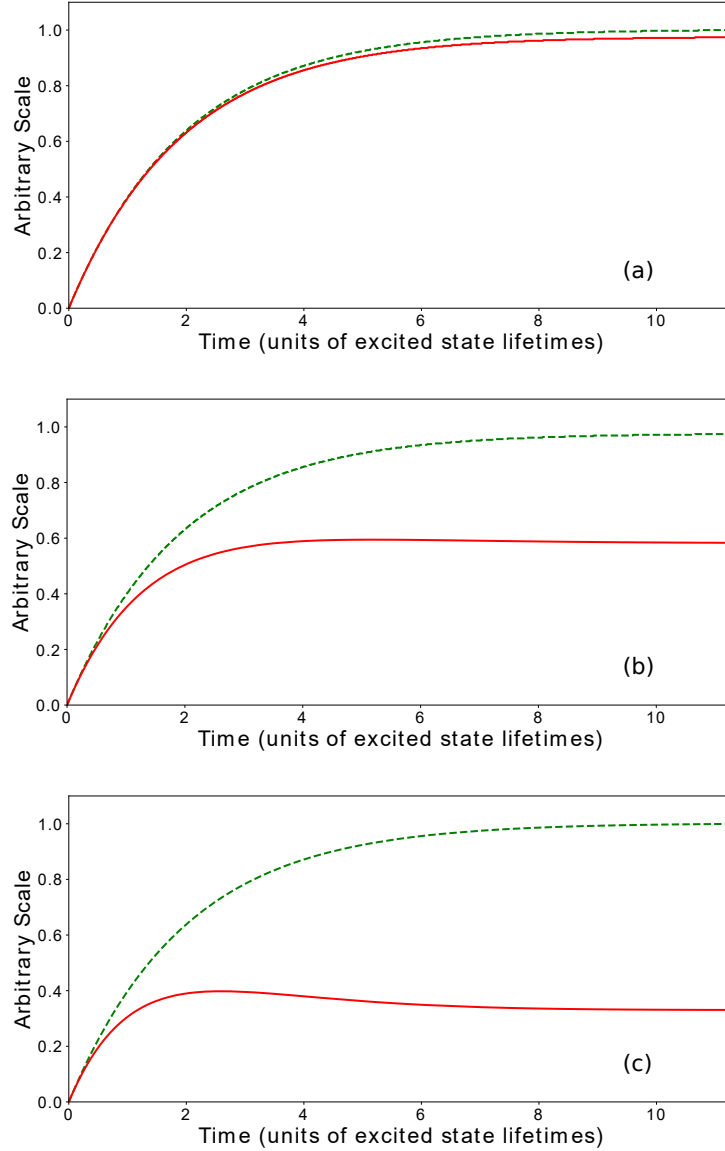


Figure 6.10: Time-dependent magnitude of the σ^+ polarization component dipole amplitude in the first (green dashed curve) and last (red solid curve) increment of a calculation using 20 increments in the z -direction. The last increment corresponds to the side of the gas opposite to the incident light. The calculation is performed in the low-intensity ($I \ll I_{sat}$) limit with zero detuning and no magnetic field. The ground state magnetic sublevels have initial populations that are evenly distributed. The subfigures (a)-(c) are the results when the optical depth is (a) O.D. = 0.06, (b) O.D. = 1.2, and (c) O.D. = 2.4. The curves in each subfigure are normalized to the maximum dipole amplitude value in the first increment for easier comparison between subfigures.

netic field, and good agreement between experimental results and theoretical predictions was obtained. Polarization rotation is ultimately due to phase shifts induced by the real part of indices of refraction in the gas, and a naive expectation would be that the development of those phase shifts requires about a factor of 2 longer in time than absorption effects. The actual situation is more complex and involves numerous factors that influence the phase response timescale in ways that make general characterizations difficult. For realistic systems, the phase response is slower than the absorption response, though.

Among the various parameters of the system that influence the response times is the optical thickness of the gas. During the initial application of a light pulse, the atoms on the opposite side of the gas from the incident light are driven much more rapidly towards their steady-state response than they would be in an optically thinner gas. Capturing this optical thickness effect is important for accurately describing the development of absorption and phase responses in an ultracold gas, and would likely need to be considered in any applications or experiments using very short near-resonant light pulses in similar systems.

The research presented in Chapter 6 has been submitted in the form of a manuscript to Physical Review A. If accepted for publication, the bibliographic information on the arXiv repository [8] will be updated to include the DOI for the peer-reviewed paper.

Chapter 7

Radiation Transport Through an Ultracold Gas

This chapter is intended to provide an overview on the direction of our research group moving forward. Our successful measurements of the time-dependent development of opacity and Faraday rotation in an ultracold gas provides the group with a good understanding of intricacies involved when measuring radiation transport physics over short timescales. In addition, those measurements allowed us to evaluate our theoretical approach using a straightforward experimental measurement. There were non-intuitive aspects of the relevant physics that would have been more time-consuming to realize and characterize using the more advanced measurement technique that will be described in this chapter. We now have the numerical tools to compare to experimental measurements that we are confident will be effective in evaluating and analyzing light propagation through our new measurement technique for observing radiation transport physics in an optically thick ultracold gas.

The main idea behind the next phase of research is to implement a measurement technique that allows us to spatially and temporally resolve the location of atoms that have been excited by particular frequencies of light. We will send a laser beam through a gas of Rb atoms, and the laser will be resonant on the $5S_{1/2}$ to $5P_{3/2}$ transition (780 nm). That will cause the atoms to scatter light, and we will then measure the propagation of that scattered light through the optically thick gas. Since the excited state atom population is a function of the intensity of light, tracking the excited state atom population tracks light intensity as it moves through the optically thick gas. To measure the excited state atoms, we will use a resonant photon excitation from the $5P_{3/2}$ excited state to the $5D_{5/2}$ excited state (776 nm). From there, we will use a 1064 nm laser pulse to ionize those atoms. The energy levels involved in the sequence are shown in figure 7.1. The resulting ions will be accelerated toward a micro-channel plate (MCP) detector using a DC electric field, as shown in figure 7.2. The $5P_{3/2}$ to $5D_{5/2}$ excitation laser will be focused to a size smaller than the ultracold gas, and so can probe different spatial regions of the gas. Information about the

location of an ionized atom along the direction of this $5P_{3/2}$ to $5D_{5/2}$ beam can be obtained from the resulting ion's time of flight. Temporal resolution will come from carefully timing the applied lasers. By waiting a variable amount of time between the lasers responsible for the $5S_{1/2}$ to $5P_{3/2}$ excitation and $5P_{3/2}$ to $5D_{5/2}$ excitation, the time-dependent propagation of light in an optically thick ultracold gas can be measured. This of course is not a direct light intensity measurement, but rather a measurement of the location of atoms that have been excited by a particular frequency of light. However, the light propagation and diffusion through the gas can be traced from the excited state atom distribution.

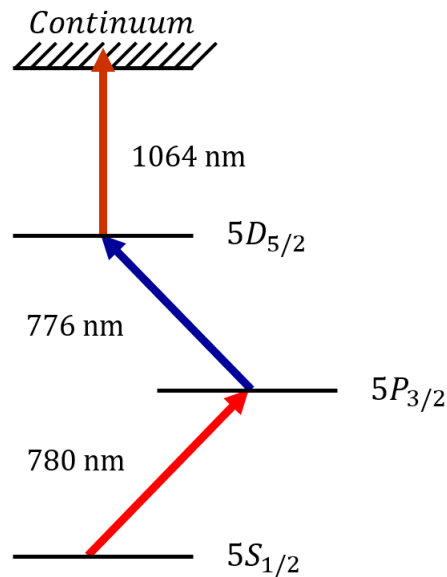


Figure 7.1: Relevant energy levels for the resonant photon excitations and ionization pulse used in the radiation transport measurement technique.

Other experiments have measured the time behavior of light diffusing through an optically thick ultracold gas. This was done by illuminating the gas with a laser and then measuring the time-dependence of the light escaping the gas using time-sensitive photon detectors positioned outside of the gas (e.g. [114]). The measured signal was then used to determine a light diffusion rate through the gas. These experiments rely on a model of the light propagation through the gas as they do not directly observe a signal sensitive to the light as a function of position and time inside the gas. In addition, these experiments are not sensitive to short times after the initial atom

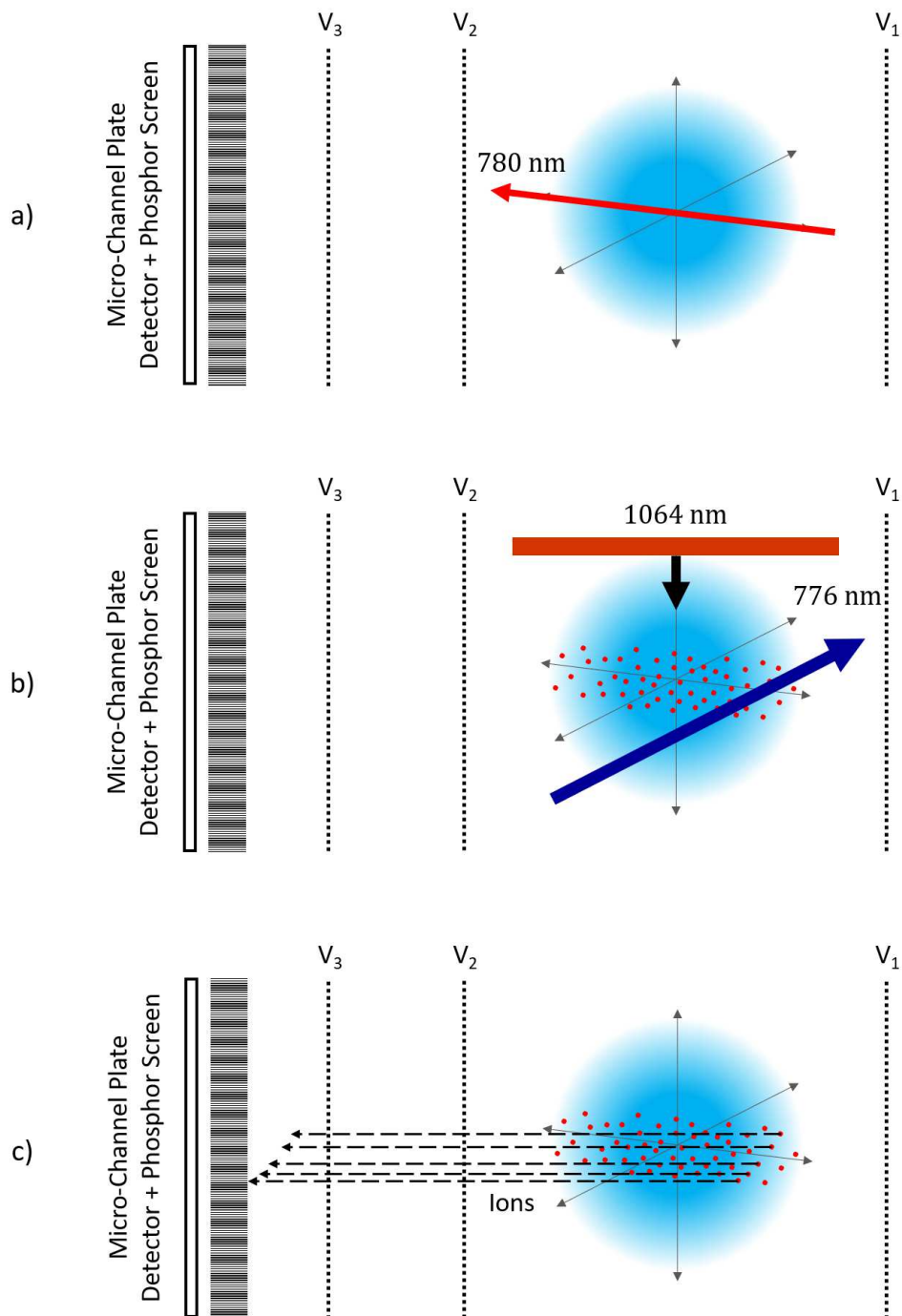


Figure 7.2: Schematic of the resonant laser beams and ionization laser pulse used in the radiation transport measurement technique. Part a) shows the application of the 780 nm laser beam (light red) used to excite atoms (light blue circle) from the $5S_{1/2}$ ground state to the $5P_{3/2}$ excited state. Part b) shows the application of the 776 nm laser beam (dark blue) used to excite atoms from the $5P_{3/2}$ excited state to the $5D_{5/2}$ excited state. Also shown is the 1064 nm ionization pulse (bronze) propagating along a direction that passes through the center of the gas. Part c) shows the resulting ions being accelerated toward the micro-channel plate (MCP) detector. The dotted vertical lines correspond to voltage grids and the voltages will be approximately $V_1 = +10$ V, $V_2 = -10$ V, and $V_3 = -200$ V.

excitation, since the signal detection only occurs once light escapes the gas. The usual approach in those experiments is to first let the gas come into steady-state, then turn off the excitation light and measure the decay of the light signal escaping the gas. Light takes time to diffuse through the optically thick gas, so by measuring the escaped light signal, the diffusion rate can be inferred. The new measurement technique described in this chapter does not have these limitations. It can measure the light diffusion inside the gas and can look at short-time behavior. This allows a different investigation of the light diffusion. In particular, the usual model of light diffusion is based on a random walk of photons. That picture cannot apply at short times after excitation (as the atoms in the gas have not had time to respond to the light). Thus, the extent of the validity of the random walk picture can be investigated in a controlled and characterizable way.

The research presented in chapter 6 was necessary to understand the physics of the atom response inside the $5S_{1/2}$ to $5P_{3/2}$ excitation beam and the time and space profile of the light scattered out of that beam. In the absence of knowing those details, the light diffusion experiment data could not be interpreted at short times.

Bibliography

- [1] G. P. Barwood, P. Gill, and W. R. C. Rowley. Frequency measurements on optically narrowed Rb-stabilised laser diodes at 780 nm and 795 nm. *Appl. Phys. B*, 53(3):142–147, 1991.
- [2] Jun Ye, Steve Swartz, Peter Jungner, and John L. Hall. Hyperfine structure and absolute frequency of the ^{87}Rb $5\text{P}_{3/2}$ state. *Opt. Lett.*, 21(16):1280–1282, 1996.
- [3] Dipankar Das and Vasant Natarajan. High-precision measurement of hyperfine structure in the D lines of alkali atoms. *J. Phys. B*, 41(3):035001, 2008.
- [4] S Bize, Y Sortais, M. S Santos, C Mandache, A Clairon, and C Salomon. High-accuracy measurement of the ^{87}Rb ground-state hyperfine splitting in an atomic fountain. *Europhys. Lett.*, 45(5):558–564, 1999.
- [5] Kristan L. Corwin, Zheng-Tian Lu, Carter F. Hand, Ryan J. Epstein, and Carl E. Wieman. Frequency-stabilized diode laser with the Zeeman shift in an atomic vapor. *Appl. Opt.*, 37(15):3295–3298, 1998.
- [6] J Gilbert, R Ferrier Wilson, and J Roberts. Spatially truncated optical pumping cooling. *New J. Phys.*, 21(6):063023, 2019.
- [7] Jonathan R. Gilbert, Colin P. Roberts, and Jacob L. Roberts. Near-resonant light propagation in an absorptive spatially anisotropic ultracold gas. *J. Opt. Soc. Am. B*, 35(4):718–723, 2018.
- [8] Jonathan R. Gilbert, Mark A. Watkins, and Jacob L. Roberts. Nanosecond-timescale development of Faraday rotation in an ultracold gas. *arXiv:1912.07553*, 2019.
- [9] T.W. Hänsch and A.L. Schawlow. Cooling of gases by laser radiation. *Opt. Commun.*, 13(1):68–69, 1975.

- [10] D. J. Wineland and Wayne M. Itano. Laser cooling of atoms. *Phys. Rev. A*, 20:1521–1540, 1979.
- [11] J. P. Gordon and A. Ashkin. Motion of atoms in a radiation trap. *Phys. Rev. A*, 21:1606–1617, 1980.
- [12] Richard J. Cook. Theory of resonance-radiation pressure. *Phys. Rev. A*, 22:1078–1098, 1980.
- [13] Stig Stenholm. The semiclassical theory of laser cooling. *Rev. Mod. Phys.*, 58:699–739, 1986.
- [14] Paul D. Lett, Richard N. Watts, Christoph I. Westbrook, William D. Phillips, Phillip L. Gould, and Harold J. Metcalf. Observation of atoms laser cooled below the Doppler limit. *Phys. Rev. Lett.*, 61:169–172, 1988.
- [15] Y. Shevy, D. S. Weiss, P. J. Ungar, and Steven Chu. Bimodal speed distributions in laser-cooled atoms. *Phys. Rev. Lett.*, 62:1118–1121, 1989.
- [16] B. Sheehy, S-Q. Shang, P. van der Straten, S. Hatamian, and H. Metcalf. Magnetic-field-induced laser cooling below the Doppler limit. *Phys. Rev. Lett.*, 64:858–861, 1990.
- [17] P. D. Lett, W. D. Phillips, S. L. Rolston, C. E. Tanner, R. N. Watts, and C. I. Westbrook. Optical molasses. *J. Opt. Soc. Am. B*, 6(11):2084–2107, 1989.
- [18] J. Dalibard and C. Cohen-Tannoudji. Laser cooling below the Doppler limit by polarization gradients: simple theoretical models. *J. Opt. Soc. Am. B*, 6(11):2023–2045, 1989.
- [19] P. J. Ungar, D. S. Weiss, E. Riis, and Steven Chu. Optical molasses and multilevel atoms: theory. *J. Opt. Soc. Am. B*, 6(11):2058–2071, 1989.
- [20] David S. Weiss, Erling Riis, Yaakov Shevy, P. Jeffrey Ungar, and Steven Chu. Optical molasses and multilevel atoms: experiment. *J. Opt. Soc. Am. B*, 6(11):2072–2083, 1989.

- [21] D. E. Pritchard, E. L. Raab, V. Bagnato, C. E. Wieman, and R. N. Watts. Light traps using spontaneous forces. *Phys. Rev. Lett.*, 57:310–313, 1986.
- [22] E. L. Raab, M. Prentiss, Alex Cable, Steven Chu, and D. E. Pritchard. Trapping of neutral sodium atoms with radiation pressure. *Phys. Rev. Lett.*, 59:2631–2634, 1987.
- [23] Fujio Shimizu, Kazuko Shimizu, and Hiroshi Takuma. Laser cooling and trapping of Ne metastable atoms. *Phys. Rev. A*, 39:2758–2760, 1989.
- [24] Harold Metcalf. Magneto-optical trapping and its application to helium metastables. *J. Opt. Soc. Am. B*, 6(11):2206–2210, 1989.
- [25] Steven Chu, J. E. Bjorkholm, A. Ashkin, and A. Cable. Experimental observation of optically trapped atoms. *Phys. Rev. Lett.*, 57:314–317, 1986.
- [26] Rudolf Grimm, Matthias Weidemüller, and Yurii B. Ovchinnikov. Optical dipole traps for neutral atoms. *Adv. At., Mol., Opt. Phys.*, 42:95–170, 2000.
- [27] J. D. Miller, R. A. Cline, and D. J. Heinzen. Far-off-resonance optical trapping of atoms. *Phys. Rev. A*, 47:R4567–R4570, 1993.
- [28] Anthony R. Gorges. *Simultaneous trapping of ^{85}Rb & ^{87}Rb in a far off resonant trap*. PhD thesis, Colorado State University, 2010.
- [29] Mathew Hamilton. *Experimental realization of two-isotope collision-assisted Zeeman cooling*. PhD thesis, Colorado State University, 2013.
- [30] Rebekah Ferrier Wilson. *Spatially-selective Optical Pumping cooling and Two-Isotope Collision-assisted Zeeman cooling*. PhD thesis, Colorado State University, 2014.
- [31] Peter Van der Straten and Harold Metcalf. *Atoms and Molecules Interacting with Light: Atomic Physics for the Laser Era*. Cambridge University Press, 2016.

- [32] Steven Chu, L. Hollberg, J. E. Bjorkholm, Alex Cable, and A. Ashkin. Three-dimensional viscous confinement and cooling of atoms by resonance radiation pressure. *Phys. Rev. Lett.*, 55:48–51, 1985.
- [33] William D. Phillips, John V. Prodan, and Harold J. Metcalf. Laser cooling and electromagnetic trapping of neutral atoms. *J. Opt. Soc. Am. B*, 2(11):1751–1767, 1985.
- [34] S. R. Muniz, K. M. F. Magalhães, Ph. W. Courteille, M. A. Perez, L. G. Marcassa, and V. S. Bagnato. Measurements of capture velocity in a magneto-optical trap for a broad range of light intensities. *Phys. Rev. A*, 65:015402, 2001.
- [35] A. Aspect, E. Arimondo, R. Kaiser, N. Vansteenkiste, and C. Cohen-Tannoudji. Laser cooling below the one-photon recoil energy by velocity-selective coherent population trapping. *Phys. Rev. Lett.*, 61:826–829, 1988.
- [36] A. Aspect, E. Arimondo, R. Kaiser, N. Vansteenkiste, and C. Cohen-Tannoudji. Laser cooling below the one-photon recoil energy by velocity-selective coherent population trapping: theoretical analysis. *J. Opt. Soc. Am. B*, 6(11):2112–2124, 1989.
- [37] Mark Kasevich and Steven Chu. Laser cooling below a photon recoil with three-level atoms. *Phys. Rev. Lett.*, 69:1741–1744, 1992.
- [38] Nir Davidson, Heun Jin Lee, Mark Kasevich, and Steven Chu. Raman cooling of atoms in two and three dimensions. *Phys. Rev. Lett.*, 72:3158–3161, 1994.
- [39] S. H. Autler and C. H. Townes. Stark effect in rapidly varying fields. *Phys. Rev.*, 100:703–722, 1955.
- [40] J. Dalibard and C. Cohen-Tannoudji. Dressed-atom approach to atomic motion in laser light: the dipole force revisited. *J. Opt. Soc. Am. B*, 2(11):1707–1720, 1985.

- [41] M. Drewsen, Ph. Laurent, A. Nadir, G. Santarelli, A. Clairon, Y. Castin, D. Grison, and C. Salomon. Investigation of sub-Doppler cooling effects in a cesium magneto-optical trap. *Appl. Phys. B*, 59(3):283–298, 1994.
- [42] C. G. Townsend, N. H. Edwards, C. J. Cooper, K. P. Zetie, C. J. Foot, A. M. Steane, P. Szriftgiser, H. Perrin, and J. Dalibard. Phase-space density in the magneto-optical trap. *Phys. Rev. A*, 52:1423–1440, 1995.
- [43] Andrejs Vorozcovs, Matthew Weel, Scott Beattie, Saviour Cauchi, and A. Kumarakrishnan. Measurements of temperature scaling laws in an optically dense magneto-optical trap. *J. Opt. Soc. Am. B*, 22(5):943–950, 2005.
- [44] A. M Steane and C. J Foot. Laser cooling below the Doppler limit in a magneto-optical trap. *Europhys. Lett.*, 14(3):231–236, 1991.
- [45] A Höpe, D Haubrich, G Müller, W. G Kaenders, and D Meschede. Neutral cesium atoms in strong magnetic-quadrupole fields at sub-Doppler temperatures. *Europhys. Lett.*, 22(9):669–674, 1993.
- [46] P Kohns, P Buch, W Süptitz, C Csambal, and W Ertmer. On-line measurement of sub-Doppler temperatures in a Rb magneto-optical trap-by-trap centre oscillations. *Europhys. Lett.*, 22(7):517–522, 1993.
- [47] Alan L. Migdall, John V. Prodan, William D. Phillips, Thomas H. Bergeman, and Harold J. Metcalf. First observation of magnetically trapped neutral atoms. *Phys. Rev. Lett.*, 54:2596–2599, 1985.
- [48] T. Bergeman, Gidon Erez, and Harold J. Metcalf. Magnetostatic trapping fields for neutral atoms. *Phys. Rev. A*, 35:1535–1546, 1987.
- [49] C. D. Wallace, T. P. Dinneen, K. Y. N. Tan, A. Kumarakrishnan, P. L. Gould, and J. Javanainen. Measurements of temperature and spring constant in a magneto-optical trap. *J. Opt. Soc. Am. B*, 11(5):703–711, 1994.

- [50] T Takekoshi, J.R Yeh, and R.J Knize. Quasi-electrostatic trap for neutral atoms. *Opt. Commun.*, 114(5):421–424, 1995.
- [51] T. Takekoshi and R. J. Knize. CO₂ laser trap for cesium atoms. *Opt. Lett.*, 21(1):77–79, 1996.
- [52] Joseph Thomas Verdeyen. *Laser Electronics*. Prentice Hall, 3rd edition, 1995.
- [53] R. Shankar. *Principles of Quantum Mechanics*. Springer, 2nd edition, 1994.
- [54] J. E. Sansonetti. Wavelengths, transition probabilities, and energy levels for the spectra of rubidium (Rb I through Rb XXXVII). *J. Phys. Chem. Ref. Data*, 35(1):301–421, 2006.
- [55] K. B. MacAdam, A. Steinbach, and C. Wieman. A narrow-band tunable diode laser system with grating feedback, and a saturated absorption spectrometer for Cs and Rb. *Am. J. Phys.*, 60(12):1098–1111, 1992.
- [56] L. Ricci, M. Weidemüller, T. Esslinger, A. Hemmerich, C. Zimmermann, V. Vuletic, W. König, and T.W. Hänsch. A compact grating-stabilized diode laser system for atomic physics. *Opt. Commun.*, 117(5):541–549, 1995.
- [57] S. Friebe, C. D’Andrea, J. Walz, M. Weitz, and T. W. Hänsch. CO₂-laser optical lattice with cold rubidium atoms. *Phys. Rev. A*, 57:R20–R23, 1998.
- [58] G. Roati, W. Jastrzebski, A. Simoni, G. Modugno, and M. Inguscio. Optical trapping of cold fermionic potassium for collisional studies. *Phys. Rev. A*, 63:052709, 2001.
- [59] Jinwei Wu, Raymond Newell, Marc Hausmann, David J. Vieira, and Xinxin Zhao. Loading dynamics of optical trap and parametric excitation resonances of trapped atoms. *J. Appl. Phys.*, 100(5):054903, 2006.
- [60] L.D. Landau, E.M. Lifshitz, J.B. Sykes, and J.S. Bell. *Mechanics*. Elsevier Science, 3rd edition, 1976.

- [61] Jacob L. Roberts. *The First Experiments with ^{85}Rb BECs*. PhD thesis, University of Colorado, 2001.
- [62] Steven Chu. Nobel lecture: The manipulation of neutral particles. *Rev. Mod. Phys.*, 70:685–706, 1998.
- [63] Claude N. Cohen-Tannoudji. Nobel lecture: Manipulating atoms with photons. *Rev. Mod. Phys.*, 70:707–719, 1998.
- [64] William D. Phillips. Nobel lecture: Laser cooling and trapping of neutral atoms. *Rev. Mod. Phys.*, 70:721–741, 1998.
- [65] Carl E. Wieman, David E. Pritchard, and David J. Wineland. Atom cooling, trapping, and quantum manipulation. *Rev. Mod. Phys.*, 71:S253–S262, 1999.
- [66] M. H. Anderson, J. R. Ensher, M. R. Matthews, C. E. Wieman, and E. A. Cornell. Observation of Bose-Einstein condensation in a dilute atomic vapor. *Science*, 269(5221):198–201, 1995.
- [67] K. B. Davis, M. O. Mewes, M. R. Andrews, N. J. van Druten, D. S. Durfee, D. M. Kurn, and W. Ketterle. Bose-Einstein condensation in a gas of sodium atoms. *Phys. Rev. Lett.*, 75:3969–3973, 1995.
- [68] B. DeMarco and D. S. Jin. Onset of Fermi degeneracy in a trapped atomic gas. *Science*, 285(5434):1703–1706, 1999.
- [69] K. M. O’Hara, S. L. Hemmer, M. E. Gehm, S. R. Granade, and J. E. Thomas. Observation of a strongly interacting degenerate Fermi gas of atoms. *Science*, 298(5601):2179–2182, 2002.
- [70] C. W. Chou, D. B. Hume, J. C. J. Koelemeij, D. J. Wineland, and T. Rosenband. Frequency comparison of two high-accuracy Al^+ optical clocks. *Phys. Rev. Lett.*, 104:070802, 2010.

- [71] Andrew D. Ludlow, Martin M. Boyd, Jun Ye, E. Peik, and P. O. Schmidt. Optical atomic clocks. *Rev. Mod. Phys.*, 87:637–701, 2015.
- [72] J. T. Bahns, W. C. Stwalley, and P. L. Gould. Laser cooling of molecules: A sequential scheme for rotation, translation, and vibration. *J. Chem. Phys.*, 104(24):9689–9697, 1996.
- [73] Lincoln D Carr, David DeMille, Roman V Krems, and Jun Ye. Cold and ultracold molecules: science, technology and applications. *New J. Phys.*, 11(5):055049, 2009.
- [74] J. I. Cirac and P. Zoller. Quantum computations with cold trapped ions. *Phys. Rev. Lett.*, 74:4091–4094, 1995.
- [75] T. D. Ladd, F. Jelezko, R. Laflamme, Y. Nakamura, C. Monroe, and J. L. O’Brien. Quantum computers. *Nature*, 464:45, 2010.
- [76] Wolfgang Ketterle and N. J. van Druten. Evaporative cooling of trapped atoms. *Adv. At., Mol., Opt. Phys.*, 37:181–236, 1996.
- [77] C. A. Sackett, C. C. Bradley, and R. G. Hulet. Optimization of evaporative cooling. *Phys. Rev. A*, 55:3797–3801, 1997.
- [78] Z. Hadzibabic, C. A. Stan, K. Dieckmann, S. Gupta, M. W. Zwierlein, A. Görlitz, and W. Ketterle. Two-species mixture of quantum degenerate Bose and Fermi gases. *Phys. Rev. Lett.*, 88:160401, 2002.
- [79] Andrew J. Kerman, Vladan Vuletić, Cheng Chin, and Steven Chu. Beyond optical molasses: 3D Raman sideband cooling of atomic cesium to high phase-space density. *Phys. Rev. Lett.*, 84:439–442, 2000.
- [80] Y. Castin, J. I. Cirac, and M. Lewenstein. Reabsorption of light by trapped atoms. *Phys. Rev. Lett.*, 80:5305–5308, 1998.
- [81] J. I. Cirac, M. Lewenstein, and P. Zoller. Collective laser cooling of trapped atoms. *Europhys. Lett.*, 35(9):647, 1996.

- [82] Steffen Wolf, Steven J. Oliver, and David S. Weiss. Suppression of recoil heating by an optical lattice. *Phys. Rev. Lett.*, 85:4249–4252, 2000.
- [83] Dudarev, A. M., Marder, M., Niu, Q., Fisch, N. J., and Raizen, M. G. Statistical mechanics of an optical phase space compressor. *Europhys. Lett.*, 70(6):761–767, 2005.
- [84] Gabriel N. Price, S. Travis Bannerman, Kirsten Viering, Edvardas Narevicius, and Mark G. Raizen. Single-photon atomic cooling. *Phys. Rev. Lett.*, 100:093004, 2008.
- [85] S Travis Bannerman, Gabriel N Price, Kirsten Viering, and Mark G Raizen. Single-photon cooling at the limit of trap dynamics: Maxwell’s demon near maximum efficiency. *New J. Phys.*, 11(6):063044, 2009.
- [86] Jeremy J. Thorn, Elizabeth A. Schoene, Tao Li, and Daniel A. Steck. Experimental realization of an optical one-way barrier for neutral atoms. *Phys. Rev. Lett.*, 100:240407, 2008.
- [87] David E. Pritchard. Cooling neutral atoms in a magnetic trap for precision spectroscopy. *Phys. Rev. Lett.*, 51:1336–1339, 1983.
- [88] Kurt W. Miller, Stephan Dürr, and Carl E. Wieman. rf-induced Sisyphus cooling in an optical dipole trap. *Phys. Rev. A*, 66:023406, 2002.
- [89] Martin Zeppenfeld, Barbara G. U. Englert, Rosa Glöckner, Alexander Prehn, Manuel Mienz, Christian Sommer, Laurens D. van Buuren, Michael Motsch, and Gerhard Rempe. Sisyphus cooling of electrically trapped polyatomic molecules. *Nature*, 491:570, 2012.
- [90] Daniel Comparat. Molecular cooling via Sisyphus processes. *Phys. Rev. A*, 89:043410, 2014.
- [91] Dian-Jiun Han, Steffen Wolf, Steven Oliver, Colin McCormick, Marshall T. DePue, and David S. Weiss. 3D Raman sideband cooling of cesium atoms at high density. *Phys. Rev. Lett.*, 85:724–727, 2000.

- [92] Anthony R. Gorges, Ansel J. Foxley, David M. French, Christopher M. Ryan, and Jacob L. Roberts. Suppression of reabsorption in ultracold gases via modulation of light. *Phys. Rev. A*, 75:053403, 2007.
- [93] Matthew T. Hummon, Mark Yeo, Benjamin K. Stuhl, Alejandra L. Collopy, Yong Xia, and Jun Ye. 2D magneto-optical trapping of diatomic molecules. *Phys. Rev. Lett.*, 110:143001, 2013.
- [94] E. B. Norrgard, D. J. McCarron, M. H. Steinecker, M. R. Tarbutt, and D. DeMille. Submillikelvin dipolar molecules in a radio-frequency magneto-optical trap. *Phys. Rev. Lett.*, 116:063004, 2016.
- [95] M R Tarbutt. Magneto-optical trapping forces for atoms and molecules with complex level structures. *New J. Phys.*, 17(1):015007, 2015.
- [96] Loïc Anderegg, Benjamin L. Augenbraun, Eunmi Chae, Boerge Hemmerling, Nicholas R. Hutzler, Aakash Ravi, Alejandra Collopy, Jun Ye, Wolfgang Ketterle, and John M. Doyle. Radio frequency magneto-optical trapping of CaF with high density. *Phys. Rev. Lett.*, 119:103201, 2017.
- [97] Loïc Anderegg, Benjamin L. Augenbraun, Yicheng Bao, Sean Burchesky, Lawrence W. Cheuk, Wolfgang Ketterle, and John M. Doyle. Laser cooling of optically trapped molecules. *Nat. Phys.*, 14(9):890–893, 2018.
- [98] Lawrence W. Cheuk, Loïc Anderegg, Benjamin L. Augenbraun, Yicheng Bao, Sean Burchesky, Wolfgang Ketterle, and John M. Doyle. Λ -enhanced imaging of molecules in an optical trap. *Phys. Rev. Lett.*, 121:083201, 2018.
- [99] Boerge Hemmerling, Eunmi Chae, Aakash Ravi, Loic Anderegg, Garrett K Drayna, Nicholas R Hutzler, Alejandra L Collopy, Jun Ye, Wolfgang Ketterle, and John M Doyle. Laser slowing of CaF molecules to near the capture velocity of a molecular MOT. *J. Phys. B*, 49(17):174001, 2016.

- [100] M. R. Tarbutt and T. C. Steimle. Modeling magneto-optical trapping of CaF molecules. *Phys. Rev. A*, 92:053401, 2015.
- [101] S. J. M. Kuppens, K. L. Corwin, K. W. Miller, T. E. Chupp, and C. E. Wieman. Loading an optical dipole trap. *Phys. Rev. A*, 62:013406, 2000.
- [102] Mathew S. Hamilton, Anthony R. Gorges, and Jacob L. Roberts. Influence of optical molasses in loading a shallow optical trap. *Phys. Rev. A*, 79:013418, 2009.
- [103] D. Sesko, T. Walker, C. Monroe, A. Gallagher, and C. Wieman. Collisional losses from a light-force atom trap. *Phys. Rev. Lett.*, 63:961–964, 1989.
- [104] M. H. Anderson, W. Petrich, J. R. Ensher, and E. A. Cornell. Reduction of light-assisted collisional loss rate from a low-pressure vapor-cell trap. *Phys. Rev. A*, 50:R3597–R3600, 1994.
- [105] John Weiner, Vanderlei S. Bagnato, Sergio Zilio, and Paul S. Julienne. Experiments and theory in cold and ultracold collisions. *Rev. Mod. Phys.*, 71:1–85, 1999.
- [106] Anthony R. Gorges, Nicholas S. Bingham, Michael K. DeAngelo, Mathew S. Hamilton, and Jacob L. Roberts. Light-assisted collisional loss in a $^{85/87}\text{Rb}$ ultracold optical trap. *Phys. Rev. A*, 78:033420, 2008.
- [107] D. W. Sesko, T. G. Walker, and C. E. Wieman. Behavior of neutral atoms in a spontaneous force trap. *J. Opt. Soc. Am. B*, 8(5):946–958, 1991.
- [108] Wolfgang Ketterle, Kendall B. Davis, Michael A. Joffe, Alex Martin, and David E. Pritchard. High densities of cold atoms in a dark spontaneous-force optical trap. *Phys. Rev. Lett.*, 70:2253–2256, 1993.
- [109] M. R. Andrews, M.-O. Mewes, N. J. van Druten, D. S. Durfee, D. M. Kurn, and W. Ketterle. Direct, nondestructive observation of a Bose condensate. *Science*, 273(5271):84–87, 1996.

- [110] Yen-Wei Lin, Hung-Chih Chou, Prashant P. Dwivedi, Ying-Cheng Chen, and Ite A. Yu. Using a pair of rectangular coils in the MOT for the production of cold atom clouds with large optical density. *Opt. Express*, 16(6):3753–3761, 2008.
- [111] M. Bajcsy, S. Hofferberth, T. Peyronel, V. Balic, Q. Liang, A. S. Zibrov, V. Vuletic, and M. D. Lukin. Laser-cooled atoms inside a hollow-core photonic-crystal fiber. *Phys. Rev. A*, 83:063830, 2011.
- [112] Ya-Fen Hsiao, Hung-Shiue Chen, Pin-Ju Tsai, and Ying-Cheng Chen. Cold atomic media with ultrahigh optical depths. *Phys. Rev. A*, 90:055401, 2014.
- [113] B M Sparkes, J Bernu, M Hosseini, J Geng, Q Glorieux, P A Altin, P K Lam, N P Robins, and B C Buchler. Gradient echo memory in an ultra-high optical depth cold atomic ensemble. *New J. Phys.*, 15(8):085027, 2013.
- [114] G. Labeyrie, E. Vaujour, C. A. Müller, D. Delande, C. Miniatura, D. Wilkowski, and R. Kaiser. Slow diffusion of light in a cold atomic cloud. *Phys. Rev. Lett.*, 91:223904, 2003.
- [115] A Fioretti, A.F Molisch, J.H Müller, P Verkerk, and M Allegrini. Observation of radiation trapping in a dense Cs magneto-optical trap. *Opt. Commun.*, 149(4):415–422, 1998.
- [116] Shanchao Zhang, J. F. Chen, Chang Liu, Shuyu Zhou, M. M. T. Loy, G. K. L. Wong, and Shengwang Du. A dark-line two-dimensional magneto-optical trap of ^{85}Rb atoms with high optical depth. *Rev. Sci. Instrum.*, 83(7):073102, 2012.
- [117] Frank Blatt, Thomas Halfmann, and Thorsten Peters. One-dimensional ultracold medium of extreme optical depth. *Opt. Lett.*, 39(3):446–449, 2014.
- [118] G. Labeyrie, R. Kaiser, and D. Delande. Radiation trapping in a cold atomic gas. *Appl. Phys. B*, 81(7):1001–1008, 2005.

- [119] Guillaume Labeyrie, Enrico Tesio, Pedro M Gomes, G-L Oppo, William J Firth, Gordon RM Robb, Aidan S Arnold, Robin Kaiser, and Thorsten Ackemann. Optomechanical self-structuring in a cold atomic gas. *Nat. Photonics*, 8(4):321–325, 2014.
- [120] Stetson Roof, Kasie Kemp, Mark Havey, I. M. Sokolov, and D. V. Kupriyanov. Microscopic lensing by a dense, cold atomic sample. *Opt. Lett.*, 40(7):1137–1140, 2015.
- [121] Bonnie L Schmittberger and Daniel J Gauthier. Spontaneous emergence of free-space optical and atomic patterns. *New J. Phys.*, 18(10):103021, 2016.
- [122] D. Boiron, A. Michaud, J. M. Fournier, L. Simard, M. Sprenger, G. Grynberg, and C. Salomon. Cold and dense cesium clouds in far-detuned dipole traps. *Phys. Rev. A*, 57:R4106–R4109, 1998.
- [123] I. M. Sokolov, M. D. Kupriyanova, D. V. Kupriyanov, and M. D. Havey. Light scattering from a dense and ultracold atomic gas. *Phys. Rev. A*, 79:053405, 2009.
- [124] M. L. Dowell, B. D. Paul, A. Gallagher, and J. Cooper. Self-focused light propagation in a fully saturable medium: Theory. *Phys. Rev. A*, 52:3244–3253, 1995.
- [125] John David Jackson. *Classical Electrodynamics*. Wiley, 2nd edition, 1975.
- [126] F. Arecchi and R. Bonifacio. Theory of optical maser amplifiers. *IEEE J. Quantum Electron.*, 1(4):169–178, 1965.
- [127] Robert W Boyd. *Nonlinear Optics*. Academic press, 2nd edition, 2003.
- [128] Kasie Kemp, SJ Roof, MD Havey, IM Sokolov, and DV Kupriyanov. Cooperatively enhanced light transmission in cold atomic matter. *arXiv:1410.2497*, 2014.
- [129] S. Slama, S. Bux, G. Krenz, C. Zimmermann, and Ph. W. Courteille. Superradiant Rayleigh scattering and collective atomic recoil lasing in a ring cavity. *Phys. Rev. Lett.*, 98:053603, 2007.

- [130] Ferdinand Brennecke, Stephan Ritter, Tobias Donner, and Tilman Esslinger. Cavity optomechanics with a Bose-Einstein condensate. *Science*, 322(5899):235–238, 2008.
- [131] Michelle O. Araújo, Ivor Krešić, Robin Kaiser, and William Guerin. Superradiance in a large and dilute cloud of cold atoms in the linear-optics regime. *Phys. Rev. Lett.*, 117:073002, 2016.
- [132] S. Balik, A. L. Win, M. D. Havey, I. M. Sokolov, and D. V. Kupriyanov. Near-resonance light scattering from a high-density ultracold atomic ^{87}Rb gas. *Phys. Rev. A*, 87:053817, 2013.
- [133] N. J. Schilder, C. Sauvan, J.-P. Hugonin, S. Jennewein, Y. R. P. Sortais, A. Browaeys, and J.-J. Greffet. Polaritonic modes in a dense cloud of cold atoms. *Phys. Rev. A*, 93:063835, 2016.
- [134] L. Corman, J. L. Ville, R. Saint-Jalm, M. Aidelsburger, T. Bienaimé, S. Nascimbène, J. Dalibard, and J. Beugnon. Transmission of near-resonant light through a dense slab of cold atoms. *Phys. Rev. A*, 96:053629, 2017.
- [135] S. J. Roof, K. J. Kemp, M. D. Havey, and I. M. Sokolov. Observation of single-photon superradiance and the cooperative Lamb shift in an extended sample of cold atoms. *Phys. Rev. Lett.*, 117:073003, 2016.
- [136] M. O. Araújo, W. Guerin, and R. Kaiser. Decay dynamics in the coupled-dipole model. *J. Mod. Opt.*, 65(11):1345–1354, 2018.
- [137] Ryan Jones, Reece Saint, and Beatriz Olmos. Far-field resonance fluorescence from a dipole-interacting laser-driven cold atomic gas. *J. Phys. B*, 50(1):014004, 2016.
- [138] Juha Javanainen, Janne Ruostekoski, Yi Li, and Sung-Mi Yoo. Exact electrodynamics versus standard optics for a slab of cold dense gas. *Phys. Rev. A*, 96:033835, 2017.

- [139] S. E. Skipetrov and I. M. Sokolov. Absence of Anderson localization of light in a random ensemble of point scatterers. *Phys. Rev. Lett.*, 112:023905, 2014.
- [140] L. Bellando, A. Gero, E. Akkermans, and R. Kaiser. Cooperative effects and disorder: A scaling analysis of the spectrum of the effective atomic Hamiltonian. *Phys. Rev. A*, 90:063822, 2014.
- [141] Stephan Jennewein, Ludovic Brossard, Yvan R. P. Sortais, Antoine Browaeys, Patrick Cheinet, Jacques Robert, and Pierre Pillet. Coherent scattering of near-resonant light by a dense, microscopic cloud of cold two-level atoms: Experiment versus theory. *Phys. Rev. A*, 97:053816, 2018.
- [142] I. M. Georgescu, S. Ashhab, and Franco Nori. Quantum simulation. *Rev. Mod. Phys.*, 86:153–185, 2014.
- [143] Tetsuya Ido, Thomas H. Loftus, Martin M. Boyd, Andrew D. Ludlow, Kevin W. Holman, and Jun Ye. Precision spectroscopy and density-dependent frequency shifts in ultracold Sr. *Phys. Rev. Lett.*, 94:153001, 2005.
- [144] S. M. Brewer, J.-S. Chen, A. M. Hankin, E. R. Clements, C. W. Chou, D. J. Wineland, D. B. Hume, and D. R. Leibbrandt. $^{27}\text{Al}^+$ quantum-logic clock with a systematic uncertainty below 10^{-18} . *Phys. Rev. Lett.*, 123:033201, 2019.
- [145] M Lyon and S L Rolston. Ultracold neutral plasmas. *Rep. Prog. Phys.*, 80(1):017001, 2016.
- [146] Heejeong Jeong, Andrew M. C. Dawes, and Daniel J. Gauthier. Direct observation of optical precursors in a region of anomalous dispersion. *Phys. Rev. Lett.*, 96:143901, 2006.
- [147] K. Toyoda, Y. Takahashi, K. Ishikawa, and T. Yabuzaki. Optical free-induction decay of laser-cooled ^{85}Rb . *Phys. Rev. A*, 56:1564–1568, 1997.
- [148] M. Chalony, R. Pierrat, D. Delande, and D. Wilkowski. Coherent flash of light emitted by a cold atomic cloud. *Phys. Rev. A*, 84:011401, 2011.

- [149] A D Cimarusti, C A Schroeder, B D Patterson, L A Orozco, P Barberis-Blostein, and H J Carmichael. Control of conditional quantum beats in cavity QED: amplitude decoherence and phase shifts. *New J. Phys.*, 15(1):013017, 2013.
- [150] Ofer Firstenberg, Thibault Peyronel, Qi-Yu Liang, Alexey V. Gorshkov, Mikhail D. Lukin, and Vladan Vuletic. Attractive photons in a quantum nonlinear medium. *Nature*, 502:71, 2013.
- [151] W. Guerin, M.T. Rouabah, and R. Kaiser. Light interacting with atomic ensembles: collective, cooperative and mesoscopic effects. *J. Mod. Opt.*, 64(9):895–907, 2017.